Title

Electron Paramagnetic Resonance Spectroscopy of Photosynthetic Systmes and Inorganic Model Complexes

Author

Dexheimer, S.L.

Publication Date

1990-04-01

LBL-28987

Lawrence Berkeley Laboratory
UNIVERSITY OF CALIFORNIA

CHEMICAL BIODYNAMICS DIVISION

Electron Paramagnetic Resonance Spectroscopy of Photosynthetic Systems and Inorganic Model Complexes

S.L. Dexheimer
(Ph.D. Thesis)

April 1990

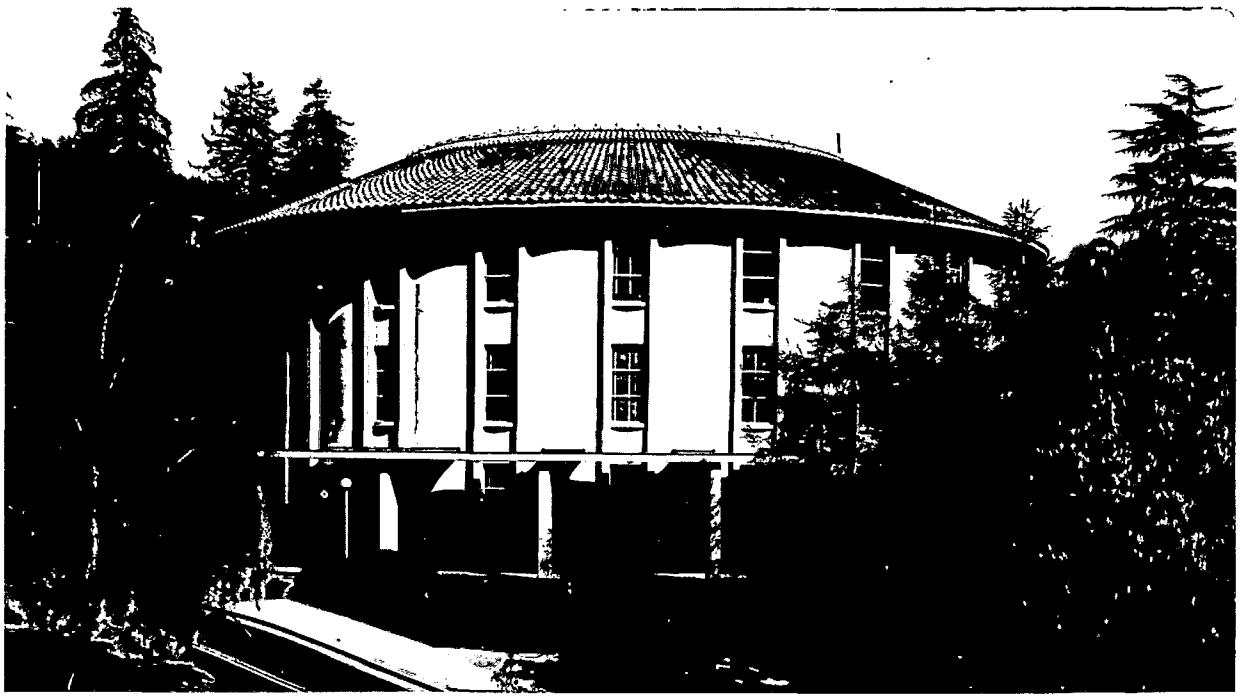

Prepared for the U.S. Department of Energy under Contract Number DE-AC03-76SF00098.

DISCLAIMER

Electron Paramagnetic Resonance Spectroscopy of Photosynthetic Systems and Inorganic Model Complexes

Susan Lynne Dexheimer

Ph.D. Thesis

April 1990

Lawrence Berkeley Laboratory
University of California
Berkeley, California 94720

This work was supported by the U. S. Department of Energy under contract number DE-AC03-76SF00098.

Electron Paramagnetic Resonance Spectroscopy of Photosynthetic Systems and Inorganic Model Complexes

by

Susan Lynne Dexheimer

Abstract

This thesis discusses the application of parallel polarization electron paramagnetic resonance (EPR) spectroscopy, a technique sensitive to formally forbidden transitions in high spin states, to the study of the electronic structure of photosynthetic electron transfer centers and related inorganic model complexes. The theoretical basis for the origin of the parallel polarization transitions and the interpretation of the resulting spectra is presented, and experimental aspects of the detection of parallel polarization transitions are discussed.

Parallel polarization EPR was used to study inorganic complexes of trivalent manganese that serve as models for the spectroscopic properties of biological electron transfer centers. X-band EPR spectra were detected from non-Kramers spin states of these complexes. EPR spectra of the $S = 2$ ground states of the mononuclear complexes Mn(III) tris-acetylacetonate and Mn(III) tris-picolinate and a low-lying excited state of the weakly antiferromagnetically coupled binuclear complex Mn_2(III,III) $O(O_2CCH_3)_2$ $(HB(pz)_3)_2$ ($HB(pz)_3$ = hydrotris(1-pyrazolyl)borate) are discussed. The spectra are interpreted using numerical simulations.

Application of parallel polarization EPR to photosynthetic systems led to the detection of a new paramagnetic intermediate associated with photosynthetic water oxidation. The parallel polarization EPR signal is assigned to an $S = 1$ spin state of

an exchange-coupled manganese center in the resting (S_1) state of the photosynthetic oxygen-evolving complex. The properties of the S_1 state parallel polarization EPR signal indicate that it corresponds to the reduced form of the species that gives rise to the previously established multiline conventional EPR signal in the light-induced S_2 state, and the behavior of the signal upon advancement to the S_2 state demonstrates the presence of two separate redox-active centers in the oxygen-evolving complex. The implications for the electronic structure of the centers are discussed.

Contents

Acknowledgments

I would like to thank my research advisor, Dr. Melvin P. Klein, for his useful suggestions throughout the course of my graduate work. I also thank him for giving me the opportunity to learn about time-domain methods and X-ray spectroscopy in addition to the techniques used in this thesis.

I thank Prof. Bill Armstrong for his enthusiastic interest in this work and for his careful reading of this thesis. I am indebted to his graduate students Joel Gohdes and Mike Chan and his postdoc Karl Hagen for their painstaking work in preparing samples of the inorganic complexes discussed in Chapter 4. I also thank Dave Westmoreland for useful discussions of spin Hamiltonian theory.

I have been fortunate to work in a research group of people with a wide range of expertise. I thank Jim Cole for teaching me how to make photosynthetic preparations and for many helpful discussions of the biophysical literature. I would also like to thank Enrique Dalmasso, Vickie Derose, Ron Guiles, Dennis Kim, Matthew Latimer, Ann McDermott, Peter Sandusky, and Jean-Luc Zimmermann for chemical and biochemical advice, and Sun Un for discussions on programming, electronics, and magnetic resonance theory. In addition, I thank Paul Selvin, Nathan Hunt, and Dave Britt for discussions of microwave techniques. I thank Prof. Ken Sauer for providing references and discussions of the photosynthetic literature. I owe thanks to Phil Eggers and Gary Smith in the Calvin Lab and to Al Daft in the physics machine shop for technical advice and assistance.

I would also like to thank Profs. Bill Bialek and Alan Portis for reading this thesis. Bill Bialek has contributed to my interest in the physics of biological systems, and Alan Portis has provided me with advice throughout my graduate career. I thank Prof.

John Clarke for serving as my physics faculty advisor while I was engaged in graduate research.

This work was supported by grants from the National Science Foundation (PCM84-16676 and PCM88-045260) and by the Director, Office of Energy Research, Office of Basic Energy Sciences, Division of Energy Biosciences of the U. S. Department of Energy under Contract DE-ACO3-76SF00098.

1 Introduction

1.1 Overview of the light reactions of photosynthesis

The light reactions of photosynthesis consist of a series of light-induced electron transfer processes that result in the generation of a potential gradient. The light reactions take place in membrane-bound reaction centers composed of a number of protein subunits, to which are bound a series of electron transfer components that act as donors and acceptors in the light-driven electron transfer processes. In plant photosynthesis, two types of reaction centers, Photosystem (PS) I and PS II, act in series. These reaction centers are bound in the thylakoid membrane, a continuous structure folded within the plant chloroplast. The electron transfer components contained within the PS I and PS II reactions centers, together with those of the cytochrome b_6f complex that couples their electron transport, are displayed according to their approximate redox midpoint potential in the the photosynthetic Z-scheme shown in Figure 1.1. Both the PS I and PS II reaction centers contain a photoactive primary donor, a series of acceptors, and a series of secondary donors. Each reaction center is surrounded by chlorophyll-containing antenna protein complexes that present a large absorption cross section for light in the visible region and direct light excitation energy to the primary donor of the reaction center.

The light reactions begin with photo-excitation of the primary donor to its first excited electronic state, from which an electron is transferred through a series of acceptors. The photo-oxidized primary donor is then reduced by the transfer of an electron through a series of secondary donors. The electron transfer components are arranged so that the terminal donor and terminal acceptor are located on opposite sides of the membrane-bound reaction center complex, stabilizing the oxidized and

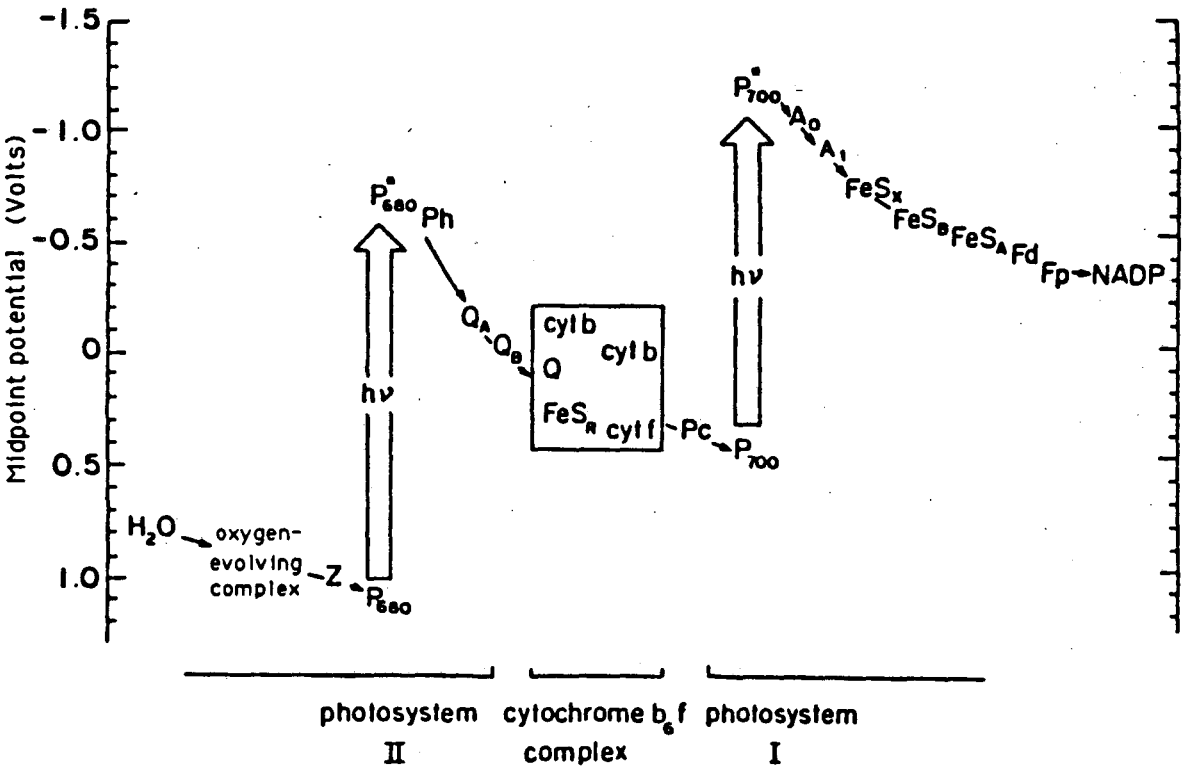

Figure 1.1. The Z-scheme, showing the pathway for photosynthetic electron transfer in plants. Redox components are displayed according to their approximate redox potential. Adapted from Blankenship and Prince (1985) and Cole (1987).

reduced species against charge recombination. The net electrochemical potential gradient across the membrane results largely from a pH gradient generated by proton transfer processes that are coupled to the electron transfer reactions.

The electron transfer components that participate in the light reactions are generally either organic molecules with delocalized π orbitals or transition metal complexes. Both of these types of species may be relatively stable with respect to the gain or loss of at least one electron, allowing them to act as transient intermediates in the electron transfer reactions. The mechanism of electron transfer between these sites is a vibrationally assisted quantum mechanical tunneling process. The rate of electron transfer depends on the distance between the sites and on the electronic structure of the complexes, and is also influenced by the electronic structure and vibrational modes of the intervening protein medium. The relation between structure and dynamics in electron transfer processes remains an area of active experimental and theoretical research (reviewed in Gray and Malmström, 1989). Qualitatively, the rates are expected to decrease exponentially with distance, consistent with a tunneling process. Reorganizational energy within each electron transfer component also plays a significant role. Electron transfers involving non-bonding orbitals require a minimal structural rearrangement of the components upon the gain or loss of an electron, allowing very fast rates. In contrast, significantly slower rates are observed for electron donation from antibonding orbitals, where ligand reorganization is expected to be more substantial. Observed electron transfer rates in photosynthetic systems range from 10^{11} - 10^{12} s^{-1} for the initial light-induced transfers to 10^{3} s^{-1} for the final step in the water oxidation process. (Holtzapfel et al., 1989; Babcock et al., 1976).

The solar energy stored in the photosynthetic light reactions is the ultimate source

of energy for virtually all biochemical processes. The chloroplast coupling factor, a protein complex associated with the thylakoid membrane, uses the electrochemical potential generated by the light reactions to form high energy chemical bonds, converting adenosine diphosphate (ADP) to adenosine triphosphate (ATP). The energy stored in this phosphate bond is used to drive biochemical reactions, including the synthesis of carbohydrates from CO_2 in the photosynthetic dark reactions. The light reactions also generate the strong reductant nicotinamide-adenine dinucleotide phosphate (NADPH) by reducing $NADP^+$, the terminal electron acceptor for the electron transfer processes in PS I, and this reductant is also used in the dark reactions. The carbohydrates synthesized in the dark reactions are, directly or indirectly, the source of virtually all biochemical energy for higher organisms.

Photosynthesis is a highly efficient process for the conversion of solar energy to chemical energy. An aspect of plant photosynthesis that is particularly relevant to solar energy conversion applications is the process of photosynthetic water oxidation, which involves the storage of energy from four successive photo-induced charge separations. This process takes place in PS II, which is described in more detail in the following section. A general introduction to physical processes in photosynthesis can be found in the text by Clayton (1980), and more recent accounts of research in photosynthesis are compiled in a number of serials (for example, those most recently edited by Staehelin and Arntzen, 1986; and Baltscheffsky, 1990).

1.2 Electron transfer in Photosystem II

Water is the terminal electron donor for the electron transfer processes of the light reactions of plant photosynthesis, and the splitting of water to produce molecular

oxygen, four hydrogen ions, and four electrons takes place in PS II. The reaction is mediated by a protein complex, known either as the water oxidation complex or the oxygen-evolving complex, which contains redox-active manganese ions. As shown in the left-hand side of the Z-scheme in Figure 1.1, electron transfer in PS II begins with the photo-excitation of the primary donor, P_{680}, which is named for its characteristic optical absorption maximum at 680 nm. The photo-excited electron undergoes rapid transfer to an intermediate pheophytin species, and then in sequence to the quinone acceptors Q_A and Q_B. Transfer of an electron from the oxygen-evolving complex via the intermediate Z reduces the photo-oxidized primary donor, allowing repetition of the photochemical cycle. Electron transfer in PS II has recently been reviewed (Andréasson and Vänngard, 1988).

The overall structure of the PS II reaction center in plants bears a strong similarity to that of the reaction centers of the simpler photosynthetic bacteria *Rhodopseudomonas Viridis* and *Rhodobacter Sphaeroides*. The molecular structures of the reaction centers of these bacteria have recently been determined by X-ray crystallography (Deisenhofer et al., 1984, 1985; Allen et al., 1986), and many of the more detailed proposals for the structure of the PS II reaction center have been based on these results (Michel and Deisenhofer, 1988). The reaction center of the photosynthetic bacterium *R. Viridis* contains three protein subunits L, M, and H. Cofactors bound to the L and M subunits include a specialized pair of bacteriochlorophyll molecules that forms the primary donor, two additional monomeric bacteriochlorophylls, two bacteriopheophytins, a menaquinone as Q_A, a ubiquinone as Q_B, and a non-heme Fe^{2+} ion. These cofactors are arranged in an approximate C_2 symmetry, with the primary donor and the Fe^{2+} ion centered on the C_2 axis on opposite sides of the protein complex. A suprising

aspect of the bacterial reaction center is that although the two branches of the complex are structurally very similar, physiological electron transfer proceeds along only one branch, and the bacteriochlorophyll and bacteriopheophytin bound to the M subunit appear to be inactive. The role of the bacteriochlorophyll bound to the L subunit is currently under debate. Recent time-resolved optical absorption measurements suggest that this species acts as the initial acceptor of the photo-excited electron from the primary donor before the electron is transferred to the bacteriopheophytin (Holtzapfel et al., 1989), in contrast to previous results indicating that the pheophytin is the initial acceptor (Martin et al., 1986). The non-heme Fe^{2+} ion appears to play mainly a structural role and is not directly involved in the electron transfer processes, despite the magnetic coupling between the ion and the reduced quinone acceptors (Butler et al., 1980, 1984; Kirmaier et al., 1986). The similarity between the bacterial reaction center and the PS II reaction center in plants does not extend to the donor side. In the bacterial reaction center, reduction of the photo-oxidized primary donor is accomplished simply by a cytochrome donor rather than by the oxidation of water.

The sketch of PS II components shown in Figure 1.2 reflects the current knowledge of the organization of the PS II reaction center, as well as some speculation based largely on comparison with the bacterial reaction centers. Most of the electron transfer components are bound within two polypeptides, D_1 and D_2, which are substantially homologous to the L and M subunits of the bacterial reaction centers (Hearst, 1986). The primary donor P_{680} is thought to be a specialized pair of chlorophyll molecules, in analogy to the primary donor of the bacterial reaction centers, and pheophytin and accessory chlorophyll species are thought to be present, as well (Michel and Deisenhofer, 1988, and references therein). The acceptors Q_A and Q_B

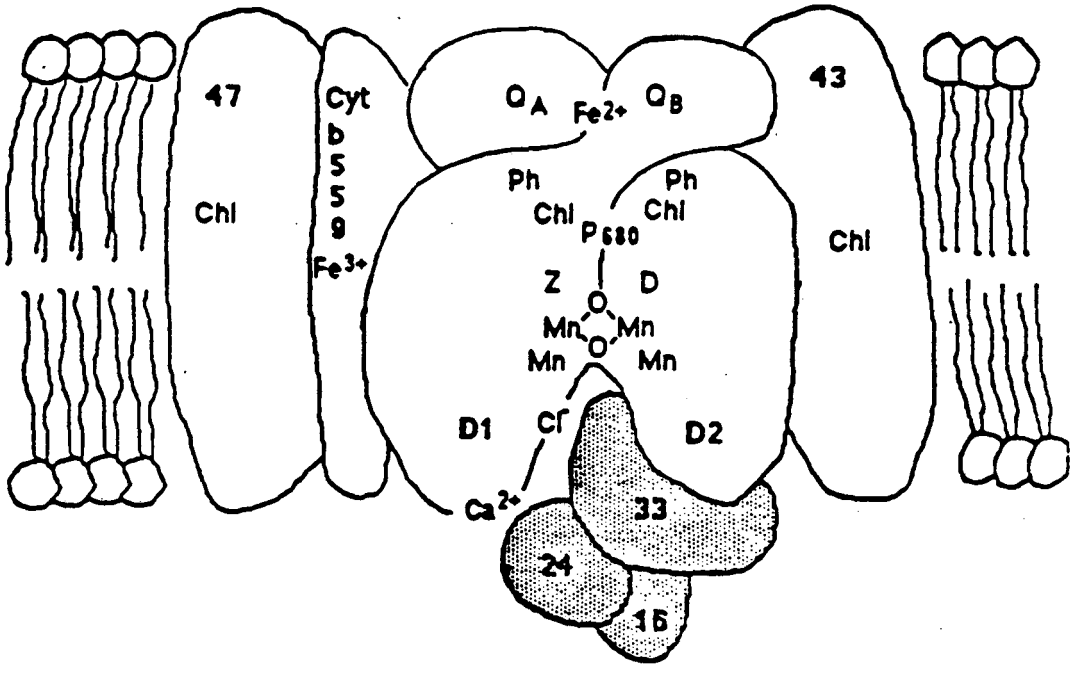

Figure 1.2. Model for the organization of Photosystem II components. Adapted from Rutherford (1989) and Cole (1987).

in PS II are plastoquinone species and are also associated with a non-heme Fe^{2+} ion. The intermediate donor Z has recently been identified as a redox-active tyrosine amino acid residue on the D_1 polypeptide (Debus et al., 1988b). The species D corresponds to a tyrosine residue located on the D_2 polypeptide (Barry and Babcock, 1987; Debus et al.,1988a); however, this species does not participate in the normal pathway for electron transfer and is generally stable in its oxidized form. The manganese ions associated with water oxidation are also thought to be bound within the D_1 and D_2 polypeptides. Two additional large polypeptides of molecular weight 43 and 47 kDa contain antenna chlorophyll species. Each PS II reaction center also includes two cyt b_{559} proteins. Their physiological function is not yet clear, although they may act as alternate electron donors when the oxygen-evolving complex is not functional. Three extrinsic (non-membrane-bound) polypeptides of approximate molecular weight 16, 24, and 33 kDa are associated with the reaction center, and smaller polypeptides may be present as well. Soluble cofactors necessary for the function of PS II include Ca^{2+} and Cl^- ions, although the precise roles of these ions have not yet been established. The composition of the PS II complex is discussed in a recent review (Babcock, 1987).

1.3 Photosynthetic water oxidation

The photosynthetic oxidation of water to molecular oxygen,

$$2H_2O \rightarrow O_2 + 4H^+ + 4e^-,$$

is a four-electron process, while the reduction of the photo-oxidized primary donor is a single-electron process. As a result, the oxygen-evolving complex must couple the four-electron oxidation of water to the single-electron photochemistry of the rest of the reaction center. This function has been described in terms of an S-state model (Kok et

al., 1970) in which the oxygen-evolving complex cycles through a series of states, S_0 - S_4, as it transfers electrons to reduce the primary donor while accumulating oxidizing equivalents for water oxidation. When the complex reaches the state S_4, molecular oxygen is released and the complex reverts to the S_0 state. The S-state model, which is depicted in Figure 1.3, was originally developed to explain the results of oxygen evolution measurements on photosynthetic preparations in which the yield of oxygen evolved following each of a series of short, saturating light flashes showed a periodicity of four as a function of flash number (Joliot et al., 1969). For preparations that were dark-adapted prior to the measurements, the first peak in the oxygen yield appears after the third light flash, indicating that the resting state of the complex is the S_1 state.

Although the S-state model is successful in describing the overall function of the oxygen-evolving complex, the mechanism of charge storage and subsequent oxidation of water remains unknown. In particular, the electronic structure of the species that constitute the S-states and the relation of this structure to the function of the oxygen-evolving complex have been the subject of continued study and speculation. This literature has recently been reviewed from a variety of perspectives (Rutherford, 1989; Pecoraro, 1988; Babcock, 1987). Biochemical studies (reviewed in Radmer and Chenaie, 1977) have demonstrated a requirement of manganese for oxygen evolution activity, and the electrochemical properties of manganese are consistent with the generation of the redox potential required for water splitting (see, for example, Lawrence and Sawyer, 1978). Quantitation procedures indicate a stoichiometry of four functional manganese ions per PS II unit (Yocum et al., 1981; Chenaie, 1980), but the structural organization and oxidation states of the manganese ions throughout the S-state cycle

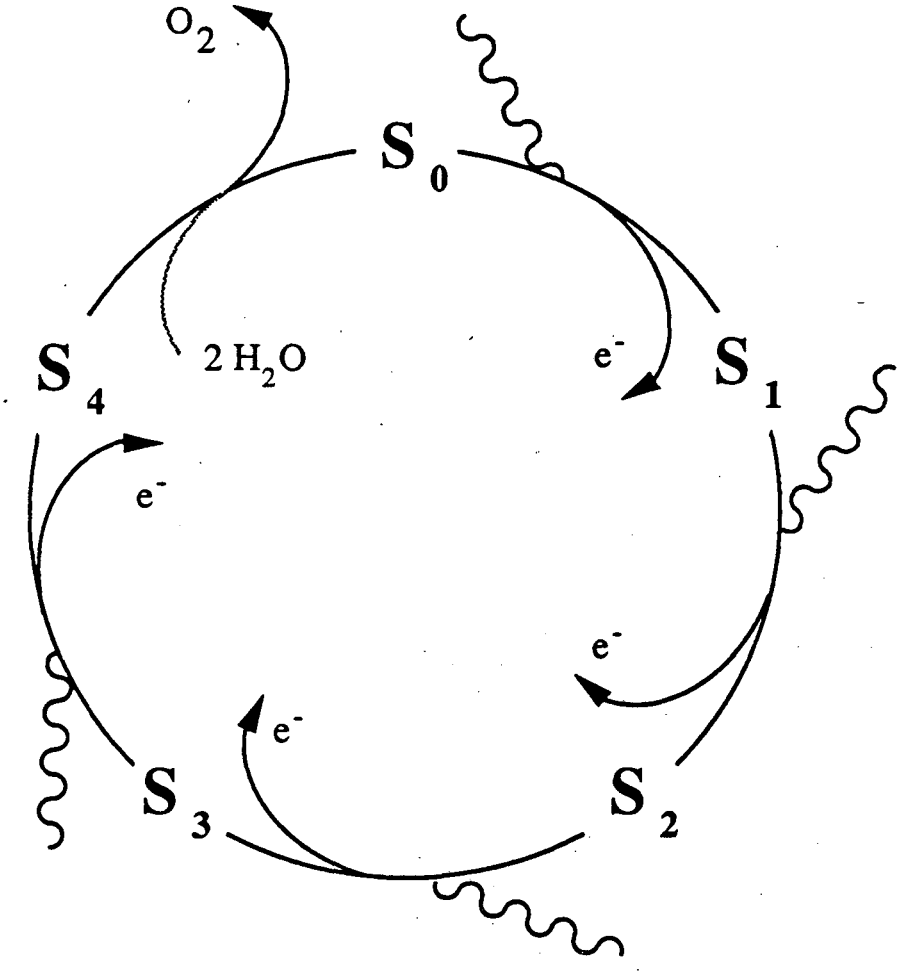

Figure 1.3. The S-state model for the function of the photosynthetic oxygen-evolving complex. See text for details.

have not yet been established.

Much of what is known about the structure of the manganese centers in the oxygen-evolving complex has resulted from electron paramagnetic resonance (EPR) and X-ray absorption spectroscopic techniques. EXAFS measurements have demonstrated that at least two of the manganese ions are present in a bridged structure similar to that illustrated in Figure 1.2 with a distance of 2.7 Å between the ions (Kirby et al., 1981; Yachandra et al., 1986, 1987; Guiles et al., 1990a,b). More recent EXAFS results indicate the presence of additional manganese and/or calcium ions at distances greater than 3 Å (George et al., 1988; Penner-Hahn et al., 1990a,b).

Measurements of the manganese X-ray K-edge absorption energy on photosynthetic preparations poised in various S-states have provided information on the manganese oxidation state changes throughout the S-state cycle. For free ions of the first transition series, the X-ray K-edge absorption corresponds mainly to transitions from the 1s shell to the unoccupied 4p orbitals. For ions in complexes, the edge energy is influenced by a number of factors, including the nature of the covalent interactions between the metal ion and the neighboring ligands, the electron donating character of the ligands, the symmetry of the metal center, and the nuclearity of the complex (Shulman et al., 1976; Cartier et al., 1986). In general, for a given set of ligands, the edge energy is expected to increase as the oxidation state of the ion increases. The manganese edge energy in the S_2 state is about 1 eV higher than that of the S_1 state (Yachandra et al., 1987), whereas measurements on preparations treated with the reductant hydroxylamine so as to induce a redox state analogous to the S_0 state show a decrease of about 1 eV relative to the S_1 state (Guiles et al., 1990b).

Comparison of the edge spectra of the photosynthetic system with those of well-

characterized inorganic complexes has allowed some qualitative interpretation of these results. The changes in the absorption edge energy are consistent with successive one-electron oxidations of the pool of manganese ions in the S_0 to S_1 and S_1 to S_2 transitions. The manganese absorption edge energy in the S_1 and S_2 states is in the range typical of Mn(III) and Mn(IV) complexes. Assuming a stoichiometry of four manganese ions in the oxygen-evolving complex, and given that the S_2 state exhibits a mixed-valence EPR signal (see below), these results indicate that the oxidation state of the manganese ions are (III, III, III, III) or (III, III, IV, IV) in the S_1 state and (III, III, III, IV) or (III, IV, IV, IV) in the S_2 state. Proposed influences of ligand electronegativity may favor the higher oxidation state estimates (Guiles, 1988). The change in the absorption edge energy in the S_0 to S_1 transition is consistent with the oxidation of one of the manganese ions from the Mn(II) oxidation state to the Mn(III) oxidation state. Differences between the EXAFS spectra for the S_0, S_1, and S_2 states are consistent with the changes in manganese-ligand bond lengths expected to accompany these oxidation state changes (Guiles et al., 1990b; Derose et al., unpublished observations). Preparations in which a substantial number of centers have been advanced to the S_3 state show no difference in edge energy from samples in the S_2 state, suggesting that oxidation of manganese does not occur in this transition, and it has been proposed that a redox-active amino acid residue closely associated with the manganese complex is oxidized instead (Guiles et al., 1990a).

EPR spectroscopy has also provided insight into the structure of the manganese ions associated with the oxygen-evolving complex. Although the system has been thoroughly studied with conventional EPR spectroscopy, only two signals attributed to manganese in the native enzyme have been reported, and both occur in the S_2 state.

The multiline signal consists of at least 19 partially resolved hyperfine components over a field range of approximately 1500 G centered near g = 2. The hyperfine structure of the multiline signal is similar to that observed for $S = 1/2$ spin states of exchange-coupled mixed-valence manganese complexes (Dismukes and Siderer, 1980, 1981). A second signal associated with the S_2 state appears at an effective g value of 4.1 (Casey and Sauer, 1983; Zimmermann and Rutherford, 1984, 1986). The field position of this signal is consistent with an $S = 3/2$ species of nearly axial symmetry, and the correlation of the generation of this signal with an increase in the manganese X-ray absorption energy suggests that the signal originates from manganese (Cole et al., 1987).

More recently, two new EPR signals have been observed in PS II preparations biochemically treated so as to remove Ca^{2+} ions required for normal functioning of the oxygen-evolving complex (Boussac et al., 1989) The Ca^{2+} depleted preparations exhibit a multiline signal that differs from the native multiline signal in that it appears in a dark-stable S_2 state and has somewhat altered hyperfine structure. Illumination of these preparations produces a nearly Gaussian signal with a width of 164 G centered at g = 2 that has been attributed to a free radical magnetically coupled to a manganese center in a formal S_3 charge accumulation state. It is not yet clear whether the changes in the EPR properties of the complex following Ca^{2+} depletion result from changes in coordination near the manganese ions or from more indirect conformational changes in the surrounding protein subunits.

Comparison of the spectroscopic properties of the oxygen-evolving complex with those of structurally well-characterized synthetic inorganic complexes provides insight into possible structures for the photosynthetic manganese centers. The hyper-

fine structure of the multiline signal resembles that of mixed-valence oxo-bridged manganese complexes. One example of this type of complex is the Mn_2(III,IV)(μ-O)$_2$(2,2'-bipyridine)$_4$ binuclear complex (Plaksin et al., 1972). This complex contains two manganese ions connected by two bridging oxygen ligands. Each of the two manganese ions has approximate octahedral geometry, with the remaining coordination sites filled by nitrogen atoms from the bipyridyl ligands. The interatomic distances in this complex are similar to a number of those observed in the EXAFS spectra of the biological complex, including an Mn - Mn distance of 2.7 Å, an Mn - bridging O distance of 1.8 Å, and Mn - terminal N distances ranging from 2.0 to 2.2 Å. The two manganese ions are valence trapped, and the oxo bridges mediate an antiferromagnetic superexchange coupling between the $S = 2$ Mn(III) ion and the $S = 3/2$ Mn(IV) ion, giving an $S = 1/2$ ground spin state (Cooper et al., 1978). The EPR spectrum arising from this spin state consists of 16 partially resolved hyperfine lines with an average spacing and overall structure similar to that of the multiline signal. Similar 16-line EPR spectra have been observed in other binuclear, mixed-valence manganese complexes (Hagen et al., 1987; Pecoraro, 1988). However, the EPR spectra of these complexes have fewer hyperfine components than the multiline signal, indicating that the biological center may be more complex. EPR signals with features near an effective g of 4 have been observed in synthetic mononuclear Mn(IV) species with axial symmetry, as well as in $S = 3/2$ states of complexes of higher nuclearity (Chan and Armstrong, 1988; Pecoraro et al., 1990).

A number of models have been proposed for the structural organization of manganese in the oxygen-evolving complex. Brudvig and Crabtree (1986) and Christou and Vincent (1987) have proposed that four manganese ions are associated in a single

tetranuclear cluster. In contrast, Hansson, Aasa, and Vänngard (1987) have proposed that the manganese ions are present in separate centers, including a binuclear center and at least one mononuclear center, and Pecoraro (1988) and Penner-Hahn et al. (1990a,b) have proposed a modification of this model involving a trinuclear center and a mononuclear center. More recently, Guiles et al. (1990a) proposed that the oxygen-evolving complex contains a pair of possibly loosely associated binuclear centers. These proposals for the structural organization of manganese in the oxygen-evolving complex have been reviewed in the light of previous experimental evidence (Rutherford, 1989).

1.4 Thesis scope and format

This thesis discusses the application of parallel polarization EPR, an unconventional EPR technique sensitive to formally forbidden transitions in high spin states, to the study of the photosynthetic oxygen-evolving complex and related inorganic model complexes. Theoretical aspects of the electronic structure of these transition metal centers and the origin of the EPR transitions are presented in Chapter 2. The instrumentation used for the detection of the parallel polarization EPR signals is described in Chapter 3. EPR measurements on inorganic manganese complexes are presented and discussed in Chapter 4. Finally, the detection of a paramagnetic intermediate in the S_1 state of the photosynthetic oxygen-evolving complex and its implications for the structure of the complex are discussed in Chapter 5.

2 Theory

2.1 Introduction

This chapter discusses the theoretical basis for the interpretation of the EPR spectra presented in Chapters 4 and 5. An overview of the electronic structure of transition metal complexes is presented in Section 2.2. This discussion is focussed on the properties of ions of the first transition series, and the states of the $3d^4$ configuration corresponding to Mn(III) are presented as an example. Section 2.3 outlines the spin Hamiltonian formalism used in the interpretation of EPR spectra and discusses the physical origin of the spin Hamiltonian parameters. Section 2.4 discusses the energy levels of the $S = 1$, $S = 2$, and $S = 5/2$ spin states relevant to the measurements presented in Chapters 4 and 5, and discusses the origin of the EPR transitions. Numerical simulation of high spin EPR spectra is discussed in Section 2.5.

2.2 Electronic structure of transition metal complexes

The magnetic properties of transition metal ions result from the unpaired electrons in the d orbitals. For free ions, that is, for ions in a spherically symmetric environment, the electronic wavefunctions are eigenfunctions of the orbital and spin angular momentum. In the Russell-Saunders spin-orbit coupling limit, which applies to ions of the first transition series, the total orbital angular momentum and the total spin angular momentum couple to give a resultant spin $\mathbf{J} = \mathbf{L} + \mathbf{S}$, and the magnetic moment of the free ion is simply given by $\mu = -g_L \beta \mathbf{J}$, where g_L is the Landé g-factor. For ions in crystal lattices or molecular complexes, the non-spherically symmetric potential resulting from the neighboring ligands may substantially alter the magnetic properties of the ion. The field due to the neighboring ions or ligands is referred to as the crystal

or ligand field, where the term crystal field carries the connotation that the effect of the neighboring ions can be modelled as a classical charge distribution and that the single-electron wavefunctions of the transition metal ion are similar in form to those of the free ion, whereas the more general term ligand field is meant to include the effects of possible covalent interactions between the metal and ligand orbitals. In either case, the properties of the complex ion are determined largely by the symmetry and magnitude of this non-spherical potential.

For the ions of the first transition series, the ligand field is typically on the order of 10,000 cm^{-1} and can often be treated as a perturbation on the free ion terms characterized by the quantum numbers L and S. The field is substantially larger than the spin-orbit interaction, which is typically on the order of 100 cm^{-1} in the first transition series. This regime, in which

$$H_{coulomb} >> H_{ligand-field} >> H_{spin-orbit}$$

where $H_{coulomb}$ represents the coulombic interaction between the d electrons of the ion, is known as the intermediate ligand field limit, in which the ligand field and spin-orbit interaction may be treated as successive perturbations on the free ion terms. In practice, the ligand field may consist of a dominant contribution of high symmetry and a smaller contribution of lower symmetry, for example, a largely octahedral field with a smaller tetragonal distortion, and the lower symmetry part may be comparable in magnitude to the spin-orbit interaction.

Because of the angular dependence of the d orbitals, some d electrons will interact more strongly than others with the ligand field, resulting in the breaking of their degeneracy. For example, in an octahedral ligand field, the d_{z^2} and $d_{x^2-y^2}$ orbitals, which

transform according to the E_g (Γ_3) representation of the O_h symmetry group, will be raised in energy relative to the d_{xy}, d_{xz}, and d_{yz} T_2 (Γ_5) orbitals. In the intermediate field regime, the field may quench the L_z component of the orbital angular momentum of the ground state wavefunction, and in contrast to the free ion, the magnetic properties will depend almost entirely on the spin angular momentum. However, the perturbation resulting from the spin-orbit interaction $\lambda \boldsymbol{L} \cdot \boldsymbol{S}$ may mix in some orbital angular momentum from excited states, leading to a small orbital contribution to the magnetic moment.

As an example of the effect of a ligand field on the free ion terms, the Tanabe-Sugano diagram (Tanabe and Sugano, 1954) for a $3d^4$ ion in an octahedral field is shown in Figure 2.1. The free ion terms are shown at the left-hand side of the diagram. The energies of the states into which the free ion terms are split are plotted as a function of the ligand field strength, Δ. All energies are scaled according to the Racah parameter B, which is a measure of the mutual electrostatic interaction of the electrons in a given ion. The vertical line indicates the transition between the intermediate and strong ligand field limits. In the strong ligand field limit, the ligand field is larger than the energy of the coulombic repulsion between the d electrons, and the electrons pair in the lowest-lying set of orbitals rather than filling the higher orbitals. For a $3d^4$ ion, the ground free ion term is ${}^5D$. In an octahedral ligand field of moderate strength, this term splits into a doubly degenerate ${}^5E$ ground state, which has a t_2^3e configuration in terms of the single-electron orbitals, and a triply degenerate ${}^5T_2$ excited state corresponding to a $t_2^2e^2$ configuration. The energies of the single-electron orbitals corresponding to the ground state configuration of a high spin $3d^4$ ion in an octahedral field are displayed in Figure 2.2a. Most complexes of Mn(III) have a high

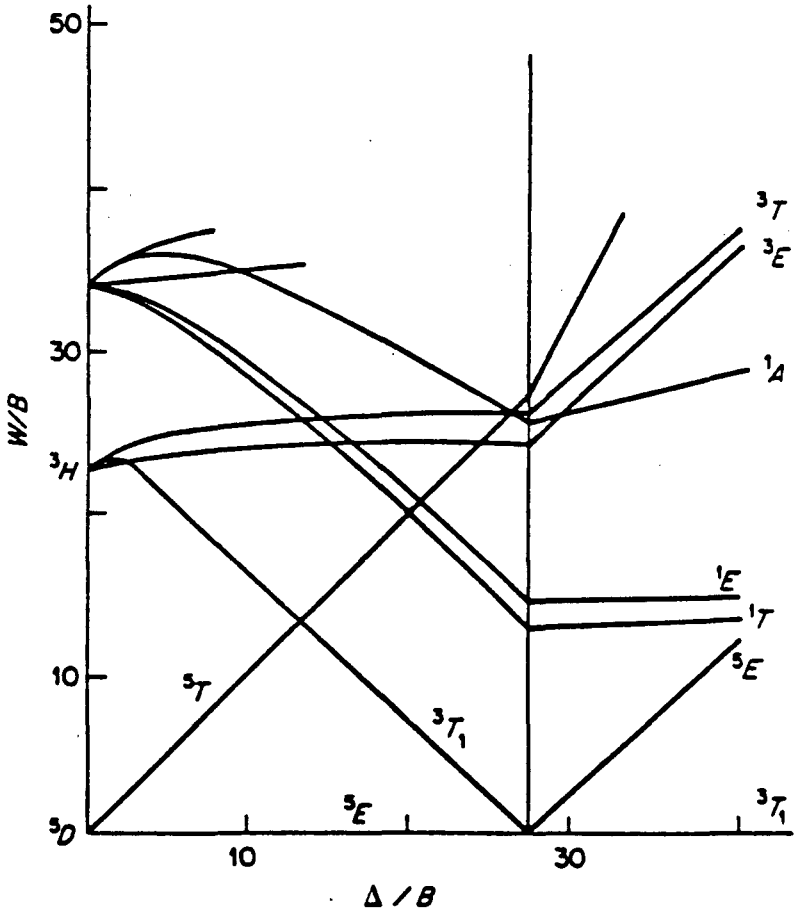

Figure 2.1. Tanabe-Sugano diagram for the $3d^4$ configuration, showing the splitting of the free ion terms as a function of ligand field strength Δ for a field of octahedral symmetry. (Adapted from Tanabe and Sugano, 1954).

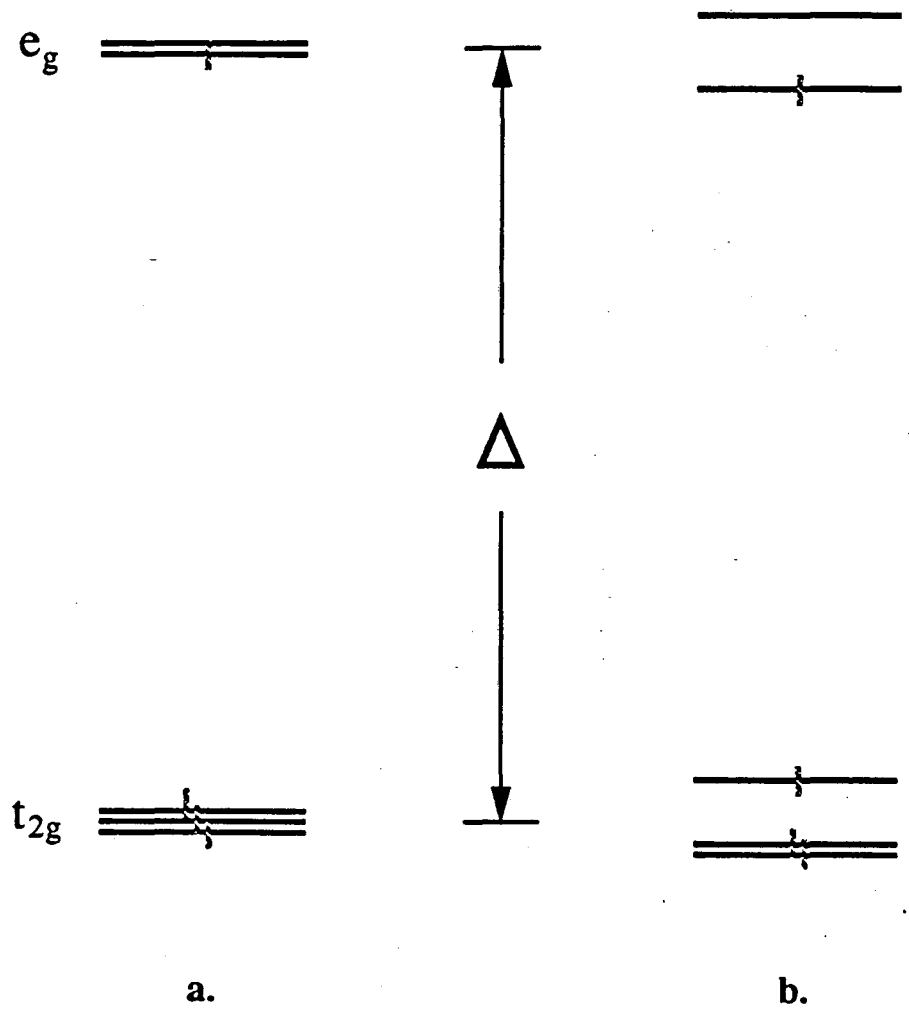

Figure 2.2.a. Splitting of the d-orbitals in a ligand field of octahedral symmetry. The occupation of the orbitals corresponds to a high spin $3d^4$ configuration. **b.** Splitting of the orbitals under a tetragonal elongation.

spin ground state.

For situations in which the ligand field does not completely remove the orbital degeneracy of the ground state of a complex ion, the Jahn-Teller effect also influences the properties of the complex. The Jahn-Teller theorem (reviewed in Bersuker, 1975) demonstrates that nonlinear complexes having an electronic degeneracy other than the Kramers degeneracy resulting from time-reversal symmetry in odd-electron systems are inherently unstable. Coupling between the vibronic and electronic degrees of freedom will cause such a complex to distort to a nuclear configuration of lower symmetry so as to remove the degeneracy. As an example, the effect of a tetragonal elongation on the single-electron orbitals of the $3d^4$ ion is shown in Figure 2.2b. A tetragonal elongation in which the metal-ligand distances for the two ligands along the z axis of the complex are increased relative to the metal-ligand distances in the x-y plane lowers the energy of the d_{z^2} orbital relative to that of the $d_{x^2-y^2}$ orbital, thereby breaking the degeneracy of the ${}^5E$ state. Similarly, a tetragonal compression lowers the energy of the $d_{x^2-y^2}$ orbital relative to that of the d_{z^2} orbital. At a sufficiently low temperature, the complex may remain trapped in one of these minima, resulting in a static Jahn-Teller distortion. This will produce a ${}^5A_1$ ground state in the case of a tetragonal compression and a ${}^5B_1$ ground state in the case of a tetragonal elongation for a $3d^4$ ion. The influence of the Jahn-Teller effect on EPR spectra of transition metal complexes has been reviewed (Ham, 1972). A general treatment of ligand field theory and its application to EPR of transition metal ions has been presented in a number of texts (for example, Griffith, 1961; Abragam and Bleaney, 1970).

2.3 Spin Hamiltonian formalism

EPR spectra are generally interpreted in terms of the spin Hamiltonian formalism. The spin Hamiltonian describes the properties of the ground manifold of states, which usually corresponds to the $2S + 1$ levels of the lowest-lying spin state. The allowed terms in the spin Hamiltonian depend on the magnitude of the spin and the symmetry properties of the potential. These considerations have been extensively discussed in a number of texts (for example, Abragam and Bleaney, 1970; Pake and Estle, 1973).

For a spin $S = 1/2$, the spin Hamiltonian simply consists of the Zeeman term,

$$H_{Zeeman} = \beta \mathbf{H}_0 \cdot \mathbf{g} \cdot \mathbf{S}. \qquad (2.3-1)$$

The difference between the g tensor values and the free electron g value results from the admixture by the spin-orbit interaction of orbital angular momentum from excited states. For spins $S \geq 1$, a term quadratic in the spin operators that introduces a splitting of the levels at zero magnetic field may also be present. This term may be expressed in terms of the axial zero-field parameter D and the rhombic zero-field parameter E in the molecular principal axis frame:

$$H_{zero-field} = D[S_z^2 - \frac{1}{3}S(S+1)] + E(S_x^2 - S_y^2). \qquad (2.3-2)$$

The quadratic zero-field parameters may include contributions from the admixture of excited state orbital angular momentum as well as from dipolar interactions. In general, the molecular axes may be chosen so that $|E/D| \leq \frac{1}{3}$, where the equality holds for a maximally rhombic system. For $S \geq 2$, terms of higher order in the spin operators resulting from the ligand field, as well as from higher order spin-orbit contributions, may be present. For example, a ligand field of cubic symmetry will give rise to the

term:

$$H_{cubic} = \frac{a}{6}[(S_x^4 + S_y^4 + S_z^4) - \frac{1}{5}S(S+1)(3S^2 + 3S - 1)] \qquad (2.3-3)$$

Within the limits of crystal field theory, the parameter a may be related to the magnitude of the electrostatic potential seen by the transition metal ion (see, for example, Wertz and Bolton, 1972). The Hamiltonian terms resulting from lower symmetry components of the ligand field are generally small in comparison to the axial and rhombic quadratic zero-field terms described above, and are often neglected.

Hyperfine interactions are also present when the nuclear spin of the ion is nonzero:

$$H_{hyperfine} = \boldsymbol{S} \cdot \boldsymbol{A} \cdot \boldsymbol{I}. \qquad (2.3-4)$$

The isotropic part of the hyperfine tensor results from the Fermi contact interaction from a nonzero unpaired spin density at the nucleus. The anisotropic part of the hyperfine tensor results from electron-nuclear dipolar interactions (Abragam and Pryce, 1951). Ligand superhyperfine interactions result from overlap of metal orbitals with unpaired spin density onto the ligand nuclei, as well as from electron-nuclear dipolar interactions. Additional terms involving nuclear spin operators include a nuclear Zeeman term, and a nuclear quadrupole term for $I \geq 1$; however, these terms usually do not contribute significantly to the EPR spectrum.

The derivation of the spin Hamiltonian parameters for a high spin $3d^4$ ion in tetragonal symmetry has been discussed by Griffith (1961). The dominant contribution to the g tensor is from an admixture of the $^5T_2$ excited state at an energy Δ above the ground state. This gives rise to the corrections:

$$\begin{aligned} g_z &= 2, & g_x = g_y &= 2 - \tfrac{6\lambda}{\Delta} & &\text{for } {}^5A_1 \\ g_z &= 2 - \tfrac{8\lambda}{\Delta}, & g_x = g_y &= 2 - \tfrac{2\lambda}{\Delta} & &\text{for } {}^5B_1. \end{aligned} \qquad (2.3-5)$$

The value of the spin-orbit coupling parameter λ for the Mn(III) free ion is 88 cm^{-1}, and the value for an ion in a ligand field is expected to be somewhat lower. Typical values for the ligand field splitting parameter Δ for Mn(III) complexes are in the range of 12,000 - 21,000 cm^{-1}. As a result, the g tensor values for Mn(III) complexes are expected to differ from the free electron g value by at most a few percent. The quadratic zero-field parameter D for the $3d^4$ ion includes contributions from the excited state ${}^5T_2$ at an energy Δ and the state ${}^3T_1$ at an energy Δ', as well as from spin-spin dipolar interactions characterized by a spin-spin coupling parameter ρ. The resulting expression for D is

$$D = \pm 3 \{ \frac{\lambda^2}{\Delta} + \frac{4\lambda^2}{3\Delta'} + \rho \} \qquad (2.3-6)$$

where the positive sign applies to the ${}^5A_1$ state and the negative sign applies to the ${}^5B_1$ state. The contribution from the ${}^3T_1$ state may be significantly larger than the contribution from the ${}^5T_2$ state. The spin-spin contribution is expected to be rather small, as the estimated value for ρ is less than 0.1 cm^{-1}. Values of D as determined by magnetic susceptibility measurements typically fall in the range $|D| = 1 - 4$ cm^{-1} for Mn(III) complexes (Kennedy and Murray, 1985).

When more than one ion is present in a complex, exchange interactions may also contribute to its magnetic properties. In multinuclear biological metal centers, the relevant mechanism is that of superexchange, in which the interaction between the metal ions is mediated by the intervening ligands. The superexchange interaction results from the admixture of excited states in which an electron is transferred from

one ion to the other (Anderson, 1959). The primary effect of this interaction is to introduce an isotropic coupling between the spins of the form

$$H_{exchange} = -2JS_1 \cdot S_2 \qquad (2.3-7)$$

where the magnitude and sign of J depend on the details of the electronic orbitals of the ions and the nature of the bonding interactions with the intervening ligands. Observed values of J for pairs of first-row transition metal ions present as impurities in diamagnetic crystals range from less than 1 cm^{-1} to several hundred cm^{-1} (Owen and Harris, 1972).

Anisotropic interactions may also be present between the ions. The simplest of these is the classical dipolar interaction, which leads to a term of the form

$$H_{dipolar} = D_d(3S_{1z}S_{2z} - S_1 \cdot S_2) \qquad (2.3-8)$$

when the g tensors for the individual ions are equal and isotropic, where $D_d = -g^2\beta^2/r^3$ and the z axis is along the line joining the ions. This expression assumes that the ions may be considered to be point dipoles. In practice, covalent interactions may introduce substantial corrections. The combined effect of isotropic exchange and the spin-orbit interaction may give rise to a pseudodipolar exchange interaction. This results in a Hamiltonian term with a functional form identical to that of the classical dipolar interaction. For ions with orbital singlet ground states, the magnitude of the pseudodipolar exchange interaction is on the order of $J\lambda^2/\Delta^2$. Additional anisotropic exchange mechanisms give significant contributions only for ions that are orbitally nondegenerate.

The spin Hamiltonian for a pair of exchange-coupled ions may be expressed in the

coupled representation in terms of the total spin $\mathbf{S} = \mathbf{S_1} + \mathbf{S_2}$ (Scaringe et al., 1978). In the limit that the term in J is much greater than the other spin Hamiltonian terms, the spin Hamiltonian for a pair of similar spins may be expressed in a functional form identical to that for a single ion:

$$H_{coupled} = \beta \boldsymbol{H}_0 \cdot \boldsymbol{g} \cdot \boldsymbol{S} + D_s[S_z^2 - \frac{1}{3}S(S+1)] + E_s(S_x^2 - S_y^2) \qquad (2.3-9)$$

where the parameters D_s and E_s include contributions from anisotropic exchange interactions as well as from the zero-field parameters of the individual ions. These contributions are weighted by coefficients appropriate to the spin states S, S_1, and S_2. The effect of exchange interactions on EPR spectra has been extensively reviewed (Owen and Harris, 1972; Baker, 1971).

2.4 Energy levels and EPR transitions for particular spin states

2.4.A S = 1

The $S = 1$ spin state provides the simplest example of the origin of the parallel polarization EPR transitions that result from mixing of the Zeeman basis states by the zero-field Hamiltonian. The spin Hamiltonian for an $S = 1$ spin state consists of the Zeeman and quadratic zero-field terms discussed in the previous section. When only the Zeeman term is present, the eigenstates of the Hamiltonian are eigenstates of the **z** component of the spin angular momentum, where the axis of quantization is determined by the direction of the applied magnetic field. The Zeeman eigenstates are defined by the quantum number m_s, and the energy levels are given by $g\beta H m_s$. The zero-field Hamiltonian can mix the Zeeman states, leading to a splitting of the levels at zero field and producing eigenstates of the total spin Hamiltonian that are no

longer eigenstates of the z component of the angular momentum. The eigenstates of the $S = 1$ zero-field Hamiltonian may be expressed:

$$\begin{aligned} |+\rangle &= \tfrac{1}{\sqrt{2}}\{|+1\rangle + |-1\rangle\}, & E_+ &= \tfrac{1}{3}D + E \\ |-\rangle &= \tfrac{1}{\sqrt{2}}\{|+1\rangle - |-1\rangle\}, & E_- &= \tfrac{1}{3}D - E \\ |O\rangle &= |0\rangle, & E_O &= -\tfrac{2}{3}D \end{aligned} \qquad (2.4-1)$$

where the eigenstates are written in terms of the angular momentum eigenstates $|m_s\rangle$ with the z molecular axis as the axis of quantization. The eigenstates of the $S = 1$ zero-field Hamiltonian are nondegenerate, reflecting the lack of time-reversal symmetry of the Hamiltonian. In general, none of the levels of an integer spin state are necessarily degenerate at zero field. Such spin states are termed non-Kramers states to distinguish them from half-integral spin states, which retain the Kramers degeneracy at zero field.

The $S = 1$ energy levels are displayed in Figure 2.3 as a function of applied magnetic field for the case in which the applied magnetic field is parallel to the z molecular axis. For this molecular orientation, the eigenstates and energies have the simple form:

$$\begin{aligned} |+\rangle &= \cos\alpha\,|+1\rangle + \sin\alpha\,|-1\rangle, & E_+ &= \tfrac{1}{3}D + [(g_z\beta H_0)^2 + E^2]^{\frac{1}{2}} \\ |-\rangle &= \sin\alpha\,|+1\rangle - \cos\alpha\,|-1\rangle, & E_- &= \tfrac{1}{3}D - [(g_z\beta H_0)^2 + E^2]^{\frac{1}{2}} \\ |O\rangle &= |0\rangle, & E_O &= -\tfrac{2}{3}D \end{aligned} \qquad (2.4-2)$$

where the parameter α is determined by the relation $tan2\alpha = E/g_z\beta H_0$ (Abragam and Bleaney, 1970). When the applied field is parallel to the molecular z axis, the states $|+\rangle$ and $|-\rangle$ are orthogonal linear combinations of the $m_s = +1$ and $m_s = -1$ Zeeman basis states and the state $|O\rangle$ is simply equal to the $m_s = 0$ Zeeman state.

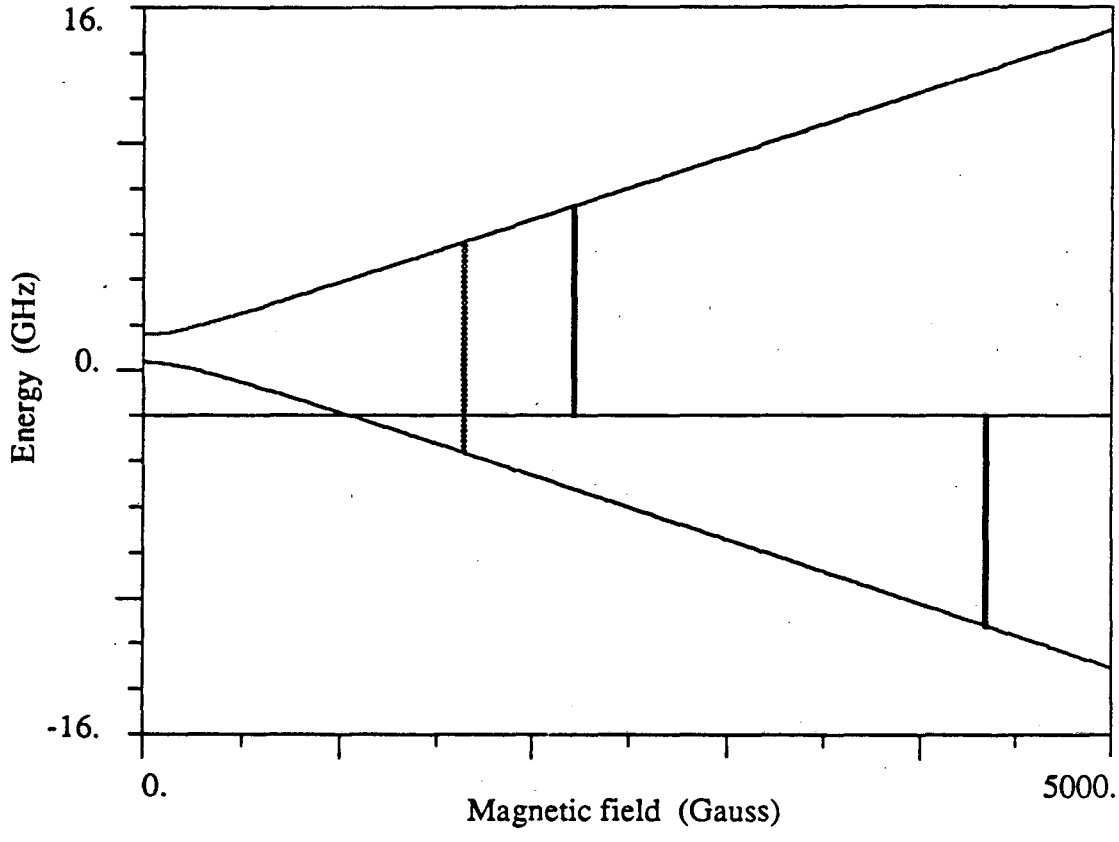

Figure 2.3. Energy levels and EPR transitions for an $S = 1$ spin state with the applied magnetic field along the z molecular axis. Spin Hamiltonian parameters: g = 2, D = 0.1 cm^{-1}, E = 0.02 cm^{-1}. Microwave frequency = 9.2 GHz. Solid lines: perpendicular polarization transitions, shaded line: parallel polarization transition.

The conventional choice for the spin quantization axis in a magnetic resonance experiment is to define the **z** axis as the direction of the applied magnetic field. In the usual geometry for EPR measurements, the microwave magnetic field $\mathbf{H_1}$ is polarized so as to be perpendicular to the applied magnetic field, and the direction of $\mathbf{H_1}$ may be taken as the **x** axis. The transition Hamiltonian for the perpendicular polarization is then proportional to the operator $S_x = \frac{1}{2}(S_+ + S_-)$ and induces transitions corresponding to the magnetic dipole selection rule $\Delta m = \pm 1$. For the $S = 1$ eigenstates listed above for the case in which the applied magnetic field is along the **z** molecular axis, two $\Delta m = \pm 1$ transitions are allowed. These occur between the $| O \rangle$ and $| + \rangle$ states and between the $| - \rangle$ and $| O \rangle$ states, and will appear at a g value near 2 if the zero-field splitting is very small compared to the Zeeman energy. These two transitions are shown as solid vertical lines in Figure 2.3.

Since the states $| + \rangle$ and $| - \rangle$ listed above contain admixtures of the same angular momentum eigenstates, a $\Delta m = 0$ transition is allowed between them. This transition may be induced by a microwave magnetic field parallel to the applied magnetic field, which corresponds to a transition Hamiltonian proportional to S_z. If the zero-field splitting is small compared to the Zeeman term, the $| - \rangle$ to $| + \rangle$ transition will occur at an effective g value of 4. As the zero-field splitting increases relative to the Zeeman energy, this transition will shift to lower field. Such transitions have sometimes been loosely referred to as "$\Delta m = 2$" transitions in the literature. This transition is shown as a shaded vertical line in Figure 2.3.

Figure 2.4 shows a comparison of the $S = 1$ energy levels and transitions when the applied magnetic field is oriented along each of the molecular principal axes. The magnitudes of the splittings corresponding to the transitions centered about g = 2

Figure 2.4. Comparison of the energy levels of an $S = 1$ spin state with the applied magnetic field along each of the molecular principal axes. Spin Hamiltonian parameters as in Figure 2.3. Solid lines: perpendicular polarization transitions, shaded lines: parallel polarization transitions.

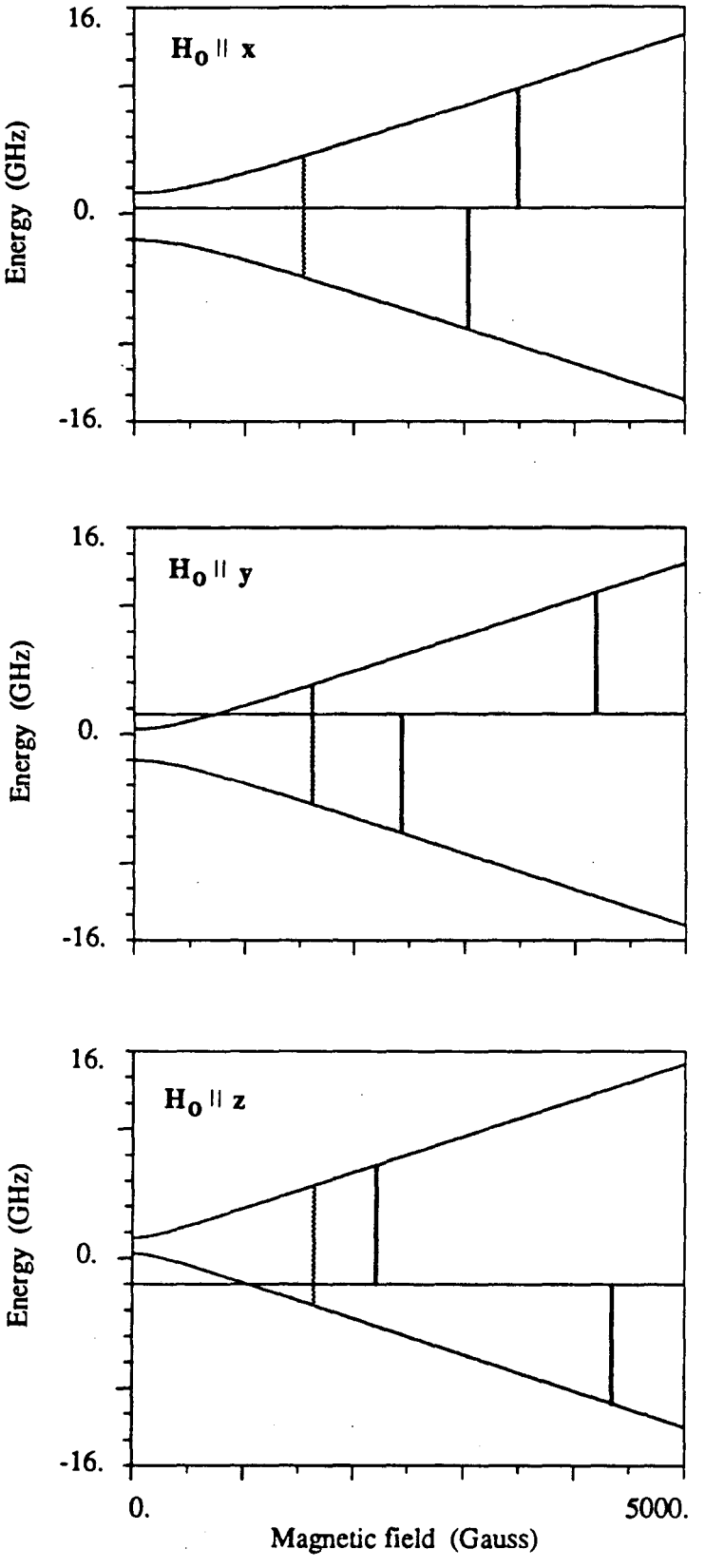
16.
$H_0 \parallel x$
0.
-16.
Energy (GHz)
16.
$H_0 \parallel y$
0.
-16.
Energy (GHz)
16.
$H_0 \parallel z$
0.
-16.
Energy (GHz)
0.
5000.
Magnetic field (Gauss)

are strongly dependent on orientation. In contrast, the splitting between the upper and lower states is less dependent on orientation, and the low-field transitions fall within a narrower field range. For molecular orientations in which the magnetic field is away from the molecular principal axes, the eigenstates will generally contain admixtures of $|m_s\rangle$ states so that perpendicular polarization transitions will also be allowed at low field. For a sample consisting of an ensemble of randomly oriented complexes, the perpendicular polarization EPR spectrum includes very broad and, therefore, low intensity transitions between $|-\rangle$ and $|O\rangle$ and between $|O\rangle$ and $|+\rangle$ spread over a broad range about g = 2, as well as the narrower low-field transition between the upper and lower states.

An alternate definition for the selection rules has sometimes been used in the interpretation of EPR spectra of non-Kramers spin states in which the zero-field Hamiltonian term is much larger than the Zeeman term. This definition amounts to taking the **z** molecular axis as the axis of quantization for the spin system. For a microwave magnetic field at a given direction with respect to the molecular axes, the transition probability between two states $|i\rangle$ and $|f\rangle$ is given by

$$P = \sum_{\nu=x,y,z} \gamma_\nu^2 \, |\langle f|S_\nu|i\rangle|^2 \qquad (2.4-3)$$

where γ_x, γ_y, and γ_z are the direction cosines of $\mathbf{H}_1$ relative to each of the molecular axes, and the spin operators are expressed in the molecular axis frame. An isotropic g tensor has been assumed. When the axis of quantization is taken as the molecular **z** axis, the "$\Delta m = 0$" selection rule corresponds to transitions induced by the component of $\mathbf{H}_1$ parallel to the molecular **z** axis, and the "$\Delta m = \pm 1$" selection rule refers to transitions induced by components of $\mathbf{H}_1$ perpendicular to this axis. As will be seen

in the following section, when the Zeeman term is sufficiently small to be treated as a perturbation on the levels of an isolated non-Kramers doublet, only the $\Delta m = 0$ transitions, as just defined, will be allowed, and these transitions may be observed with either microwave polarization. For $S = 1$ spin states arising from triplet states of organic molecules, the zero-field Hamiltonian terms are generally somewhat smaller than the Zeeman term at X-band microwave frequencies. For $S = 1$ systems containing transition metal ions of the first transition series, the zero-field terms are usually smaller than or comparable to the Zeeman term at X-band, as long as the ground electronic states are orbitally nondegenerate (see, for example, Wertz and Bolton, 1972). The Hamiltonian parameters for these systems generally do not fall in a limit where one of the terms may be treated as a perturbation on the other. When the zero-field and Zeeman terms are comparable in magnitude, powder spectra are most readily determined by numerical calculations, as will be discussed in Section 2.5. Clearly, the transitions predicted by the spin Hamiltonian formalism will not depend on the choice of the axis of quantization, as long as the static and transition Hamiltonian operators are defined in a consistent manner. Some of the original papers on integral spin EPR used a form for the Hamiltonian that does not have the appropriate symmetry properties (see Mueller, 1968, and references therein). The Hamiltonian may be accurately described by the Zeeman and zero-field terms discussed in Section 2.3.

Van der Waals and de Groot (1959, 1960) first discussed the origin of low field transitions in $S = 1$ spin states of organic molecules. A discussion of the analogous transitions in $I = 1$ NMR experiments has recently been presented using a perturbation treatment valid when the quadrupolar Hamiltonian term is small compared to the Zeeman term (Tycko and Opella, 1987). A parallel polarization EPR signal that is

assigned to an $S = 1$ spin state is discussed in Chapter 5.

2.4.B S = 2

The spin Hamiltonian for an $S = 2$ spin state includes the Zeeman and quadratic zero-field terms described previously, as well as the quartic crystal field terms discussed in Section 2.3. For $S = 2$ ions of the first transition series, the quadratic zero-field term is the dominant term in the Hamiltonian. The eigenstates and eigenvalues of the quadratic zero-field Hamiltonian for $S = 2$ may be expressed:

$$
\begin{aligned}
&|\,2^{s}\,\rangle = \tfrac{a^{+}}{\sqrt{2}}\{|+2\rangle + |-2\rangle\} + a^{-}|0\rangle, && E_{2^{s}} = 2(D^2 + 3E^2)^{1/2} \\
&|\,2^{a}\,\rangle = \tfrac{1}{\sqrt{2}}\{|+2\rangle - |-2\rangle\}, && E_{2^{a}} = 2D \\
&|\,1^{s}\,\rangle = \tfrac{1}{\sqrt{2}}\{|+1\rangle + |-1\rangle\}, && E_{1^{s}} = -D + 3E \\
&|\,1^{a}\,\rangle = \tfrac{1}{\sqrt{2}}\{|+1\rangle - |-1\rangle\}, && E_{1^{a}} = -D - 3E \\
&|\,0'\,\rangle = \tfrac{a^{-}}{\sqrt{2}}\{|+2\rangle + |-2\rangle\} - a^{+}|0\rangle, && E_{0'} = -2(D^2 + 3E^2)^{1/2}
\end{aligned}
\qquad (2.4-4)
$$

with

$$
a^{\pm} = \left[\frac{1}{2}\left(1 \pm \frac{D}{(D^2 + 3E^2)^{1/2}}\right)\right]^{1/2} \qquad (2.4-5)
$$

where the eigenstates are written in terms of the angular momentum eigenstates $|m_s\rangle$ with the z molecular axis as the axis of quantization (Tinkham, 1956). The $S = 2$ zero-field eigenstates may be grouped into two non-Kramers doublets, $|2^{\pm}\rangle$ and $|1^{\pm}\rangle$, and a singlet, $|0'\rangle$. The primary effect of the quartic crystal field term, Eqn. (2.3-3), is to increase the splitting between the levels of the $|2^{\pm}\rangle$ doublet by an amount equal to the Hamiltonian parameter a, and to shift the energies of the $|1^{\pm}\rangle$ doublet and the singlet levels.

For complexes of Mn(III), the value of the quadratic zero-field parameter D is expected to fall in the range $|D| = 1 - 4\ cm^{-1}$, and the quartic crystal field parameter a is expected to be relatively small. Figure 2.5 shows the $S = 2$ energy levels as a function of applied magnetic field for the case in which the applied magnetic field is parallel to the z molecular axis, using spin Hamiltonian parameters in the range appropriate for Mn(III). An X-band EPR transition ($h\nu \approx 0.3\ cm^{-1}$) may be detected between the levels of the $|2^{\pm}\rangle$ non-Kramers doublet if the splitting between the levels at zero field is less than the microwave frequency. For this molecular orientaion, only the parallel polarization transition is allowed between these levels. Typically, the splittings between the remaining levels of the $S = 2$ spin state are too large to be accessed with X-band microwave frequencies. Figure 2.6 shows a comparison of the $S = 2$ energy levels when the applied magnetic field is oriented along each of the molecular principal axes. The energy levels are seen to be highly anisotropic. In the molecular x-y plane, the splitting between the levels of the $|2^{\pm}\rangle$ doublet is relatively independent of the applied magnetic field, and EPR transitions may not be observed for these molecular orientations.

A perturbation treatment valid when the Zeeman term is small compared to the zero-field term and when the separation between the non-Kramers doublets is much larger than the intradoublet splitting has been developed and applied to the interpretation of EPR spectra of $S = 2$ Fe(II) ions in relatively high symmetry environments (Tinkham, 1956; Hendrich and Debrunner, 1989). Although these conditions may not rigorously apply to complexes of Mn(III), owing to the relatively smaller values of the zero-field parameter D, the results of this perturbation treatment may give some qualitative insight into the nature of the EPR transitions observed between the levels

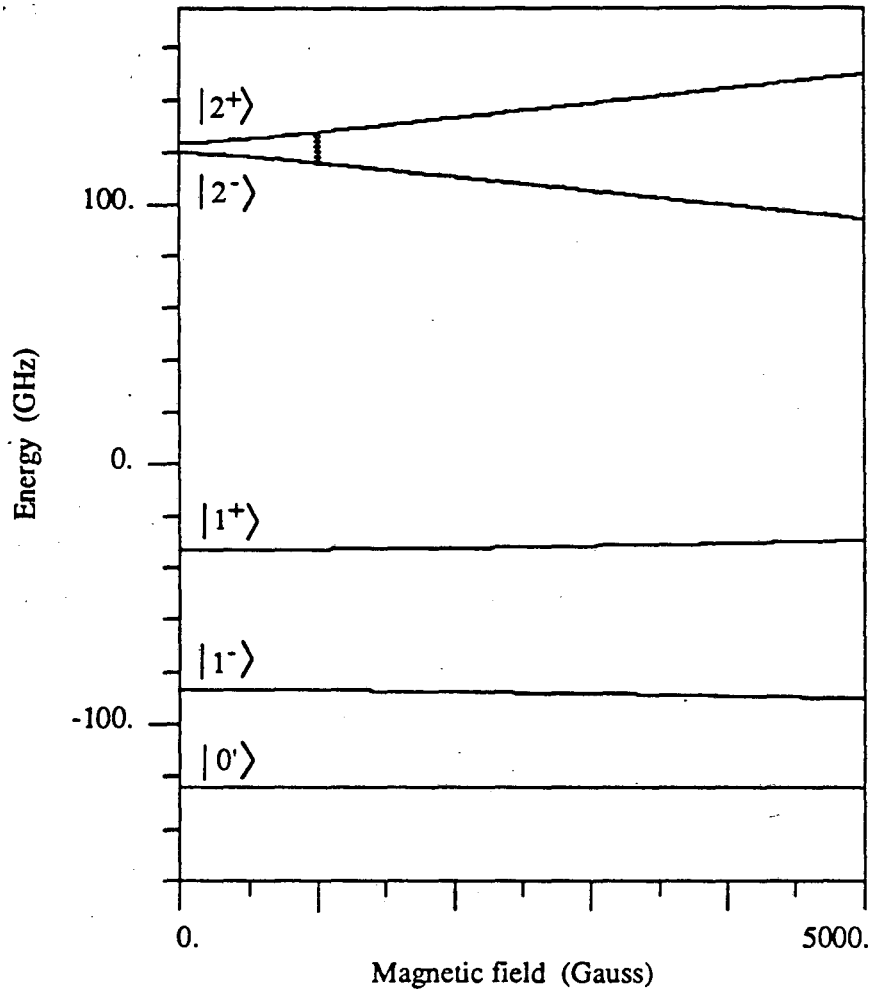

Figure 2.5. Energy levels and EPR transitions for an $S = 2$ spin state with the applied magnetic field along the **z** molecular axis. Spin Hamiltonian parameters: g = 2, D = 2.0 cm^{-1}, E = 0.3 cm^{-1}. Microwave frequency = 9.2 GHz. Only the parallel polarization EPR transition is allowed for this molecular orientation.

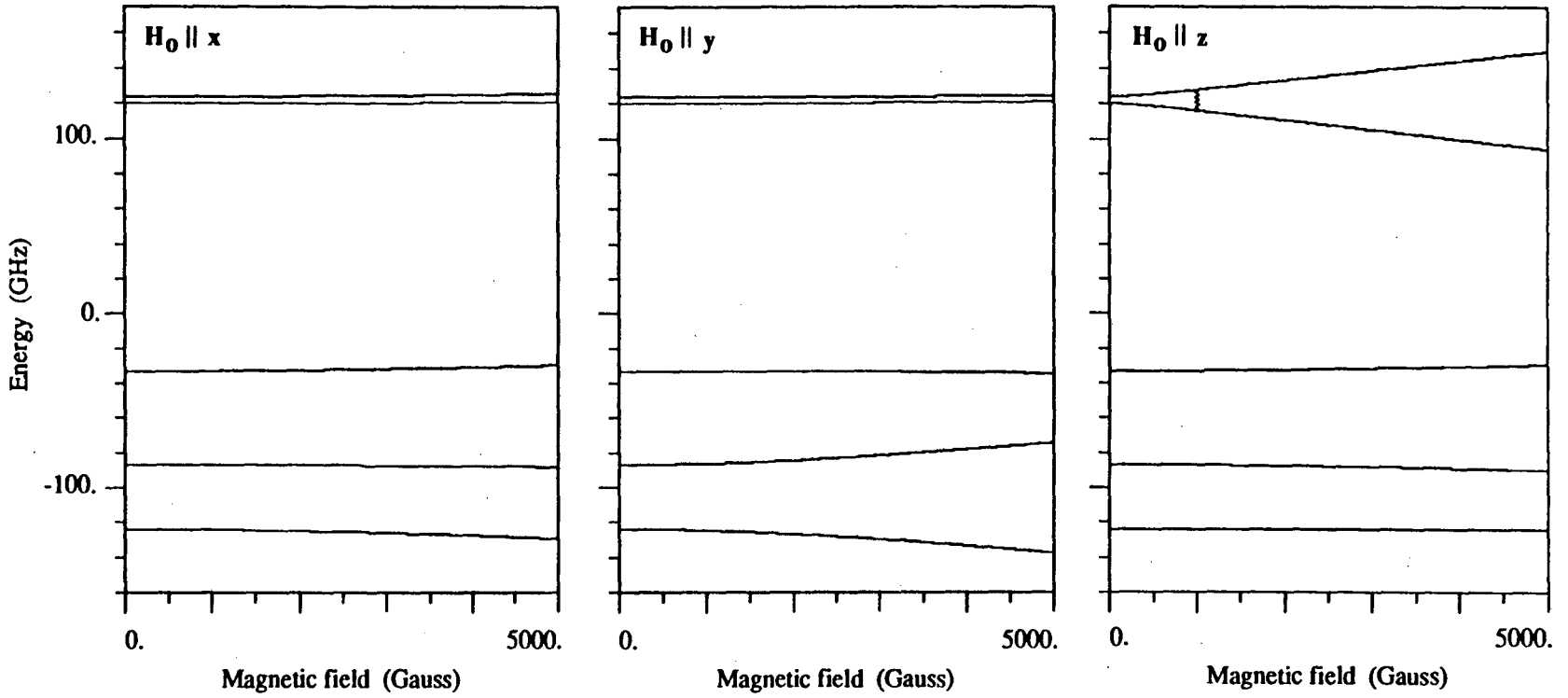

Figure 2.6. Comparison of the energy levels of an $S = 2$ spin state with the applied magnetic field along each of the molecular principal axes. Spin Hamiltonian parameters as in Figure 2.5.

of the $|2^{\pm}\rangle$ doublet in these systems.

The treatment takes the Zeeman term as a perturbation on the zero-field Hamiltonian eigenstates listed above, and relies on the assumption that the separation between the $|2^{\pm}\rangle$ doublet and the $|1^{\pm}\rangle$ doublet is sufficiently large that the Zeeman terms $g_x\beta H_0 S_x$ and $g_y\beta H_0 S_y$ will not introduce significant contributions to the eigenfunctions. The operators $S_x = \frac{1}{2}(S_+ + S_-)$ and $S_y = \frac{1}{2i}(S_+ - S_-)$ give nonzero matrix elements only between $|m_s\rangle$ states that differ by ± 1. The contributions to the $|2^{\pm}\rangle$ eigenfunctions from the admixture of the $|1^{\pm}\rangle$ states by the Zeeman terms proportional to S_x and S_y will be on the order of $g\beta H_0/D$. Since the $|2^s\rangle$ and $|2^a\rangle$ states are comprised of $|m_s\rangle$ states differing by $m_s = 0, \pm 2$, and ± 4, the Zeeman terms proportional to S_x and S_y will affect the intradoublet splitting only in second and higher order, giving contributions on the order of $(g\beta H_0/\Delta_0)^2$, where $\Delta_0 = 2[(D^2 + 3E^2)^{1/2} - D]$ is the unperturbed intradoublet splitting. If these effects may be neglected, the eigenfunctions of the $|2^{\pm}\rangle$ doublet may be expressed as a simple function of the applied field:

$$|2^{\pm}\rangle = \alpha^+|2^s\rangle \pm \alpha^-|2^a\rangle \qquad (2.4-6)$$

where

$$\alpha^{\pm} = \left[\frac{1}{2}\left(1 \pm \frac{\Delta_0^2}{(\Delta_0^2 + (\tilde{g}\beta H)^2)^{\frac{1}{2}}}\right)\right]^{\frac{1}{2}}, \qquad (2.4-7)$$

$$\tilde{g} = 4g_z a^+ \cos\theta, \qquad (2.4-8)$$

and θ is the angle between the applied field and the molecular z axis. The resonance condition has the simple form:

$$(h\nu)^2 = \Delta_0^2 + (4g_z\beta H_0 a^+ \cos\theta)^2. \qquad (2.4-9)$$

Given the form (2.4-3) for the transition probability, it can be seen that only the component of $\mathbf{H}_1$ parallel to the **z** molecular axis will induce transitions between the levels of the $|2^{\pm}\rangle$ doublet. These transitions may be observed in either microwave polarization, and the ratio of the signal intensities for the perpendicular and parallel polarizations is given by:

$$\frac{P_{\perp}}{P_{\parallel}} = \frac{1}{2}tan^2\theta \qquad (2.4-10)$$

Given the orientation dependence of the resonance condition, Eqn. (2.4-9), this factor results in different lineshapes for the two polarizations for samples consisting of randomly oriented molecules. Typically, the parallel polarization spectrum is narrower and more intense, while the perpendicular polarization spectrum is broader and extends to higher field.

The hyperfine interaction may also be incorporated in this perturbation treatment. Since only the **z** component of the spin contributes to the properties of the spin system in the perturbation limit, only the $A_z S_z I_z$ term of the hyperfine Hamiltonian, Eqn. (2.3-4), will contribute to the hyperfine interaction, and the resonance condition becomes:

$$(h\nu)^2 = \Delta_0^2 + (\tilde{g}\beta H_0 + \tilde{A}m_I)^2 \qquad (2.4-11)$$

(Baker and Bleaney, 1958). This predicts evenly spaced hyperfine components corresponding to A_z.

For $S = 2$ Mn(III) complexes, we expect that this perturbation treatment will qualitatively describe the nature of the EPR transitions within the $|2^{\pm}\rangle$ doublet. However, we expect that there may be some contribution to the transition probability from the admixture of the $|1^{\pm}\rangle$ states into the the $|2^{\pm}\rangle$ states, and that there may be some

additional orientation dependence in the resonance condtion resulting from the Zeeman terms proportional to S_x and S_y. EPR spectra of $S = 2$ spin states of Mn(III) complexes will be presented in Chapter 4 along with simulations based on an exact diagonalization of the spin Hamiltonian. Other limiting cases of $S = 2$ spin states have been discussed in the literature (Dowsing, 1970; Baranowski et al., 1979; Schwoerer et al., 1981).

2.4.C S = 5/2

The EPR properties of $S = 5/2$ spin states will be discussed briefly here because $S = 5/2$ Mn(II) species, which may be present as impurities in samples of Mn(III) systems, can also produce EPR features at low field in both the parallel and perpendicular microwave polarizations. The origin of these transitions can be understood by considering the simple case of an axially symmetric $S = 5/2$ state with a small quadratic zero-field parameter D, as discussed in Abragam and Bleaney (1970). In this case, the spin Hamiltonian is given by

$$H = \beta H_0(g_\perp S_x \sin\theta + g_\parallel S_z \cos\theta) + D[S_z^2 - \frac{1}{3}S(S+1)]. \qquad (2.4-12)$$

where θ is the angle between the applied field and the molecular symmetry axis. The Zeeman term may be diagonalized by a rotation by an angle ϕ about the y axis:

$$H = g\beta H_0 S_z' + \frac{1}{2}D[S_z'^2 - \frac{1}{3}S(S+1)](3\cos^2\phi - 1)$$

$$-D(S_x'S_z' + S_z'S_x')\cos\phi\sin\phi + \frac{1}{4}D(S_+'^2 + S_-'^2)\sin^2\phi. \qquad (2.4-13)$$

The last two terms of this Hamiltonian are off-diagonal. They may be treated as a perturbation on the Zeeman states, giving rise to matrix elements between $|m_s\rangle$

states differing by ±1 and ±2. The resulting admixtures of $|m_s\rangle$ states will produce transitions at g values corresponding to integral multiples of the main transition at $g \approx 2$, with intensities smaller by factors of $(D/g\beta H_0)^2$. Some of these transitions are forbidden when the applied field is parallel or perpendicular to the molecular symmetry axis; however, in a sample of randomly oriented molecules, the transitions may be observed in both the parallel and perpendicular microwave polarizations. More highly distorted complexes will give rise to more complicated EPR spectra, which may exhibit more intense features throughout the low-field region. A detailed account of predicted EPR transitions for $S = 5/2$ spin states for a wide range of zero-field parameters has been presented (Dowsing and Gibson, 1969), and the half-field spectra of Mn^{2+} in calcite have been discussed (Golding and Tennant, 1974).

2.5 Numerical simulation of high spin EPR spectra

The simulations presented in this thesis are based on an exact diagonalization of the spin Hamiltonian matrix. This approach is necessary when the spin Hamiltonian parameters fall in a regime in which perturbation treatments are not accurate. Simulations of field-swept EPR spectra were performed by diagonalizing the Hamiltonian at each of a series of magnetic field values. Since the samples consisted of randomly oriented centers, the Hamiltonian was diagonalized at each of a large number of orientations, and the resulting contributions to the spectrum were weighted by a factor of $\sin\theta$.

The Hamiltonian was constructed in the molecular principal axis frame. Given the input parameters S, g_x, g_y, g_z, D, E, and a, the zero-field terms were constructed as given by Eqns. (2.3-2) and (2.3-3). The Zeeman terms were computed using

field components $H_x = H_0 \sin\theta\cos\phi$, $H_y = H_0 \sin\theta\sin\phi$, and $H_z = H_0\cos\theta$. Given values for the microwave transition frequency and the transition linewidth, the differences between the Hamiltonian eigenvalues were tested for the resonance condition. If an energy difference fell within a given number of linewidths of the microwave frequency, the transition probabilites were computed and were weighted by the appropriate linewidth factor, assuming either a Gaussian or Lorentzian frequency function. Calculation of the resonances in terms of frequency rather than magnetic field obviated the use of the $dH_0/d\nu$ factor (Aasa and Vänngard, 1975) which diverges as $H_0 \rightarrow 0$ in the case of non-Kramers doublets with a nonzero intradoublet splitting. The parallel polarization transition probability was computed using a transition Hamiltonian $\beta\mathbf{H}_1\cdot\mathbf{g}\cdot\mathbf{S}$ with the components of $\mathbf{H}_1$ proportional to those of $\mathbf{H}_0$. For the perpendicular polarization spectrum, the transition probability was averaged over orientations of $\mathbf{H}_1$ in the plane perpendicular to $\mathbf{H}_0$. Derivatives of the simulated spectra were computed for comparison with experimental results.

3 Instrumentation

3.1 Introduction

The EPR measurements reported in this thesis were made using a Varian E-109 EPR spectrometer, which operates at X-band microwave frequencies and uses a homodyne detection system. Field-modulated spectra were obtained using a 100 kHz modulation frequency. The spectrometer was equipped with an Air Products Helitran liquid helium cryogenic system.

Two modifications of this spectrometer were made to perform most of the measurements. A bimodal microwave cavity, described in the following section, was used to allow observation of transitions in either the parallel or perpendicular polarization. Secondly, the detection sensitivity of the spectrometer was improved by modifying the microwave bridge to incorporate a low-noise GaAsFET microwave preamplifier. This modification assisted in the detection of weakly allowed transitions in dilute biological samples and is described in Section 3.3.

3.2 Bimodal microwave cavity

EPR measurements were made using a modified Varian V-4536 rectangular bimodal cavity. This cavity can be excited in either of two orthogonal TE_{102} modes: one having the conventional geometry in which the microwave field H_1 at the sample position is polarized perpendicular to the applied magnetic field, and the other with H_1 polarized parallel to the applied field. This arrangement allows conventional EPR signals to be monitored in the same experiment as the parallel polarization measurements. Figure 3.1a shows the magnetic field configuration used for the conventional perpendicular polarization. The sample tube is positioned vertically through the center

a. Perpendicular polarization

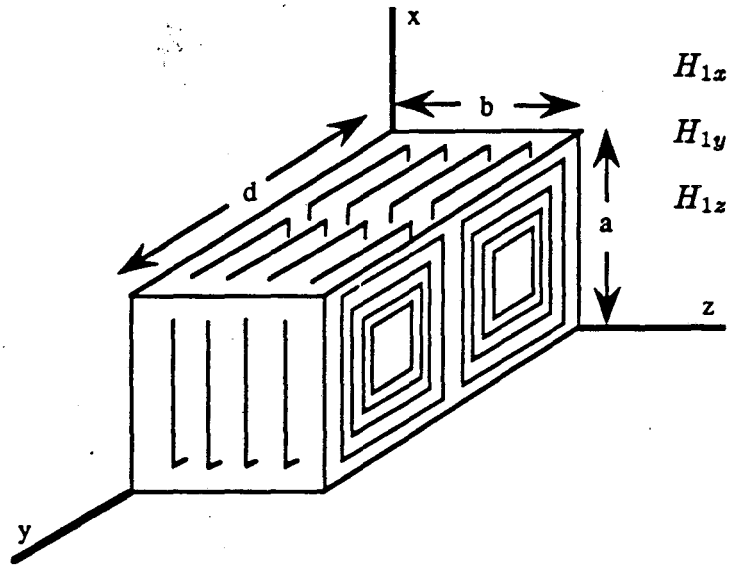

$$H_{1x} = -H_1 \frac{2a}{d} sin(\frac{\pi x}{a}) cos(\frac{2\pi y}{d})$$

$$H_{1y} = H_1 cos(\frac{\pi x}{a}) sin(\frac{2\pi y}{d})$$

$$H_{1z} = 0$$

b. Parallel polarization

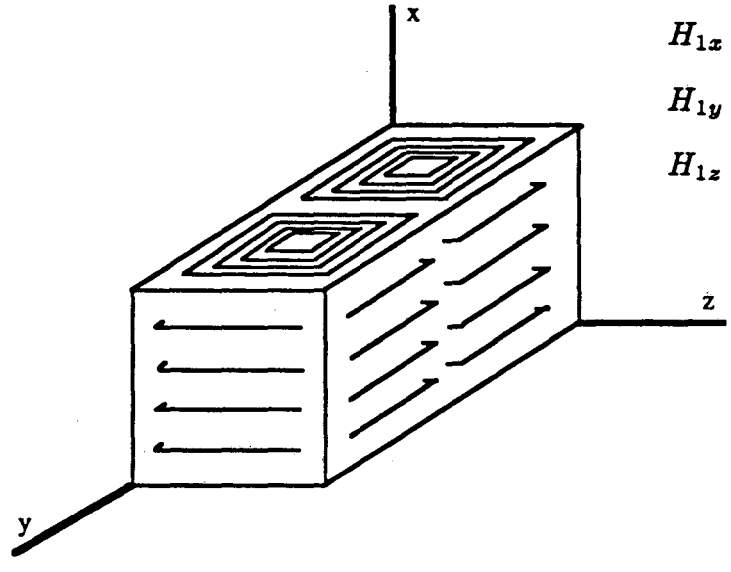

$$H_{1x} = 0$$

$$H_{1y} = H_1 sin(\frac{2\pi y}{d}) cos(\frac{\pi z}{b})$$

$$H_{1z} = -H_1 \frac{2b}{d} cos(\frac{2\pi y}{d}) sin(\frac{\pi z}{b})$$

Figure 3.1. Microwave magnetic field configurations in the two orthogonal TE_{102} modes of the bimodal microwave cavity. The cavity is positioned so that the applied magnetic field is parallel to the **z** axis. The sample is positioned vertically through the center of the cavity, parallel to the **x** axis.

of the cavity at the region of maximum H_1. In the bimodal cavity, the dimension b corresponding to the cavity width is sufficiently large to support an orthogonal TE_{102} mode. The magnetic field configuration of this mode is shown in Figure 3.1b. The H_1 field at the sample position is along the **z** direction, parallel to the direction of the applied magnetic field. The expressions for the microwave field components for the empty rectangular cavity are also given in Figure 3.1. In practice, the dielectric properties of the quartz dewar associated with the cryogenic system and the quartz sample tube, as well as the dielectric properties of the frozen solvent in the sample can significantly perturb the microwave field. The primary effect of this perturbation is to increase the magnitude of the H_1 field at the sample. Since the dielectic perturbation depends on the field geometry, the effect on H_1 is different for the two microwave polarizations.

The cavity was adapted for use in the E-109 spectrometer. To selectively excite one or the other of the two orthogonal TE_{102} modes, a waveguide-to-coax adaptor was fitted to either end of the cavity. One adaptor was oriented so as to launch the mode corresponding to the conventional perpendicular polarization, while the other was rotated by 90° so as to launch the orthogonal mode for the parallel polarization. An adjustable iris was placed between each adaptor and the body of the cavity to permit adjustment of the cavity coupling. The cavity was connected to the microwave bridge with a low-loss flexible microwave coaxial cable. Since the field modulation coils on the V-4536 cavity have a high impedance, a transformer and secondary amplifier were used at the output of the spectrometer field modulation amplifier to match the impedance for resonant excitation of the field modulation coils.

With the cryogenic system and sample tube in place, the resonant frequencies

are typically 9.20 GHz and 9.34 GHz, repsectively, for the parallel and perpendicular modes. Since the loaded Q for each mode is approximately 8000, the frequency separation of 140 MHz between the two modes is substantially larger than their frequency width. This high degree of isolation assures that each mode may be excited independently. However, the polarization of the microwave magnetic field throughout the sample volume in each of the modes is not perfect, in that field components with an orthogonal polarization are present to a small degree in each of the cavity modes. In the cavity mode corresponding to the parallel polarization, signals resulting from perpendicular field components appear attenuated by a factor of more than 100 from their amplitude in the orthogonal cavity mode.

3.3 GaAsFET microwave preamplifier

To improve the sensitivity of the spectrometer for measurements at low to moderate microwave power levels, the microwave brige was modified to incorporate a low noise microwave preamplifier. The noise figure of an EPR spectrometer can be expressed in a manner analogous to that of a series of cascaded amplifiers. For such a series of amplifiers of noise figure F_i and gain G_i, the noise figure is given by (Poole, 1983)

$$F = F_1 + \frac{F_2 - 1}{G_1} + \frac{F_3 - 1}{G_1 G_2} + ... + \frac{F_n - 1}{G_1 G_2 ... G_{n-1}}. \qquad (3.3 - 1)$$

Since the overall noise figure is dominated by stages preceding the first stage of high gain, addition of a low noise preamplifier before an initial stage of high noise figure can significantly improve the overall noise figure.

The Varian E-102 X-band EPR spectrometer bridge includes a low noise klystron and a homodyne detection system with a reference arm and a Ge backward-type diode

detector. At low incident microwave power, the dominant noise contribution is from the detector, and the spectrometer output noise remains independent of microwave power. Although klystron AM noise is negligible, klystron FM noise can be converted to AM signal noise by the cavity frequency response. As the incident microwave power is increased, the FM noise increases and becomes the dominant noise contribution at very high microwave power. For the E-102 bridge operating in absorption mode with the standard E-231 cavity, the transition between these two regimes occurs at a microwave power of about 100 mW (Varian EPR System Manual, Vol. 1, Varian Instrument Division, Palo Alto, CA). Signal processing electronics subsequent to the microwave components make a comparatively small contribution to the overall spectrometer output noise.

An EPR spectrometer differs from the series of cascaded amplifiers described by Eqn. 3.3-1 in that components that precede the generation of the signal can contribute to the total noise at the output. The most significant such contribution is klystron FM noise conversion, and this can be accounted for by an initial stage with a power dependent noise figure and signal gain of unity (Poole, 1983). Since the noise at low microwave power is dominated by the detector (F_{diode} = 9 dB, typical, 13 dB, maximum, rated at 0.1 mW), installation of a low noise microwave preamplifier immediately preceding the detector can improve the spectrometer sensitivity in this power regime. In principle, a preamplifier should improve the sensitivity for incident microwave powers lower than those for which the klystron FM noise dominates the preamplifier noise. Since the conversion of FM noise to AM signal noise is nonlinear (Meijer, 1975), the presence of the preamplifier will degrade the spectrometer performance as the power exceeds this limit. In practice, the increased signal level produced by the microwave

preamplifier can lead to instability of the klystron automatic frequency control (AFC) loop, resulting in decreased spectrometer performance at powers lower than those determined by intrinsic klystron FM noise. To circumvent this problem, the AFC circuit was also modified.

A MITEQ (Hauppauge, New York) model AMF-2S-8895-30-S low noise GaAs-FET amplifier was used for the detector preamplifier. The amplifier has a 2.8 dB noise figure, 20 dB gain, and a 100 mW maximum input power rating within the frequency range of the klystron, 8.8 - 9.5 GHz. The output power at the 1-dB gain compression point of the amplifier is greater than 40 mW, which is more than sufficiently high to avoid distortion of EPR signals. The amplifier was installed using a solenoid-activated transfer switch that allowed the amplifier to be taken out of the bridge circuit for initial tune-up and for high power spectrometer operation. The spectrometer bridge components with the addition of the preamplifier and transfer switch are shown in Figure 3.2.

The E-102 bridge AFC system operates at a 70 kHz klystron reflector voltage modulation frequency. The video signal from the microwave diode detector is preamplified in the reference arm assembly and is sent both to the console receiver module for detection as a field-modulated EPR signal and to a 70 kHz tuned amplifier for the AFC system. The AFC error signal is generated by phase sensitive detection of the amplified AFC signal against a 70 kHz reference signal and is applied to the reflector regulator. The overall gain of the AFC loop depends both on the gain of the AFC amplifier and on the amplitude of the 70 kHz component of the microwave signal reflected from the cavity, which in turn depends on the amplitude of the 70 kHz klystron modulation, the incident microwave power, the Q of the cavity, and, if present, the

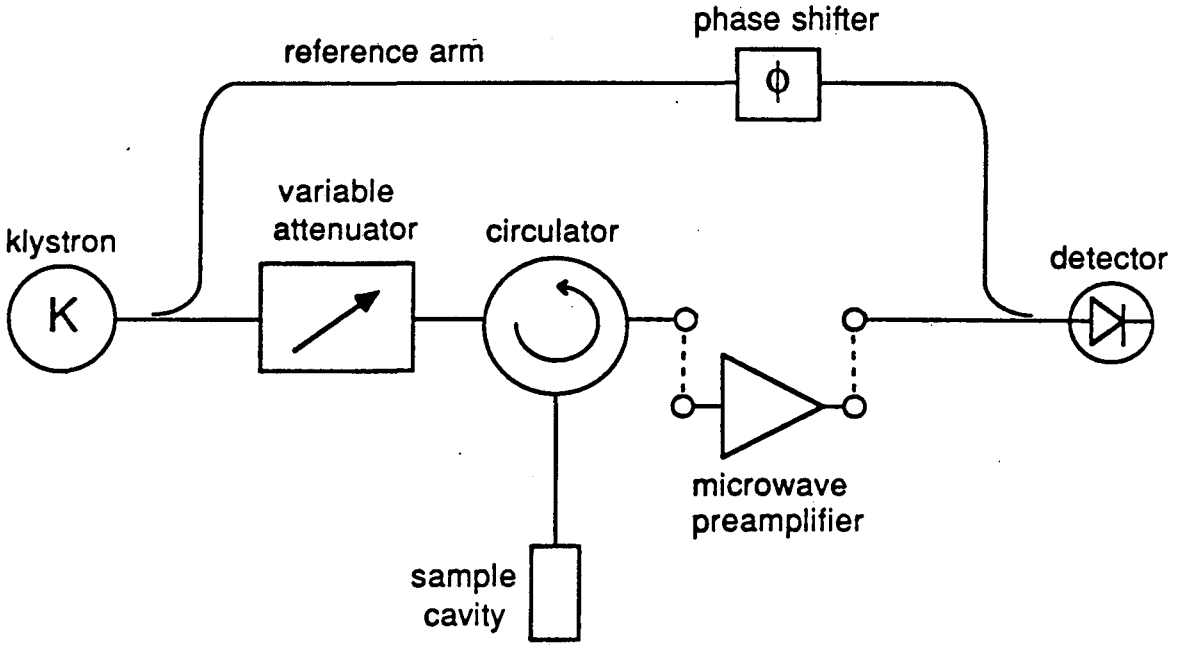

Figure 3.2. Primary microwave bridge components with the addition of the microwave preamplifier.

gain of the microwave preamplifier. To compensate for the increase in AFC loop gain with microwave power, the klystron modulation amplitude is decreased via a resistive network that includes a potentiometer mechanically linked to the attenuation control. The modulation amplitude may be further adjusted over a limited range by the front-panel AFC modulation control. A straightforward means of compensating for the increased AFC loop gain from the microwave preamplifier and, thereby, eliminating the resulting AFC loop instabilities is to reduce the gain of the 70 kHz AFC amplifier when the preamplifier is in use. Details of the modification of the AFC circuit and the results of test procedures on the modified bridge have been published (Dexheimer and Klein, 1988).

Addition of the preamplifier improves the spectrometer sensitivity by a factor of two for microwave power levels lower than 3 mW. As the microwave power is increased, conversion of klystron FM noise becomes a more significant contribution to the total spectrometer noise, and the improvement in sensitivity decreases and results in degradation of the spectrometer performance for power levels greater than $\approx$ 25 mW. Modification of the AFC circuit to compensate for the increased signal gain from the preamplifier eliminates AFC instabilities that would result in degradation of spectrometer performance at lower microwave powers. The improvement of the spectrometer sensitivity at low to moderate microwave power levels is useful for detecting EPR signals from species in which power saturation effects preclude the use of high microwave power levels. In particular, the use of the GaAsFET microwave preamplifier significantly reduced the signal averaging time required to obtain spectra of the dilute biological samples discussed in Chapter 5.

4 EPR spectra of inorganic Mn(III) complexes

4.1 Introduction

This chapter discusses the detection and interpretation of EPR spectra of inorganic Mn(III) complexes. The presence of trivalent manganese is implicated in a number of redox active metalloenzymes, including the photosynthetic oxygen-evolving complex, superoxide dismutase (Fee et al., 1976; Ludwig et al., 1986), pseudocatalase (Kono and Fridovich, 1983; Beyer and Fridovich, 1985), and ribonucleotide reductase (Willing et al., 1988). Considerable effort has been focussed on the synthesis and characterization of inorganic complexes as structural models for these biological metal centers (reviewed in Pecoraro, 1988). However, EPR spectroscopy has rarely been applied to study the electronic structure of trivalent manganese complexes. This is perhaps a result of a prevalent assumption that the non-Kramers spin states of such systems would be EPR silent, either as a result of large zero-field splittings or fast spin relaxation processes. Although a few EPR studies of trivalent manganese impurity ions in solid state systems have been reported (Gerritsen and Sabisky, 1963; Anderson et al., 1972; Aurbach et al., 1975), these have relied largely on indirect detection methods or very high observation frequencies.

The results presented in this chapter demonstrate the utility of X-band EPR for studying the electronic structure of complexes of Mn(III) and provide examples of spectral features observable in integer spin states of these systems. Interpretation of the spectra provides insight into the electronic structure of Mn(III) centers that may be applied to the understanding of biological systems and to the understanding of the single ion contributions to the properties of exchange-coupled mixed-valence complexes that contain Mn(III). Sections 4.2 and 4.3 discuss the EPR spectra of $S = 2$ spin

states of the mononuclear Mn(III) tris-acetylacetonate and tris-picolinate coordination complexes. Section 4.4 discusses the EPR spectra of the weakly antiferromagnetically exchange coupled binuclear complex $Mn_2(III,III)O(O_2CCH_3)_2(HB(pz)_3)_2$ ($HB(pz)_3$ = hydrotris(1-pyrazolyl) borate).

4.2 Mn(III) tris-acetylacetonate

The Mn(III) ion in the tris-acetylacetonate complex $Mn(O_2C_5H_7)_3$ has a pseudooctahedral coordination, with six oxygen neighbors provided by the three bidentate acetylacetonate groups. The structure of the dominant β crystal form has been determined by X-ray diffraction studies (Fackler and Avdeef, 1974). The Jahn-Teller distortion for this complex takes the form of a tetragonal compression. The two average Mn-O bond distances are 1.95 and 2.00 Å. Magnetic susceptibility measurements (Gregson et al., 1978) confirm that the complex has an $S = 2$ ground spin state. Interpretation of the susceptibility data assuming a spin Hamiltonian with axially symmetric Zeeman and quadratic zero-field terms gives values of g = 2.00 and D = +3.1 $\pm$ 0.1 cm^{-1} for the Hamiltonian parameters.

The X-band EPR spectra of a frozen solution of Mn(III) tris-acetylacetonate in a mixture of butyronitrile and propionitrile are shown in Figure 4.1. A low field feature centered at an effective g value of 8.7 is present in the parallel polarization, and a broader feature at slightly higher field appears in the perpendicular polarization. The field positions of the signals are consistent with transitions within the $|2^{\pm}\rangle$ non-Kramers doublet, and the lineshapes are consistent with the different orientation dependence for the two polarizations. Partially resolved hyperfine structure with a spacing of 55 G appears in the parallel polarization signal.

EPR spectral simulations were performed as outlined in Section 2.5. An $S = 2$ spin

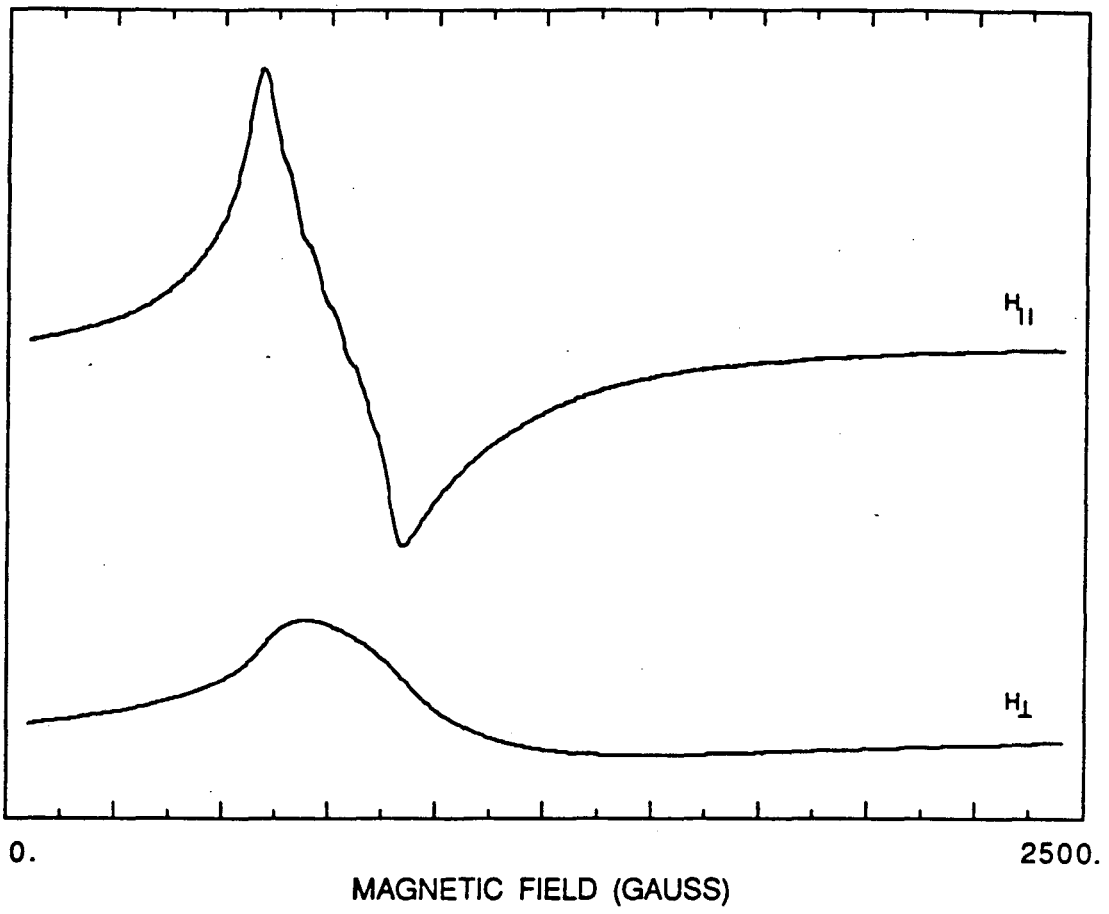

Figure 4.1. X-band EPR spectra of Mn(III) tris-acetylacetonate in butyronitrile/propionitrile. Upper trace: parallel polarization, lower trace: perpendicular polarization. Spectrometer conditions: microwave frequency, 9.20 GHz (parallel polarization), 9.34 GHz (perpendicular polarization); microwave power, 2 mW; field modulation amplitude, 20 G; modulation frequency, 100 kHz; temperature, 12 K.

state was assumed, and since Mn(III) g tensors are expected to be relatively isotropic, as discussed in Section 2.3, the g tensor values were fixed at $g_x = g_y = g_z = 2$. In the initial simulations, the hyperfine structure was neglected. The zero-field parameter D was fixed at the value D = +3.1 cm^{-1} determined by the magnetic susceptibility analysis, and the value of E was varied in order to match the simulated spectra with the field positions of the signals. Figure 4.2 shows the simulated spectra with the parameters listed above and E = 0.42 cm^{-1}. The simulation accurately reproduces the field positions of both the parallel and perpendicular polarization features and qualitatively predicts the spectral lineshapes.

For the purposes of this calculation, a Gaussian frequency function with a width of 2800 MHz was assumed for the transition linewidth. In practice, the EPR lineshapes are dominated by inhomogeneous broadening due to variations in the zero-field parameters, which result from random strains in centers present in frozen solution. The distribution in values of D and E translates into a distribution of intradoublet splittings for the $|2^{\pm}\rangle$ non-Kramers doublet, and the distribution of intradoublet splittings gives rise in turn to a distribution in the resonant field position for a given orientation of the complex. A variety of functional forms have been assumed for these distributions (see, for example, Hagen, 1982; Levin and Brill, 1988; Hendrich and Debrunner, 1989). However, the physical origin of these distributions derives from variations in the magnitude and symmetry of the potential seen by ions in differing environments, and these variations are not related to the spin Hamiltonian parameters in a straightforward manner. As a result, the assumption of any simple functional form for these distributions can only be expected to qualitatively reproduce the observed EPR lineshape. In the spectra of the Mn(III) tris-acetylacetonate complex, the hyperfine structure, discussed

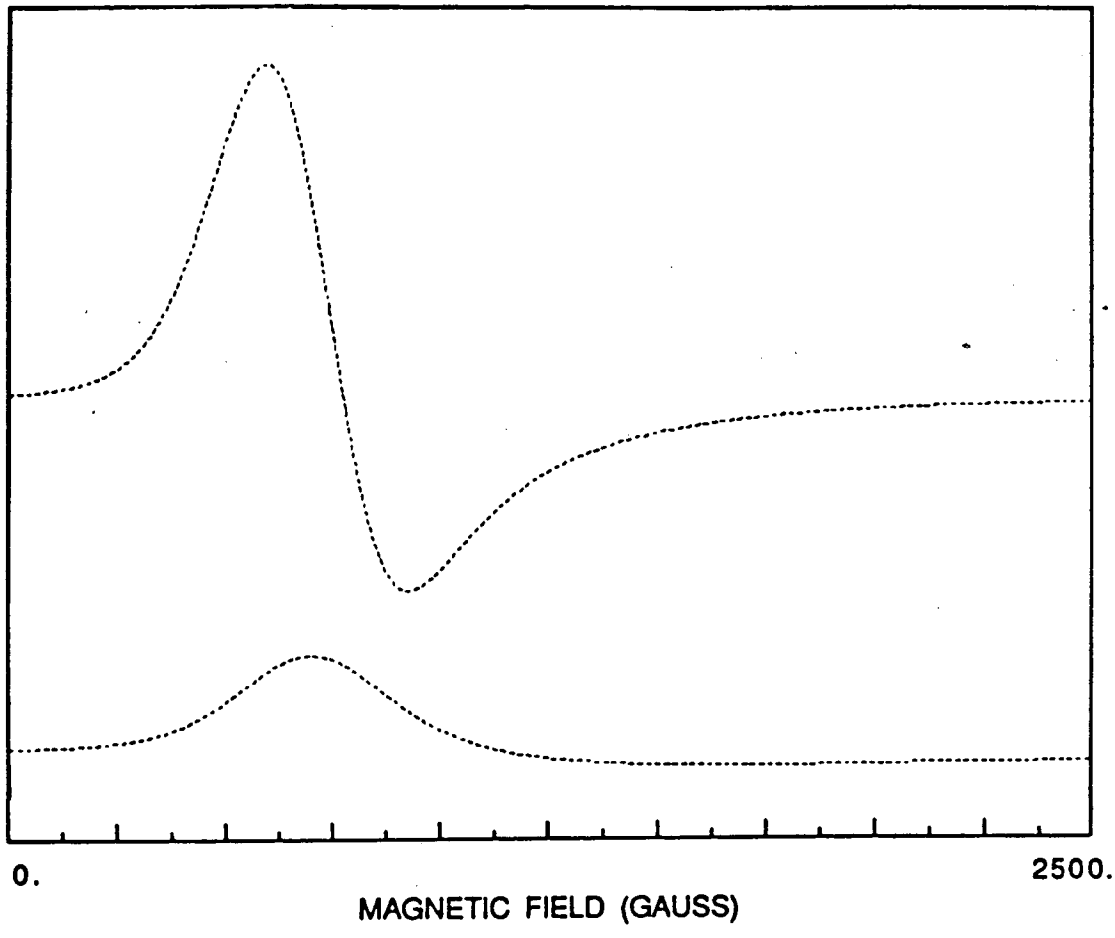

Figure 4.2. Numerical simulation of the EPR spectra of Mn(III) tris-acetylacetonate. Upper trace: parallel polarization, lower trace: perpendicular polarization. Simulation parameters: $g_x = g_y = g_z = 2$, D = 3.1 cm^{-1}, E = 0.42 cm^{-1}. See text for details.

below, also contributes to the observed lineshape. However, even when the hyperfine structure is included in the simulation, neither Gaussian nor Lorentzian lineshape functions reproduce the shape of the wings of the spectrum, indicating that the distribution of zero-field parameters significantly influences the spectral lineshape.

The simulation parameters used in Figure 4.2 correspond to a value of $\Delta_0 \approx 2[(D^2 + 3E^2)^{1/2} - D] + a = 0.168$ cm^{-1} for the intradoublet splitting for the $|2^{\pm}\rangle$ non-Kramers doublet. Most treatments of the magnetic properties of $S = 2$ spin states of first-row transition metal ions neglect the quartic Hamiltonian term; however, it is interesting to note that EPR measurements on Mn(III) impurity ions in rutile (TiO_2) indicate a suprisingly large value for the quartic crystal field parameter a (Gerritsen and Sabisky, 1963). The impurity ion study was conducted on a single crystal sample using sufficiently high microwave frequencies that a number of transitions between different levels of the $S = 2$ spin state could be observed for various crystal orientations. This allowed an independent determination of the Hamiltonian parameters D = -3.4 cm^{-1}, E = 0.116 cm^{-1}, and $a = 0.13$ cm^{-1}. Simulations of the X-band Mn(III) tris-acetylacetonate spectra using values of D, E, and a different from those used for Figure 4.2 produced similar results as long as the $|2^{\pm}\rangle$ intradoublet splitting remained constant. This result stands in contrast to the EPR properties of $S = 2$ Fe(II) complexes, in which the Hamiltonian parameters g_x, D, and E can, in principle, be determined from the $|2^{\pm}\rangle$ resonance as long as the quartic Hamiltonian term is negligible. This is due to the electronic properties of the $3d^6$ Fe(II) $S = 2$ states, which, unlike the $3d^4$ Mn(III) states, have g tensor values that may differ substantially from the free electron g value. For a $3d^6$ ion in rhombic symmetry, the deviations from the free electron g values are directly related to the values of the quadratic zero-field parameters, allowing a self-

consistent choice of Hamiltonian parameters. In practice, these parameters cannot always be determined uniquely from simulations (see, for example, Hendrich and Debrunner, 1989), in part because of complications from the effect of the distribution of Hamiltonian parameters on the signal lineshape and perhaps because of contributions from the quartic spin Hamiltonian term.

Figure 4.3 shows an expanded view of the I = 5/2 ^{55}Mn hyperfine structure present in the Mn(III) tris-acetylacetonate parallel polarization spectrum. The signal is displayed as a second derivative to enhance the spectral features. Also shown in Figure 4.3 are the results of a simulation based on diagonalization of a Hamiltonian including the hyperfine term $S \cdot A \cdot I$. A narrower linewidth was chosen for the hyperfine simulation to enhance the resolution of the hyperfine components. The simulation parameter A_x = 154 MHz corresponds to a splitting of 55 G. As predicted by the perturbation treatment discussed in Section 2.4.B, the simulated spectrum is insensitive to the values of the hyperfine tensor components A_x and A_y. The broader lineshapes resulting from the orientation dependence of the perpendicular polarization transitions preclude the resolution of hyperfine structure in the perpendicular polarization spectrum. Since the magnitude of the isotropic part $\frac{1}{3}(A_x + A_y + A_z)$ of the Mn(III) hyperfine interaction is expected to be intermediate between those of Mn(II) and Mn(IV) (Al'tshuler and Kozyrev, 1974), the observed spacing indicates the degree of anisotropy that may be present in the hyperfine tensors of Mn(III) complexes.

Care must be exercised in the assignment of low field EPR features to Mn(III) species. As discussed in Section 2.4.C, low symmetry $S = 5/2$ Mn(II) species, which may be present as impurities in Mn(III) preparations, can also give rise to EPR features at low field. Since S = 2 Mn(III) signals are quite weak if present at all, a small

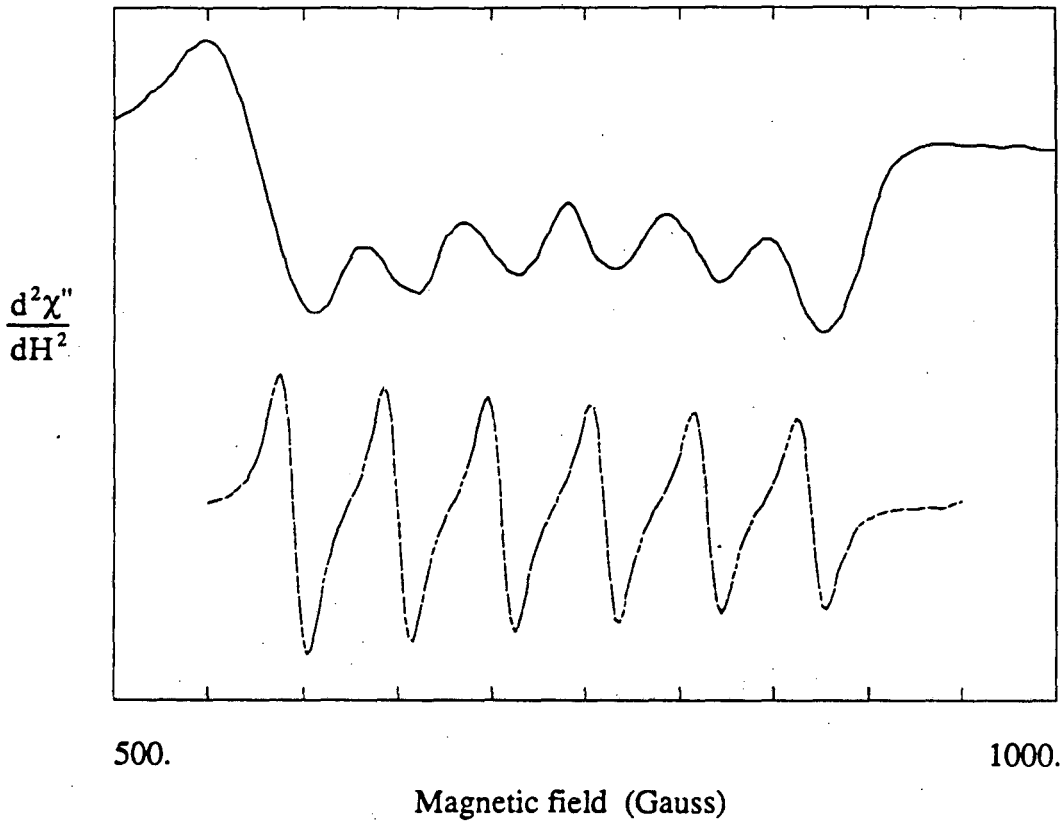

Figure 4.3. Upper trace: Expanded view of the I = 5/2 ^{55}Mn hyperfine structure in the parallel polarization Mn(III) tris-acetylacetonate spectrum, presented as a second derivative to enhance the spectral features. Each minimum in the second derivative spectrum corresponds to the center of a hyperfine component. Lower trace: Second derivative presentation of a numerical simulation of the hyperfine structure, using a narrow linewidth to enhance the resolution. The hyperfine tensor component A_z = 154 MHz corresponds to the hyperfine spacing of 55 G.

amount of an Mn(II) impurity can easily interfere with the identification of an Mn(III) signal. To minimize impurities from other oxidation states, the solutions of the Mn(III) complexes were prepared in a dry box using dry solvents. Degassing the solutions eliminated background signals from paramagnetic oxygen. Mn(II) impurities may be distinguished from Mn(III) species because the $S = 5/2$ system will in general produce a resonance near g = 2 in addition to any other features at low field. In preliminary preparations of the Mn(III) complexes, features near g = 2 were observed in addition to the low field signals. Upon further purification, the amplitudes of the g = 2 signals decreased markedly relative to the low field features. This result, together with the consistency of the field positions and lineshapes of the low field features with an $S = 2$ spin Hamiltonian, provides additional confirmation of the assignment of the signals to Mn(III).

4.3 Mn(III) tris-picolinate

The Mn(III) tris-picolinate complex $Mn(C_5H_4NCO_2)_3$ (Yamaguchi and Sawyer, 1985) contains an Mn(III) ion in pseudoocthedral coordination, with one nitrogen and one oxygen neighbor provided by each of the three bidentate picolinate groups. The X-ray crystal structure (Figgis et al., 1978) indicates a tetragonal elongation with nitrogen atoms in the axial positions.

The X-band EPR spectra of a frozen solution of Mn(III) tris-picolinate in acetonitrile are shown in Figure 4.4. The parallel polarization signal consists of a trough with a minimum at an effective g value of 10, and the perpendicular polarization signal appears as a broader trough at higher field. The field positions are again consistent with transitions within the $|2^{\pm}\rangle$ non-Kramers doublet. The lineshapes are similar to those observed in a number of $S = 2$ Fe(II) complexes (Hagen, 1982; Hendrich and

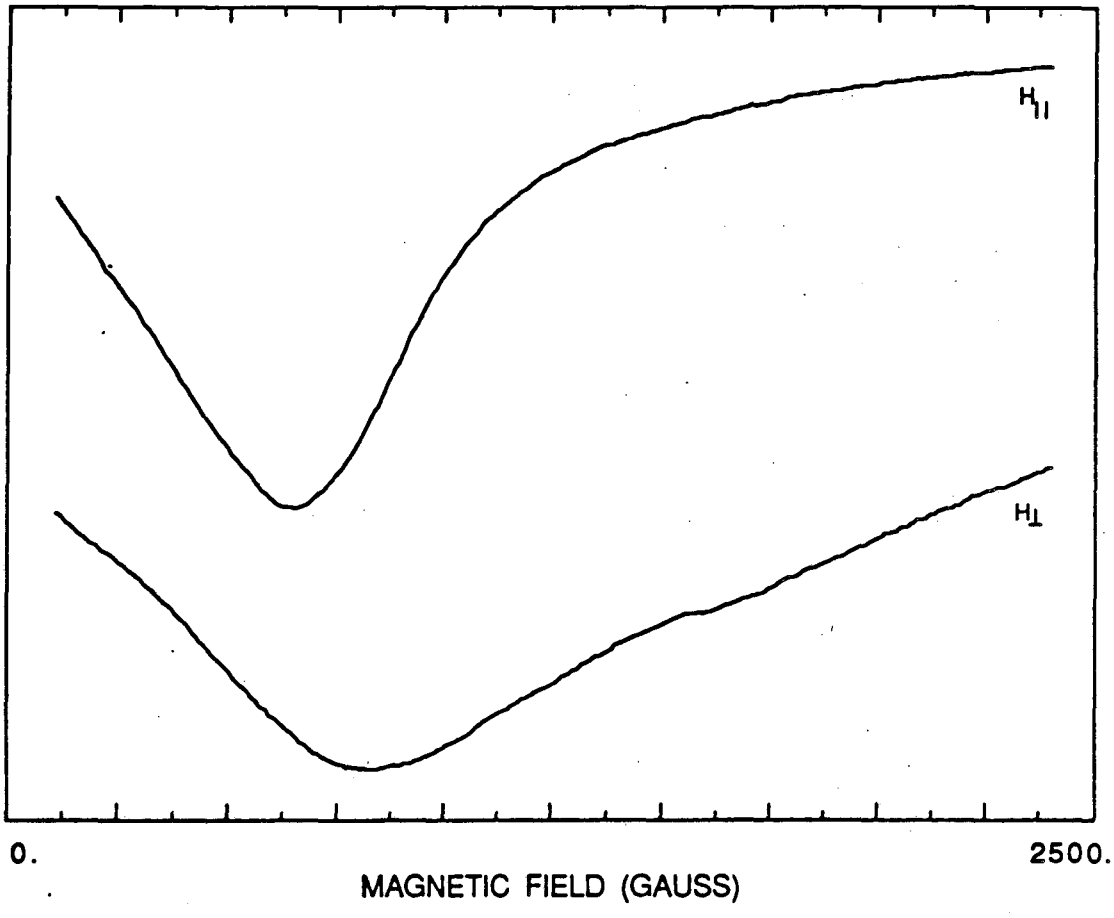

Figure 4.4. X-band EPR spectra of Mn(III) tris-picolinate in acetonitrile. Upper trace: parallel polarization, lower trace: perpendicular polarization. Spectrometer conditions: as in Figure 4.1, except microwave power, 20 mW; temperature, 7 K.

Debrunner, 1988, 1989). These lineshapes appear in field-modulated first derivative EPR spectra when the width of the resonance, which results from the distribution of zero-field parameters, is sufficiently large relative to its field position. For this system, the large spectral width results in part from the poor quality of the glass produced by frozen acetonitrile; however, the tris-picolinate complex was not stable in better glass-producing solvents. No hyperfine structure was resolved in the spectra.

Figure 4.5 shows a simulation with spin Hamiltonian parameters $S = 2$, $g_x = g_y = g_z = 2$, and zero-field parameters corresponding to a $|2^{\pm}\rangle$ intradoublet splitting of 0.31 cm^{-1}. A Gaussian frequency function with a width of 5300 MHz was assumed for the transition linewidth. The simulation accurately predicts the field positions of the minima in both the parallel and perpendicular polarization spectra, and qualitatively reproduces the spectral lineshapes.

4.4 $Mn_2(III,III)O(O_2CCH_3)_2(HB(pz)_3)_2$

The binuclear complex $Mn_2(III,III)O(O_2CCH_3)_2(HB(pz)_3)_2$ ($HB(pz)_3$ = hydrotris (1-pyrazolyl)borate) (Sheats et al., 1987) contains two six-coordinate Mn(III) ions bridged by one oxo and two acetate groups. The remaining coordination sites are filled by nitrogen atoms of the tridentate $HB(pz)_3^-$ ligands. The molecular structure was determined by X-ray diffraction methods for two crystal forms of the complex, which contained either one or four molecules of acetonitrile solvent per molecule of the binuclear complex. The distance between the manganese ions was determined to be 3.159 ±0.001 Åand 3.175 ±0.001 Å, respectively, for these two crystal forms. Both crystal structures show that, in each of the manganese sites, the Mn-O bond corresponding to the oxo- bridge and the Mn-N bond trans to this bridge are shorter than the remaining metal-ligand bonds, indicating that the empty d_{z^2} orbital is di-

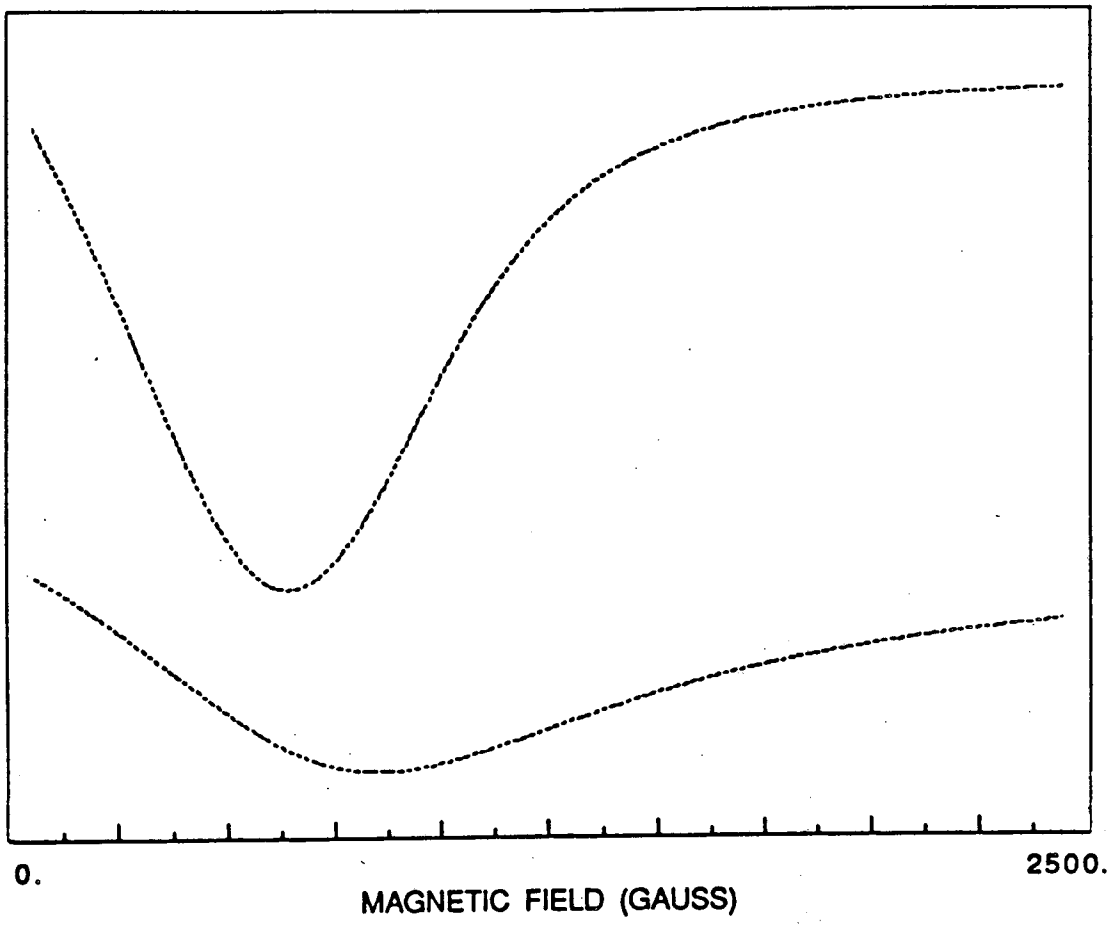

Figure 4.5. Numerical simulation of the EPR spectra of Mn(III) tris-picolinate. Upper trace: parallel polarization, lower trace: perpendicular polarization. Simulation parameters: $S = 2$, $g_x = g_y = g_z = 2$, $|2^{\pm}\rangle$ intradoublet splitting = 0.31 cm^{-1}, Gaussian frequency width = 5300 MHz.

rected along the Mn-O_{oxo} bond axis. The remaining metal-ligand bond distances are inequivalent, leading to an overall rhombic symmetry at the metal sites.

Magnetic susceptibility measurements on this complex verify that the Mn(III) ions are in high spin $S = 2$ states. Measurements on powdered samples of the two crystal forms gave slightly different results at low temperature. Sheats et al. quote values of J $\approx$ -0.2 to -0.7 cm^{-1} for the isotropic exchange coupling constant, based on fits of the temperature dependent susceptibility data to an expression derived from the Hamiltonian $H_{ex} = -2JS_1 \cdot S_2$, but they note that a good simulation of the data was not possible over the entire temperature range. As discussed in Section 2.3, the single ion quadratic zero-field parameters D and E and the dipolar interaction between the ions may also be expected to contribute to the magnetic properties of the exchange-coupled complex; however, these effects will be correlated with those of the isotropic exchange in fits of powder susceptibility data, making a precise analysis difficult. Assuming that the ions may be treated as point dipoles, the dipolar coupling constant from Eqn. (2.3-8) takes the value $D_d = -g^2\beta^2/r^3$ = -0.05 cm^{-1}. The electron-withdrawing character of the $HB(pz)_3^-$ ligands may lead to a reduction of this estimate. Since the crystal structure indicates a rhombic symmetry for the metal sites, the single ion D and E values are both expected to be nonzero.

The small value of the exchange coupling determined by the susceptibility analysis is consistent with a proposed mechanism for superexchange in this and similar systems. Bossek et al. (1989) have suggested that the dominant superexchange pathway in μ-oxo-di-μ-acetato bridged metal complexes involves interactions of the d_{z^2} and d_{xz} orbitals mediated by the oxo bridge. Since the d_{z^2} orbital is empty in the Mn(III) complexes, this mechanism will be ineffective and the coupling is expected to

be small. Susceptibility measurements on other binuclear Mn(III) complexes with the same bridging structure but different terminal ligands indicate a weak antiferromagnetic coupling J = -6.8 cm^{-1} in the case of bipyridal ligands (Menage et al., 1988) and a small ferromagnetic coupling in the case of triazacyclononane ligands (Wieghardt et al., 1986), consistent with this prediction. The weak antiferromagnetic exchange interaction in the $Mn_2(III,III)O(O_2CCH_3)_2(HB(pz)_3)_2$ complex results in an $S = 0$ ground spin state and low-lying excited states of integral spin that are thermally accessible at liquid helium temperature.

Figure 4.6 shows the spectra of the binuclear complex $Mn_2(III,III)O(O_2CCH_3)_2(HB(pz)_3)_2$ in a mixture of butyronitrile and propionitrile. The observed signals are consistent with a formal $S = 2$ state. A trough with a minimum at an effective g of 8.7 appears in the parallel polarization, and a weaker, broader trough appears at higher field in the perpendicular polarization. Partially resolved hyperfine structure with a spacing of 52 G is visible in the parallel polarization spectrum, and the multiplicity of hyperfine components is consistent with an exchange-coupled dimer as the origin of the signal. The absence of any signals corresponding to an $S = 1$ state may be explained by sufficiently large zero-field splitting parameters. This would lead to highly anisotropic and, therefore, very weak perpendicular polarization transitions between the $|\ O\ \rangle$ and $|\ +\ \rangle$ and the $|\ -\ \rangle$ and $|\ O\ \rangle$ levels of the $S = 1$ state, and could also preclude the observation of a half-field X-band transition between the $|\ +\ \rangle$ and $|\ -\ \rangle$ levels in either the perpendicular or parallel polarization. Figure 4.7 shows a simulation with spin Hamiltonian parameters $S = 2$, $g_x = g_y = g_z = 2$, and zero-field parameters corresponding to a $|2^{\pm}\rangle$ intradoublet splitting of 0.275 cm^{-1}. A Gaussian frequency function with a width of 5600 MHz was assumed for the transition

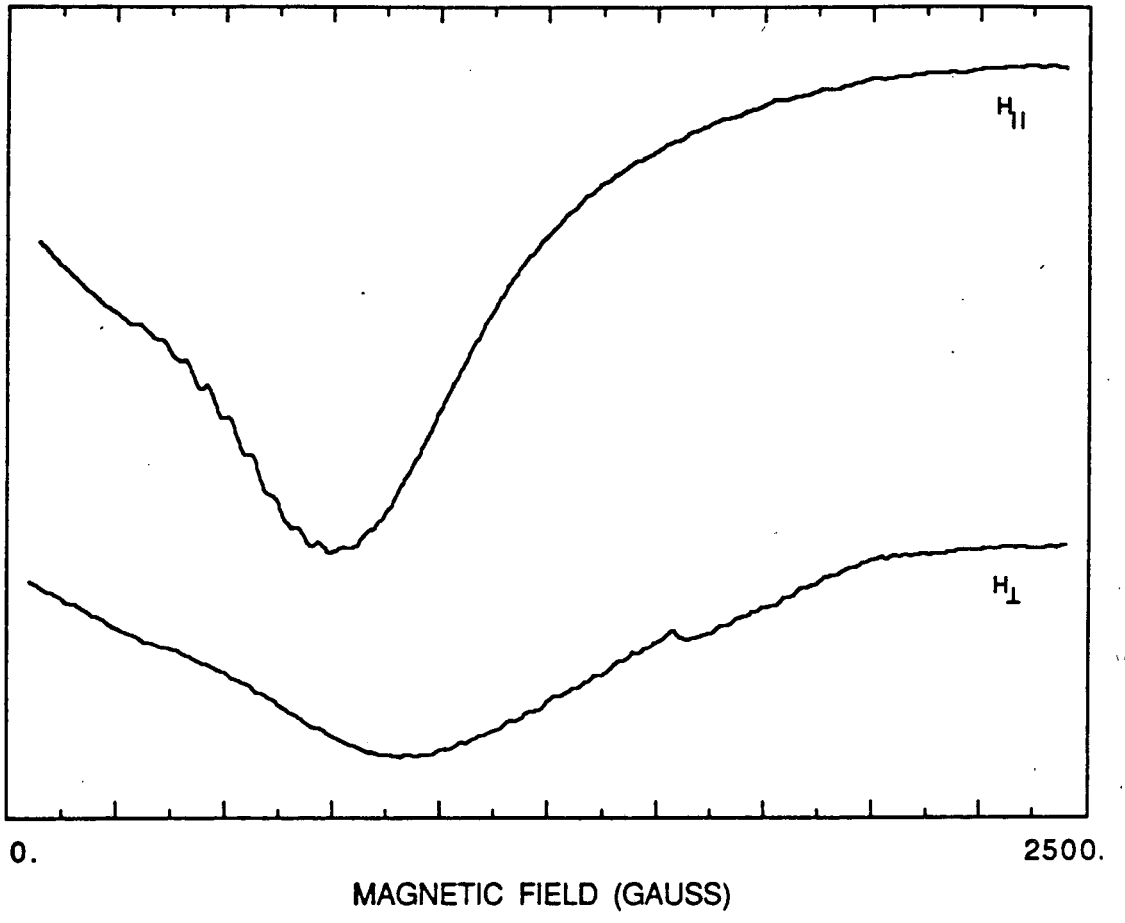

Figure 4.6. X-band EPR spectra of $Mn(III,III)O(O_2CCH_3)_2(HB(pz)_3)_2$ ($HB(pz)_3$ = hydrotris(1-pyrazolyl)borate) in butyronitrile/propionitrile. Upper trace: parallel polarization, lower trace: perpendicular polarization. Spectrometer conditions: as in Figure 4.1, except temperature, 4.2 K. A small signal due to an Fe(III) impurity is present at an effective g of 4.3 in the perpendicular polarization.

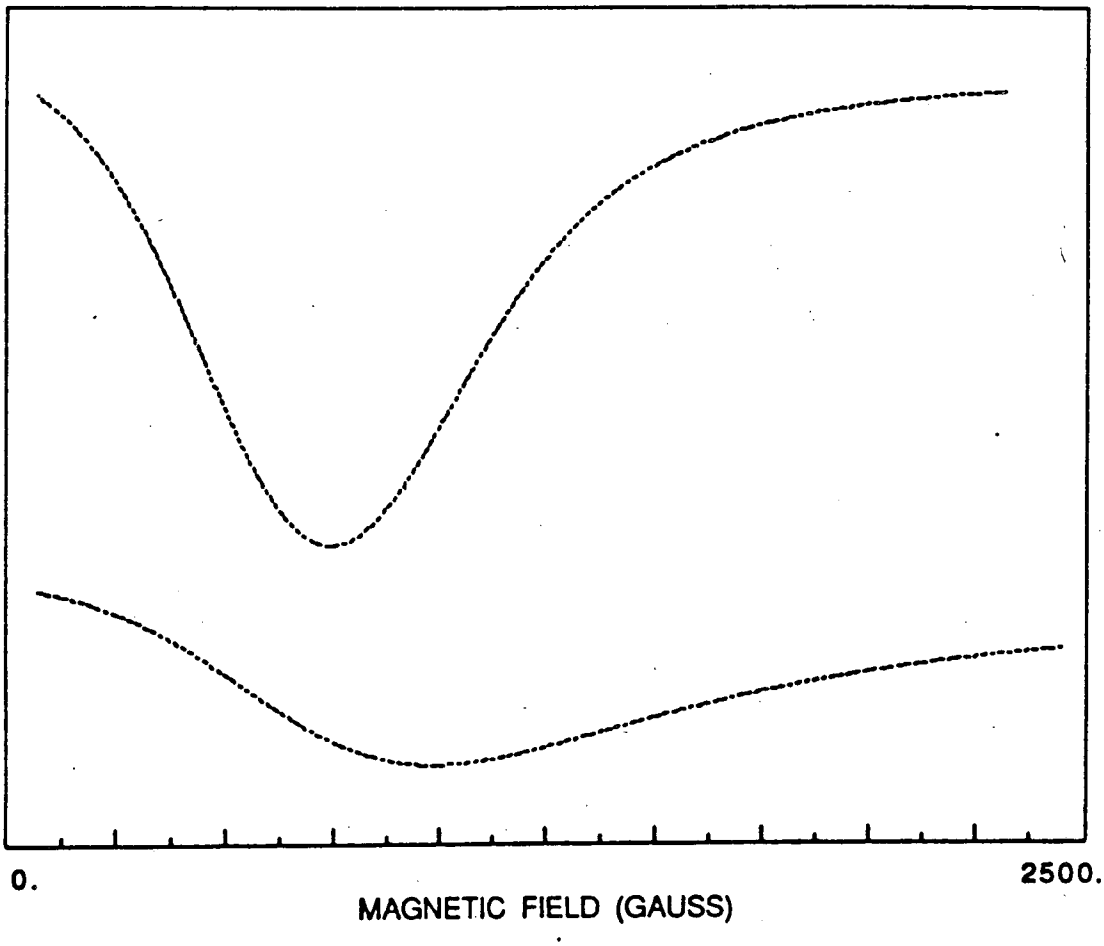

Figure 4.7. Numerical simulation of the EPR spectra of the binuclear complex Mn_2(III,III) $O(O_2CCH_3)_2$ $(HB(pz)_3)_2$. Upper trace: parallel polarization, lower trace: perpendicular polarization. Simulation parameters: $S = 2$, $g_x = g_y = g_z = 2$, $|2^{\pm}\rangle$ intradoublet splitting = 0.275 cm^{-1}, Gaussian frequency width = 5600 MHz.

linewidth.

Figure 4.8a shows an expanded view of the hyperfine structure present in the parallel polarization spectrum. To remove the spectral curvature resulting from the underlying signal shape, Figure 4.8b displays the difference between the observed spectrum and a data set that has been smoothed over a sufficiently large field range to average out the hyperfine structure. When the isotropic exchange coupling is large compared to the single ion hyperfine interaction A_i, the EPR spectrum of a coupled pair of identical ions will consist of $4I_i + 1$ hyperfine lines with a spacing $A_i/2$ (Griffith, 1972; Owen and Harris, 1972). For two nuclear spins $I_i = 5/2$, the relative intensities of the eleven hyperfine lines will be 1:2:3:4:5:6:5:4:3:2:1, corresponding to the number of ways of contructing each m_I value in the coupled system. Within the signal-to-noise, the hyperfine components in the parallel polarization spectrum follow this characteristic pattern.

The hyperfine spacing of 52 G observed in the spectrum of the binuclear complex corresponds to an effective single ion hyperfine value much larger than that observed in the Mn(III) tris-acetylacetonate complex. As seen in Section 4.2, Mn(III) hyperfine tensors may be quite anisotropic, and the parallel polarization EPR spectrum is sensitive only to the z component of the hyperfine tensor. Because of the bridging structure of the $Mn_2(III,III)O(O_2CCH_3)_2(HB(pz)_3)_2$ complex, the principal axes of the individual Mn(III) ions are not parallel, and the z axis for the dipolar interaction, which corresponds to the line joining the ions, does not coincide with any of the single ion principal axes. Although the lack of knowledge of the single ion magnetic parameters does not allow a direct prediction of the properties of the coupled system, it is clear that the principal axes for the coupled spin state will differ from those of the individ-

Figure 4.8 a. Expanded view of the hyperfine structure in the parallel polarization spectrum of the exchange coupled binuclear complex $Mn_2(III,III)O(O_2CCH_3)_2(HB(pz)_3)_2$.

b. Hyperfine structure in the absence of the curvature due to the underlying signal shape, determined by taking the difference between the spectrum shown in (**a**) and a data set smoothed over a sufficiently large field range to average out the hyperfine structure. The positions of eleven hyperfine components are marked in the field range 300 - 850 G. Features outside this field range are due to noise and are not reproducible.

a.

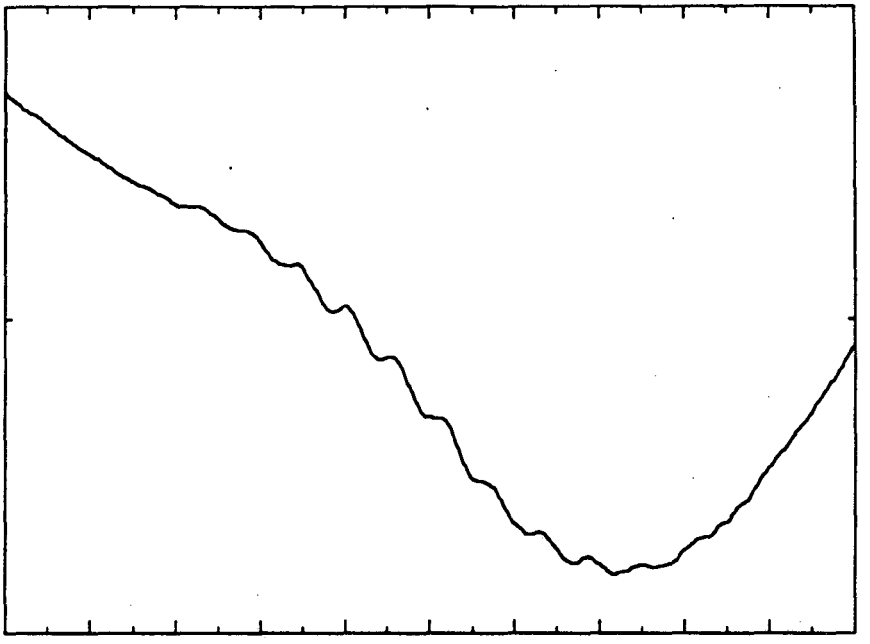
100.
1000.
Magnetic field (Gauss)

b.

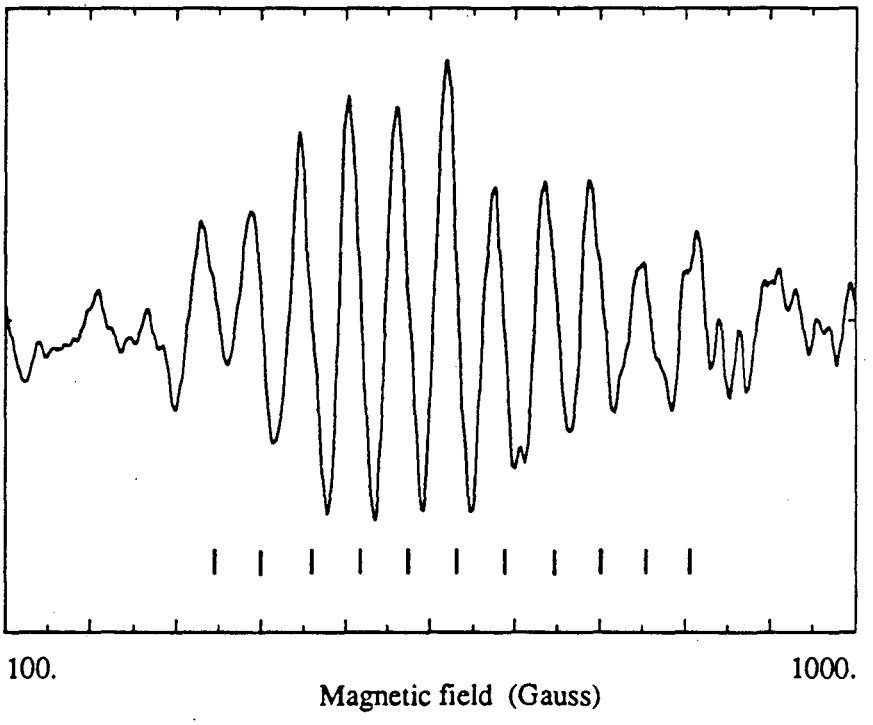
100.
1000.
Magnetic field (Gauss)

ual ions. As a result, the z component of the hyperfine tensor for the coupled system may include contributions from the A_x and A_y components, as well as the smaller A_z component, of the individual ion hyperfine tensors, producing a larger effective A_z component for the coupled system.

Recent reports (Nishida, 1988a,b) have assigned multicomponent EPR signals centered at g = 2 to integer spin states of exchange-coupled binuclear Mn_2(III,III) complexes; however, the structure and properties of these signals indicate that they arise from impurities corresponding to the Mn_2(III,IV) oxidation states of the complexes. In the measurements reported here, a small amount of an Mn_2(III,IV) impurity produced a multiline signal centered near g = 2 that decreased in amplitude relative to the low field features upon further purification. The low field features corresponding to the Mn_2(III,III) complex were observed only at temperatures below 30 K.

The Mn_2(III,III)$O(O_2CCH_3)_2$ $(HB(pz)_3)_2$ complex has been proposed as a model for the bridging structure of the binuclear Mn(III) sites in pseudocatalase and Mn-ribonucleotide reductase (Sheats et al., 1987). The detection of EPR signals from this model complex suggests the possibility of using EPR to study these biological centers.

5 Parallel polarization EPR studies of Photosystem II

5.1 Introduction

This chapter discusses the detection of a paramagnetic intermediate in the S_1 state of the photosynthetic oxygen-evolving complex and its implications for the structure of the redox-active manganese centers. The application of parallel polarization EPR to the oxygen-evolving complex was motivated by experimental evidence, including the presence of half-integral spin EPR signals in the S_2 state and the indication from X-ray edge studies of a one-electron oxidation of manganese in the S_1 to S_2 transition, that suggests the presence of a paramagnetic species of integral spin in the S_1 state.

The following section discusses the detection of the paramagnetic intermediate, and Section 5.3 discusses control experiments that allow the assignment of the parallel polarization EPR signal to manganese in the oxygen-evolving complex. The relationship between the parallel polarization signal in the S_1 state and the multiline and $g = 4.1$ signals in the S_2 state is explained in Section 5.4. A computer simulation of the parallel polarization EPR spectrum is presented in Section 5.5. Finally, the implications of these results are discussed in Section 5.6.

5.2 Detection of a paramagnetic intermediate in the S_1 state of the oxygen-evolving complex

PS II-enriched thylakoid membranes were prepared from spinach using a Triton X-100 fractionation procedure (Berthold et al., 1981). The preparations used in this study had a high level of activity, as demonstrated by measured values of at least 600 μmol O_2/mg chlorophyll/hr for the rate of oxygen evolution under continuous illumination at room temperature. Since adventitious Mn^{2+} can produce background signals in the

parallel polarization, care was exercised during the sample preparation procedure to avoid manganese release, and the resulting PS II-enriched membranes were washed first in sucrose buffer (400 mM sucrose; 50 mM 4-morpholineethanesulfonic acid (MES), pH 6; 15 mM NaCl; 5 mM $MgCl_2$) containing 1.5 mM EDTA and again in sucrose buffer containing 20 mM $CaCl_2$. The second wash in the presence of excess Ca^{2+} was performed because Ca^{2+} has been found to displace Mn^{2+} that may be non-specifically bound to membrane surfaces (Theg and Sayre, 1979). The final pellet was suspended in either sucrose buffer or glycerol buffer (50 mM MES, pH 6; 15 mM NaCl; 5 mM $MgCl_2$; 50 % (v/v) glycerol) to a final chlorophyll concentration of approximately 10 mg/ml. To avoid variable background features from paramagnetic condensed oxygen, the last two washes, final resuspension, and sample tube loading were performed under an argon atmosphere using degassed buffers. Samples were poised in the S_1 state by dark adaptation at 4 °C for at least one hour prior to freezing at 77 K and were later advanced to the S_2 state by illumination at low temperature (Brudvig et al., 1983).

Figure 5.1a shows the dark-adapted minus 200 K illuminated difference spectrum in the parallel polarization. A weak, broad feature is present at low field in the S_1 state and disappears upon advancement to the S_2 state by illumination for 5 min at 200 K. The signal appears at an effective g value of approximately 4.8, and has a peak-to-peak width of roughly 600 G. Since the photosynthetic samples are relatively dilute in manganese and parallel polarization signals are expected to be weak, signal averaging was used to improve the sensitivity. For the signal shown in Figure 5.1a, 25 four-minute scans were averaged both before and after illumination. Since temperature fluctuations may significantly distort the signal baseline, the cryogenic system was

Figure 5.1. EPR difference signals observed in the $S_1 \rightarrow S_2$ transition.

a. The parallel polarization EPR signal associated with the S_1 state of the oxygen-evolving complex, as observed in the dark-adapted minus 200 K illuminated difference spectrum of a Photosystem II preparation. The signal appears at an effective g value of approximately 4.8 and has a peak-to-peak width of approximately 600 G. Irregular features apparent in the signal are not reproducible. Spectrometer conditions: microwave frequency, 9.19 GHz; microwave power, 3 mW; temperature, 4.2 K; field modulation, 20 G at 100 KHz; scan time, 4 min; time constant 2 s. Twenty-five scans were averaged both before and after illumination, and a GaAsFET microwave preamplifier was used to improve the sensitivity.

b. The g = 4.1 and multiline conventional EPR signals associated with the S_2 state of the oxygen-evolving complex, as observed in the 200 K illuminated minus dark-adapted difference spectrum. Spectrometer conditions: microwave frequency, 9.34 GHz; microwave power, 0.5 mW; temperature, 4.2 K; field modulation, 20 G at 100 KHz; scan time, 4 min; time constant 0.25 s.

a.

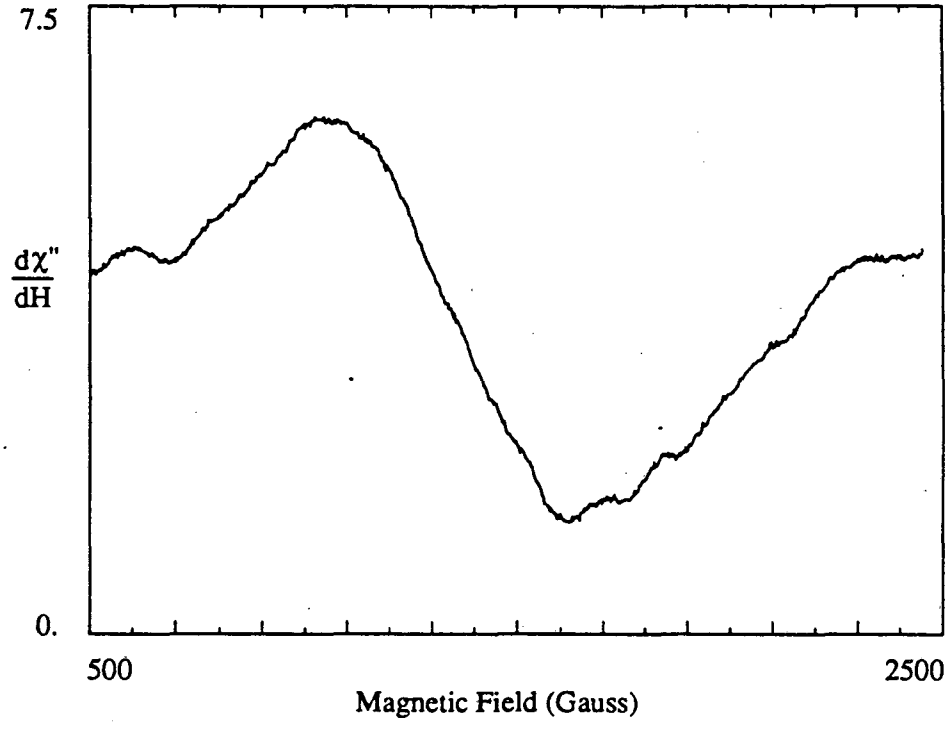
7.5
dχ"/dH
0.
500
2500
Magnetic Field (Gauss)

b.

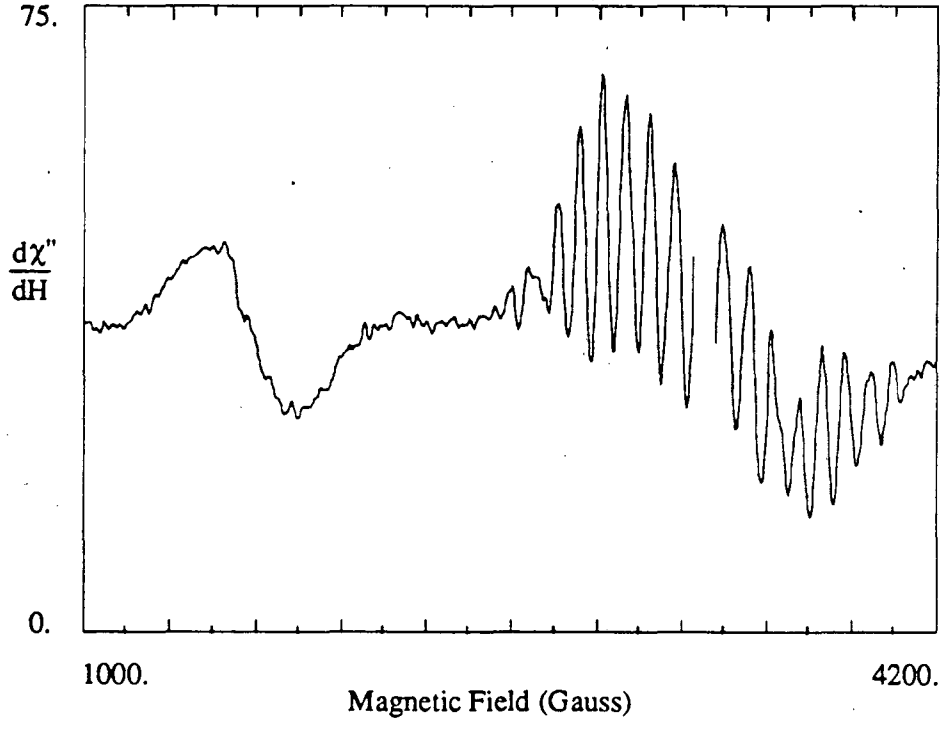
75.
dχ"/dH
0.
1000.
4200.
Magnetic Field (Gauss)

operated at its stable base temperature of 4.2 K. When the spectrometer is operated at very high gain, a monotonic increase in the baseline with increasing field strength may be observed. This corresponds to an increase in reflected microwave power resulting from strain induced in the cavity from interaction of the field modulation coils with the applied magnetic field. To compensate for this effect, linear baselines were subtracted from the signals.

The spin relaxation properties of the S_1 state parallel polarization signal were found to be dependent on the cryoprotectant used in the samples. Similar effects have been observed for the multiline and g = 4.1 conventional EPR signals (Zimmermann and Rutherford, 1986). In the case of the S_1 state signal, the signal saturated more readily in the presence of glycerol than in the presence of sucrose: in sucrose-containing samples, the signal could be detected at a microwave power of 20 mW, whereas the signal was not observable at this power level in glycerol-containing samples. The signal could be detected with either cryoprotectant at a microwave power level of 3 mW.

No parallel polarization EPR response associated with the S_2 state was detected. This result is consistent with the proposed spin state and symmetry assignments for the multiline and g = 4.1 signals, since no parallel polarization transitions are expected for $S = 1/2$ spin states or for axial $S = 3/2$ states when the axial zero-field parameter D is sufficiently large to result in a resonance in the g = 4 region.

5.3 Assignment of the signal to manganese in the oxygen-evolving complex

Illumination at 200 K, the condition that induced the disappearance of the parallel polarization signal, is known to result in both the oxidation of the oxygen-evolving complex, as evidenced by the appearance of the multiline and g = 4.1 conventional

EPR signals, and the reduction of the iron-quinone acceptor complex, as evidenced by the appearance of its conventional EPR signal at g = 1.9 (Rutherford and Zimmermann, 1984). Two independent control experiments were performed to address the origin of the parallel polarization EPR signal in the S_1 state. As one control, part of the preparation was depleted of the manganese ions associated with the oxygen-evolving complex. This was accomplished using a hydroxylamine treatment similar to that used by Tamura and Chenaie (1985): PS II membranes at a chlorophyll concentration of 1 mg/ml were incubated in the dark for 30 min in sucrose buffer containing 2.5 mM hydroxylamine and 5 mM EDTA, and then washed in an EDTA-containing sucrose buffer. This treatment resulted in the loss of the parallel polarization signal in the S_1 state, in addition to the expected loss of the ability to generate the multiline and g = 4.1 signals by illumination at 200 K, consistent with manganese as the origin of the signals. Results of a second control experiment directly rule out the iron-quinone acceptor complex as the origin of the parallel polarization signal. Illumination of intact preparations at 77 K instead of 200 K was used to induce electron donation to the iron-quinone acceptor complex by the alternate donor cyt b_{559}, rather than by the oxygen-evolving complex. This produced signals due to oxidized cyt b_{559} and the reduced iron-quinone acceptor complex in the conventional perpendicular polarization. No change was induced in the parallel polarization S_1 state signal following illumination at 77 K. The results of these control experiments imply that the oxidation of manganese, rather than the reduction of the iron-quinone acceptor complex, is responsible for the disappearance of the parallel polarization signal following advancement to the S_2 state by illumination at 200 K. The properties of the parallel polarization signal that are presented below indicate that the signal corresponds to the one-electron reduced form

of the exchange-coupled manganese species that gives rise to the multiline signal in the S_2 state.

5.4 The relation of the S_1 state signal to the multiline and g = 4.1 signals

5.4.A Models for the structure of the oxygen-evolving complex

The observation of not one, but two, light-induced EPR signals associated with the oxygen-evolving complex upon advancement to the S_2 state raises a difficult issue in the understanding of the structure and mechanism of the oxygen-evolving complex. Studies of the behavior of the two S_2 state EPR signals (Zimmermann and Rutherford, 1986; Hansson et al., 1987) indicate that upon advancement to the S_2 state, a given PS II unit will contribute either to the multiline signal or to the g = 4.1 signal, but the nature of this heterogeneity has not previously been clear. As discussed in Section 1.3, a variety of models have been proposed for the structural arrangement of the manganese ions in the oxygen-evolving complex. Two of these models specifically address the origin of both of the S_2 state EPR signals. de Paula, Beck, and Brudvig (1986) have suggested that all of the manganese ions are arranged in a single tetranuclear cluster and that the multiline and g = 4.1 signals arise, respectively, from $S = 1/2$ and $S = 3/2$ spin states corresponding to different conformations of this cluster. Alternatively, Hansson, Aasa and Vänngard (1987) have proposed that the multiline and g = 4.1 signals arise from separate sites. Each oxygen-evolving complex would contain both of these structural units, but in any given PS II unit, only one of the two centers would be oxidized following advancement to the S_2 state.

A key to distinguishing between these models lies in using the observation that the relative yield of the multiline and g = 4.1 signals depends on the experimental conditions (Zimmermann and Rutherford, 1986). As discussed above, the S_1 state signal

diminishes upon advancement to the S_2 state by illumination at 200 K, a condition that results in the generation of both the multiline and g = 4.1 signals. By comparing the change in the S_1 state signal amplitude to the amplitudes of the multiline and g = 4.1 signals generated under different conditions, we may determine the relation of the parallel polarization signal in the S_1 state to the multiline and g = 4.1 signals in the S_2 state, and in particular, we may determine whether the two S_2 state EPR signals arise from different conformations of a single cluster or from separate centers present in the oxygen-evolving complex.

The relation of the S_1 state signal to the multiline and g = 4.1 signals was investigated by illumination at different temperatures. For PS II membranes suspended in buffer containing glycerol, the relative yield of the two S_2 state signals depends on the illumination temperature: illumination at 140 K produces mostly the g = 4.1 signal, while illumination at 200 K produces mostly the multiline signal. Moreover, if a sample that has been illuminated at 140 K is warmed to 200 K in the dark, most of the PS II units that had contributed to the g = 4.1 signal undergo a conversion to the form that produces the multiline signal. (de Paula et al. attribute this conversion to a thermally-induced conformational change within a single tetranuclear cluster, while Hansson et al. attribute the conversion to electron transfer between two distinct centers.) A second illumination of the same sample at 200 K results in a further increase in the multiline signal amplitude, as well as a small increase in the g = 4.1 signal amplitude.

The changes in the S_1 state signal relative to the changes in the multiline and g = 4.1 signals were monitored throughout the course of an experiment in which an initially dark-adapted sample was first illuminated at 140 K for 9 min, then warmed to

200 K in the dark for 90 s, and finally illuminated again at 200 K for 5 min. Parallel polarization EPR spectra were collected as described in Section 5.2. Single scans of the conventional perpendicular polarization EPR spectra were collected before and after each step under the same conditions, except: microwave frequency, 9.34 GHz; microwave power, 0.5 mW, time constant, 0.5 s. The changes in the signal amplitudes from their initial values in the dark-adapted state are shown in Table 5.1. The multiline signal amplitude was taken as the average of the peak-to-peak amplitudes of two low-field hyperfine components that do not overlap cyt b_{559} features. These components were chosen because competitive donation by cyt b_{559} during the 140 K illumination results in cyt b_{559} signal intensity that precludes accurate measurement of the amplitude of a number of the hyperfine components of the induced multiline signal. The S_1 and g = 4.1 signal values are peak-to-peak amplitudes, and all signal intensities are quoted in arbitrary units.

5.4.B Identification of the S_1 state signal as a precursor to the multiline signal

The first conclusion that may be drawn from the data in Table 5.1 is that the decrease in the S_1 state signal from its initial value in the dark-adapted state is always proportional to the amplitude of the multiline signal observed under each condition. In general, a decrease in the amplitude of an EPR signal may result either from a decrease in the population of the species that gives rise to the signal or from a change in spin relaxation rates. In this experiment, the decrease of the S_1 signal upon generation of the multiline signal would likely indicate either that the S_1 state signal corresponds to a reduced form of the species that gives rise to the multiline signal when oxidized, or that the generation of the $S = 1/2$ multiline signal substantially increases the spin relaxation rate of some other species giving rise to the S_1 state

	Δ (S_1 Signal)	multiline	g = 4.1
illuminate at 140 K	–0.4	3	23
warm in dark at 200 K	–2.0	12	5
illuminate at 200 K	–4.5	29	13

Table 5.1. Comparison of the change in the S_1 state signal amplitude from its initial value in the dark-adapted state to the amplitudes of the multiline and g = 4.1 signals observed following each of a series of conditions. Signal amplitudes are in arbitrary units. Estimated uncertainties in the signal amplitudes are ± 0.15 unit for the S_1 state signal, ± 1 unit for the multiline signal, and ± 1.5 units for the g = 4.1 signal.

signal. However, the relatively slow spin relaxation rates for the multiline signal, as evidenced by time-domain measurements of $T_1 \approx 1$ ms at 4.2 K (R. D. Britt and M. P. Klein, unpublished data) and the relative ease with which the multiline signal is saturated at low temperature in cw measurements (Zimmermann and Rutherford, 1986), would result in the multiline signal being a very poor relaxer for the S_1 state species, which is assigned to an $S = 1$ spin state by means of the computer simulation discussed in Section 5.5. In addition, this argument would necessitate hypothesizing the presence of an additional paramagnetic center in PS II, and no direct evidence for such a center exists. Since measurements of the change in the manganese X-ray K-edge absorption energy indicate a one-electron oxidation of manganese in the S_1 to S_2 transition, and since EXAFS measurements do not indicate a major structural change in this transition (Yachandra et al., 1987), the proportionality of the decrease in the S_1 state signal to the amplitude of the multiline signal generated under different conditions indicates that the S_1 state signal arises from the one-electron reduced form of the species that gives rise to the multiline signal. The $S = 1$ spin state assignment is consistent with a species which, upon the loss of one electron, would produce the $S = 1/2$ multiline signal in the S_2 state.

5.4.C The multiline and g = 4.1 signals originate from separate paramagnetic species

The second conclusion that may be drawn from the data in Table 5.1 is that the g = 4.1 signal may be generated independently of any change in the parallel polarization S_1 state signal. Further interpretation of the data indicates that the multiline and g = 4.1 signals arise, respectively, from the oxidation of one or the other of two separate redox-active centers present in the oxygen-evolving complex. To make the arguments

leading to these conclusions more concrete, the signal amplitudes in Table 1 were used to estimate the percentage of oxygen-evolving complexes contributing to the g = 4.1 and multiline signals at each step of the experiment. The total number of PS II units that are oxidized from S_1 to S_2 by the illumination protocols is proportional to the weighted sum of the amplitudes of the multiline and g = 4.1 signals following the final illumination at 200 K. Defining this quantity as corresponding to 100 % of the oxygen-evolving complexes that are oxidized during the course of the experiment, we can work backwards and ascertain the fraction of these centers that are oxidized at each step in the procedure. The appropriate scaling factor for weighting the g = 4.1 signal relative to the multiline signal can be determined by comparing the decrease in the g = 4.1 signal to the increase in the multiline signal generated upon warming the sample in the dark at 200 K following illumination at 140 K. The changes in these signals induced upon warming in the dark result from the conversion of oxygen-evolving complexes from the form that gives rise to the g = 4.1 signal to the form that gives rise to the multiline signal, rather than from the generation of any new oxidizing equivalents. As a result, the decrease in the g = 4.1 signal (18 arbitrary units of g = 4.1 signal intensity) corresponds to the same number of oxidized oxygen-evolving complexes as the increase in the multiline signal (9 arbitrary units of multiline signal intensity). The resulting scaling factor may then be used to express each value for the multiline and g = 4.1 signal amplitude as a percentage of the total number of oxygen-evolving complexes oxidized during the course of the experiment. This estimation neglects any donor-acceptor charge recombination that might occur during the short 200 K warming step. Since the g = 4.1 signal recombines more readily than the multiline signal (Zimmermann and Rutherford, 1986), this would lead to an

underestimation of the fraction of centers contributing to the g = 4.1 signal in the first step of the experiment. However, since the conversion of the g = 4.1 signal to the multiline signal occurs much more rapidly than does recombination (Casey and Sauer, 1984), this error is expected to be small.

The results are displayed in Figure 5.2, where the data are interpreted in terms of a model in which the multiline and g = 4.1 signals originate from separate species. In the first step of the experiment, illumination at 140 K generates a g = 4.1 signal intensity corresponding to at least 32 % of the total number of PS II units in which the oxygen-evolving complex is oxidized during the course of the experiment, while the multiline signal amplitude corresponds to only 8 % of these units. Upon warming in the dark at 200 K, approximately two-thirds of those complexes initially giving rise to the g = 4.1 signal convert to produce additional multiline signal intensity. Following the final illumination at 200 K, 82 % of the oxidized oxygen-evolving complexes give rise to the multiline signal and 18 % to the g = 4.1 signal.

Comparison of the change in the S_1 state signal amplitude to the amounts of the g = 4.1 and multiline signals induced under the different conditions reveals that, while the decrease in the S_1 state signal is proportional to the amount of the multiline signal generated under each condition, the amount of the g = 4.1 signal is unrelated to the change in the S_1 state signal. The latter result is demonstrated most dramatically in the 140 K illumination step, in which a g = 4.1 signal amplitude corresponding to 32 % of the PS II units is observed, while only a small decrease, proportional to the small multiline signal corresponding to 8 % of the units, is seen in the S_1 state signal. A substantial decrease in the S_1 state signal is not observed until much of the g = 4.1 signal is converted to the multiline signal by warming in the dark at 200 K, and

Figure 5.2. Interpretation of the data in Table 5.1 in terms of a model in which two separate redox-active centers are present in the oxygen-evolving complex. The multiline species gives rise to the multiline EPR signal in its oxidized form and gives rise to the S_1 state parallel polarization EPR signal in its reduced form. The g = 4.1 species gives rise to the g = 4.1 EPR signal in its oxidized form and is not observed in its reduced form.

1. Dark

Both species present in the oxygen-evolving complex are in the reduced form in all PS II units.

The parallel polarization signal is present at is maximum amplitude.

2. Illuminate at 140 K

Forty percent of the PS II units advance to the S2 state. In 8 % of the units, the species that gives rise to the multiline signal is oxidized, and in 32 % of the units, the species that gives rise to the g = 4.1 signal is oxidized.

A small decrease, proportional to the amplitude of the multiline signal, is observed in the parallel polarization signal.

3. Warm in dark at 200 K

In approximately two-thirds of the units in which the g = 4.1 signal was induced during illumination at 140 K, the g = 4.1 signal is converted to the multiline signal, presumably by electron transfer between the two species. In the balance of the PS II units, the oxidation states of the two species remain unchanged.

The parallel polarization signal decreases by an amount proportional to the increase in the multiline signal amplitude.

4. Illuminate at 200 K

Additional PS II units are advanced to the S2 state. 82 % of the units oxidized during the entire course of the experiments are left with the multiline species oxidized, and 18 % are left with the g = 4.2 species oxidized.

The decrease in the parallel polarization signal from its initial value in the dark-adapted state is again proportional to the observed amplitude of the multiline signal.

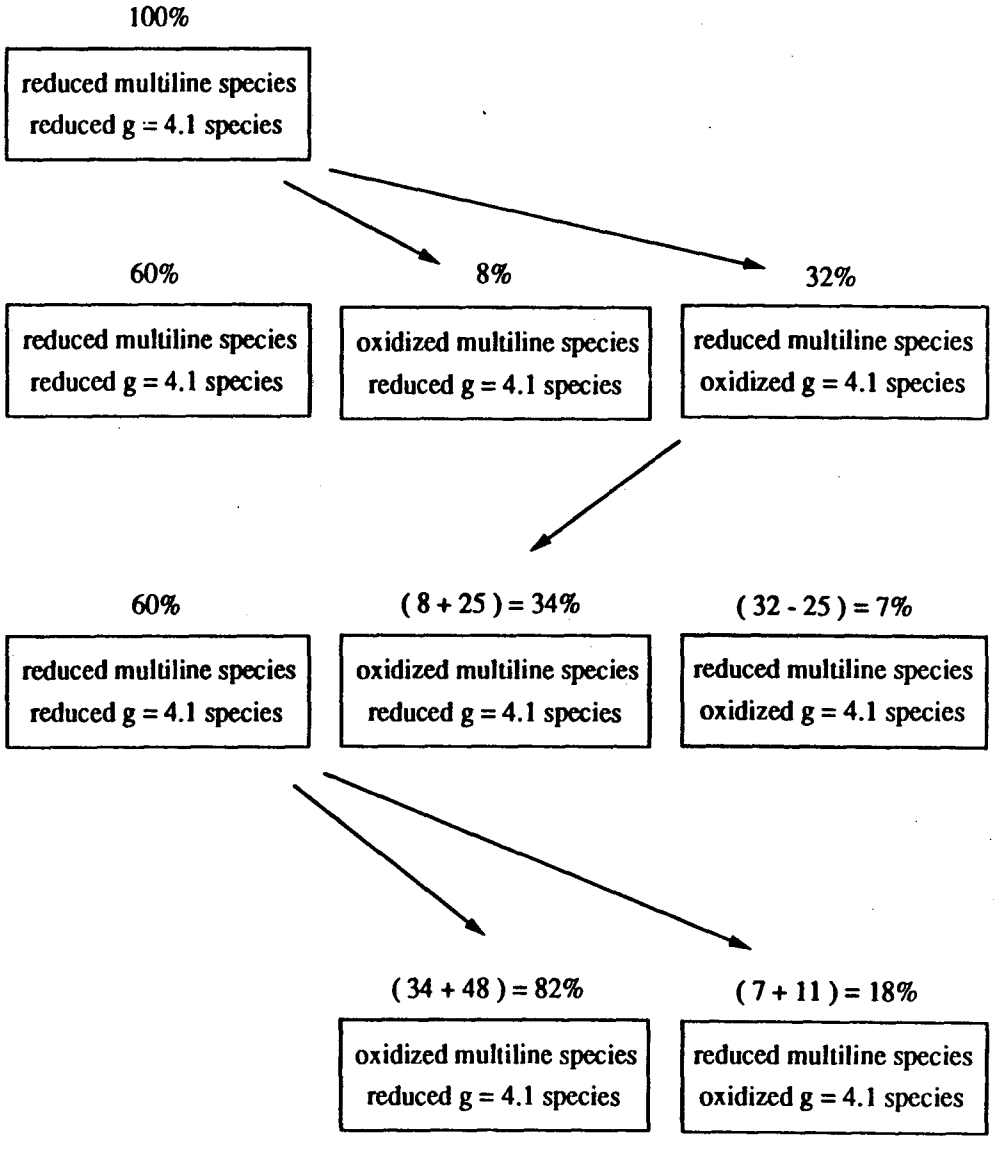

the resulting change in the S_1 state signal is found to be proportional to the multiline signal amplitude. In the second illumination, at 200 K, more centers are oxidized to generate additional multiline and g = 4.1 signal intensity, but the change in the S_1 state signal is again proportional only to the multiline signal amplitude.

Comparison of this data with the behavior expected for each of the two proposed models for the structure of the oxygen-evolving complex demonstrates that the g = 4.1 and multiline signals originate from two separate centers, rather than from different conformations of a single center. In the two-center model, we expect that generation of the g = 4.1 signal upon illumination at 140 K results from oxidation of one of the two types of centers in some fraction of the PS II units. The centers that give rise to the multiline signal when oxidized and the S_1 state parallel polarization signal when reduced would be expected to be relatively unaffected by illumination at 140 K, consistent with the observation of a small multiline signal and a proportionally small decrease in the S_1 state signal. The proposal that conversion of the g = 4.1 signal to the multiline signal upon warming in the dark at 200 K results from electron transfer between the two centers is also consistent with the data. Reduction of centers giving rise to the g = 4.1 signal would lead to a decrease in the amplitude of the g = 4.1 signal, and concomitant oxidation of the centers that give rise to the S_1 state signal would result in a decrease in the S_1 state signal proportional to the amount of induced multiline signal, as is observed. The second illumination, at 200 K, results in the oxidation of oxygen-evolving complexes that did not advance to the S_2 state in the first illumination. In a small fraction of these complexes, the g = 4.1 signal is induced, and in the remainder, the multiline signal is induced, leading again to a decrease in the S_1 state signal proportional to the induced multiline signal. The

species that gives rise to the parallel polarization signal would be expected to remain reduced in those oxygen-evolving complexes that contribute to the g = 4.1 signal, and the estimated amount of the parallel polarization signal amplitude remaining after the 200 K illumination is consistent with this expectation. Because of the presence of irregular background features, the parallel polarization S_1 state signal is most readily detected as a difference signal, and the absolute signal intensities in the dark and illuminated states are difficult to determine precisely. At best, it can be determined that at most 20 % of the original S_1 state signal intensity remains after a single 5 min illumination at 200 K of a previously dark-adapted sample containing either sucrose or glycerol. For the glycerol-containing samples that were carried through the three-step process of illumination at 140 K, warming in the dark at 200 K, and illumination at 200 K, 20 - 30 % of the original S_1 signal intensity observed in the dark-adapted state remained after the final 200 K illumination. A larger amount of residual signal might be expected under these conditions because of competitive electron donation by cyt b_{559} during the initial illumination at 140 K.

The data are not consistent with the proposal that the g = 4.1 and multiline signals arise from different conformations of a single tetranuclear cluster. The observations that a g = 4.1 signal amplitude corresponding to the oxidation of a substantial fraction of the centers can be generated with little change in the S_1 state signal and that the decrease in the S_1 state signal amplitude is always proportional to the amplitude of the multiline signal generated under different conditions rule out the possibility that the species responsible for the S_1 state signal could yield either the g = 4.1 or the multiline signal upon oxidation. Furthermore, even if the proposed tetranuclear cluster were to exist in two forms in the S_1 state, with the parallel polarization signal corresponding

only to the form of the cluster that would give rise to the multiline signal when oxidized, a thermally-induced conformational change from the form proposed to give rise to the g = 4.1 signal to the form proposed to give rise to the multiline signal would not be expected to lead to the observed decrease in the S_1 state signal upon warming a sample to 200 K in the dark following illumination at 140 K. In addition, cycling the temperature of a dark-adapted sample does not affect the amplitude of the observed parallel polarization signal, so no other thermally induced changes in the reduced centers are evident.

Even in the unlikely circumstance that the disappearance of the S_1 state signal upon generation of the multiline signal would correspond to enhanced spin relaxation of a separate S_1 signal species rather than simply to oxidation of a single center, as argued above, the experimental results still suggest that the g = 4.1 and multiline signals originate from separate centers within the oxygen-evolving complex. The data show that the S_1 state signal decreases only when the $S = 1/2$ multiline signal is generated and is unaffected by the generation of the $S = 3/2$ g = 4.1 signal. This observation is difficult to reconcile with a model in which the two S_2 state signals arise from different spin states corresponding to different conformations of a single cluster, since the $S = 3/2$ spin state that would correspond to the g = 4.1 signal would be expected to produce more efficient spin relaxation than the $S = 1/2$ state that would correspond to the multiline signal.

5.5 Computer simulation of the parallel polarization EPR spectrum

The field position and lineshape of the S_1 state signal suggest that it may correspond to a transition between the $|+\rangle$ and $|-\rangle$ levels of an $S = 1$ spin state. To test this proposal, and to determine the corresponding spin Hamiltonian parameters, computer

simulations were performed using the methods described in Section 2.5. The spin Hamiltonian for an $S = 1$ spin state includes the terms:

$$H_{Zeeman} = \beta \mathbf{H}_0 \cdot \mathbf{g} \cdot \mathbf{S}$$

$$H_{zero-field} = D[S_z^2 - \tfrac{1}{3}S(S+1)] + E(S_x^2 - S_y^2)$$

where D is the axial zero-field splitting parameter and E is the rhombic zero-field parameter. The origin of the spin Hamiltonian parameters are discussed in Section 2.3, and the energy levels and transitions for an $S = 1$ spin state are discussed in Section 2.4.A. Since the S_1 state signal most likely originates from an exchange-coupled center, the zero-field terms for its resultant spin will reflect the properties of the coupled ions as well as contributions from dipolar interactions.

The simulation is shown superimposed on the signal trace in Figure 5.3. Results of the simulation show that the parallel polarization signal in the S_1 state is consistent with a transition of Gaussian lineshape between the $|+\rangle$ and $|-\rangle$ levels of an $S = 1$ spin state with zero-field parameters D = -0.125 cm^{-1} and E = 0.025 cm^{-1}. Since the simulation is relatively insensitive to a small degree of g anisotropy, an isotropic g value of 2 was assumed. The simulation also predicts allowed transitions in the conventional perpendicular polarization. However, the anisotropy introduced by the zero-field Hamiltonian results in very broad and, therefore, unobservably weak transitions between $|-\rangle$ and $|O\rangle$ and between $|O\rangle$ and $|+\rangle$ spread over a broad range about g = 2. A weak perpendicular polarization transition is also predicted between the $|-\rangle$ and $|+\rangle$ levels for molecular orientations in which the applied field is away from the molecular principal axes. However, this transition would fall in the region of two considerably more intense signals, specifically the g = 4.3 rhombic iron feature and the light-induced g = 4.1 signal, precluding its observation either in the

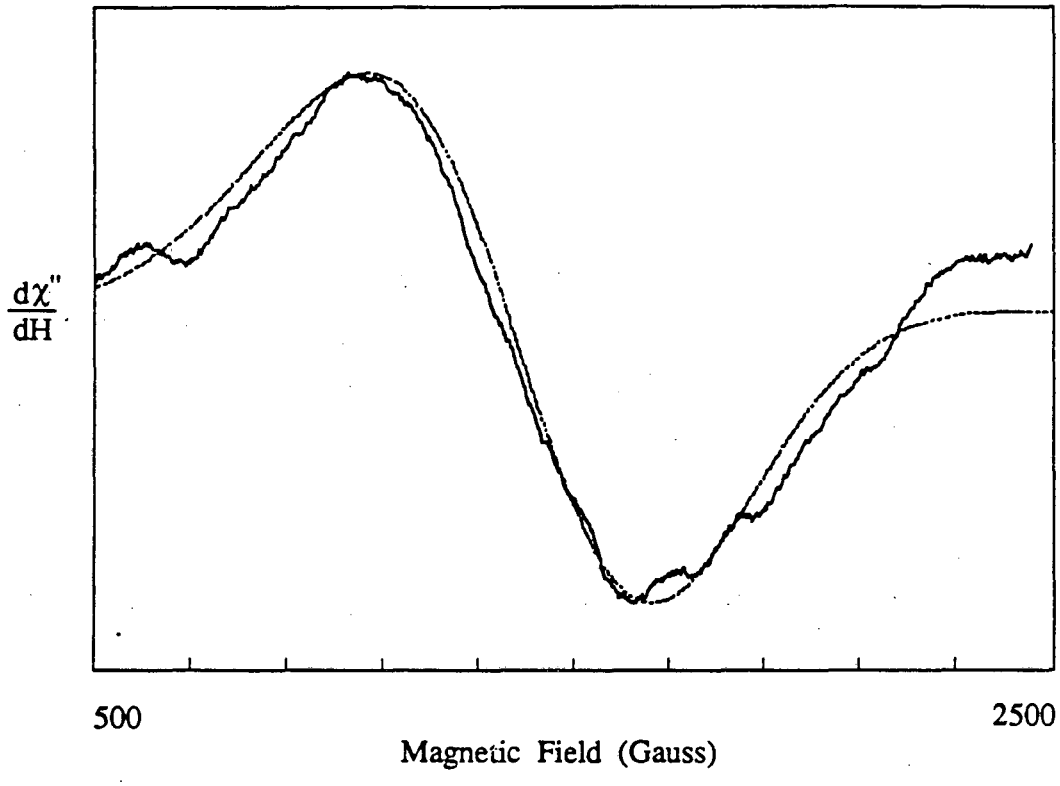

Figure 5.3. Solid line: S_1 state parallel polarization EPR signal. Dashed line: computer simulation using an $S = 1$ spin Hamiltonian with parameters g = 2, D = -0.125 cm^{-1}, and E = 0.025 cm^{-1}.

dark-adapted state or in a dark minus illuminated difference spectrum.

Simulations assuming an $S = 2$ spin state did not accurately reproduce the lineshape of the parallel polarization signal. The shape of the S_1 state parallel polarization signal is relatively symmetric, consistent with the weak orientation dependence of the splitting between the $S = 1 \mid - \rangle$ and $\mid + \rangle$ levels, as shown in Figure 2.4. In contrast, the intradoublet splittings of $S = 2$ states are quite anisotropic, as seen in Figure 2.6, leading to asymmetric lineshapes in powder spectra.

5.6 Discussion and Conclusions

The observation of the parallel polarization EPR signal provides direct evidence for the presence of a paramagnetic intermediate in the S_1 state. The behavior of the signal indicates that it corresponds to the one-electron reduced form of the exchange-coupled manganese complex that gives rise to the multiline signal in the S_2 state. X-ray absorption edge studies suggest that the S_1 state includes manganese ions in the Mn(III) oxidation state and that the S_1 to S_2 transition involves a change in the oxidation state of one of the ions from Mn(III) to Mn(IV) (Yachandra et al., 1987; Guiles, 1988; Sauer et al., 1988). The smallest structure that could give rise to an $S = 1$ signal in the S_1 state and the $S = 1/2$ multiline signal upon advancement to the S_2 state is a weakly antiferromagnetically coupled binuclear Mn_2(III,III) complex with a thermally populated first excited state. Weak antiferromagnetic exchange interactions have been observed in synthetic binuclear Mn_2(III,III) complexes (Sheats et al., 1987; Menage et al., 1988). Alternatively, the S_1 state signal could arise from a low-lying $S = 1$ state of an exchange-coupled complex of higher nuclearity.

Comparison of the change in the S_1 state signal to the amplitudes of the multiline and g = 4.1 signals generated upon advancement to the S_2 state under different experi-

mental conditions provides clear evidence for the presence of two separate redox-active centers within the oxygen-evolving complex. This result is suggestive of a mechanism in which one of the centers acts as a binding site for water, while the second center may participate in the associated electron transfer processes. The results of a number of experiments suggest that the center that gives rise to the multiline signal, and by implication, the S_1 state signal, acts as the binding site for water. EPR measurements have demonstrated that ammonia, which is thought to be a substrate analog for water, binds to the manganese cluster responsible for the multiline signal, and that this binding appears to take place in the S_1 state (Beck et al., 1986; Britt et al., 1989), and other EPR experiments involving D_2O or $H_2^{17}O$ treated PS II membranes have suggested possible binding of water to this species (Hansson et al., 1986; Nugent, 1987; Britt, 1988).

The structures of the two metal centers giving rise to the multiline and g = 4.1 signals are not yet entirely clear. The presence of a bridged structure with a Mn-Mn distance of 2.7 Å was established by early EXAFS experiments (Kirby et al., 1981; Yachandra et al., 1986). Hansson et al. (1987) proposed that the multiline signal arises from a binuclear Mn(III,IV) species and the g = 4.1 signal arises from a mononuclear Mn(IV) species of nearly axial symmetry; however, these particular assignments may not be fully consistent with the observed EXAFS scattering amplitudes when a stoichiometry of four mangnese ions per PS II unit is assumed. In addition, recent EXAFS results indicate the presence of additional manganese and/or calcium ions at distances greater than 3 Å (George et al., 1989; Penner-Hahn et al., 1990a,b). The suggestion that the g = 4.1 signal arises from a mononuclear Mn(IV) site implies that this species is present in the Mn(III) form in the S_1 state. Although the results presented in Chapter

4 demonstrate the possibility of detecting parallel polarization EPR signals from $S = 2$ states of mononuclear Mn(III) species, no such signals were detected in the S_1 state of the oxygen-evolving complex. However, this result does not conclusively rule out the proposal that the g = 4.1 signal originates from a mononuclear manganese species, as the inability to detect an $S = 2$ Mn(III) signal could be the result of fast spin relaxation or large splittings between the zero-field states, or also of a sufficiently large, positive value of the axial zero-field parameter D, which would place the transition between two relatively unpopulated excited levels.

The uncertainty about the structure of the manganese sites in the oxygen-evolving complex is due in part to a lack of a complete understanding of the hyperfine structure of the multiline signal. Synthetic binuclear Mn_2(III,IV) complexes exhibit a characteristic 16-line hyperfine spectrum that contains fewer lines and covers a somewhat smaller field range than the multiline signal. The presence of additional lines in the multiline signal has been taken as evidence that it arises from a cluster of higher nuclearity (Dismukes et al., 1982). However, no synthetic manganese complexes of any nuclearity have been found to have EPR features that directly match those of the multiline signal, and no satisfactory computer simulations of all the features of the multiline signal have been presented. Recent studies of the multiline signal at S-band microwave frequencies (Haddy et al., 1989) have revealed the presence of over 50 hyperfine components. The additional lines may result from the presence of hyperfine anisotropy, which is expected to be better resolved at lower microwave frequencies. As seen in the spectra presented in Chapter 4, Mn(III) ions may exhibit significant hyperfine anisotropy, and this would contribute to the hyperfine structure of an exchange-coupled cluster. Recent progress in understanding the hyperfine struc-

ture of binuclear mixed-valence manganese complexes (Diril et al., 1989) may lead to improved simulations of the multiline signal.

A number of biochemical treatments of the oxygen-evolving complex have provided insight into its structure and mechanism (for example, Casey and Sauer, 1984; Guiles et al., 1990a,b; Boussac et al., 1989). A number of these treatments have been found to alter the conventional EPR properties of the oxygen-evolving complex, providing motivation for analogous parallel polarization EPR studies. Unfortunately, many of these treatments damage a small fraction of the sites, resulting in release of manganese in the form of Mn^{2+} ions. EPR signals from a small amount of Mn^{2+} are usually inconsequential in conventional EPR experiments, since the signals from intact PS II components are quite large in comparison; however, they may easily interfere with parallel polarization measurements. These $S = 5/2$ transitions are discussed in Section 2.4.C. $Mn^{2+}(H_2O)_6$ produces a feature at g = 4 in the parallel polarization that overlaps the S_1 state signal at g = 4.8. In addition, Mn^{2+} in a distorted geometry, as might be expected for ions non-specifically bound to membrane surfaces, produces features throughout the low field region. Although the methods described in Section 5.2 were successful in preventing interference from Mn^{2+} in the standard PS II preparations, many of the biochemically modified preparations are not sufficiently stable to withstand additional washes.

In conclusion, the detection of the parallel polarization EPR signal in the S_1 state of the oxygen-evolving complex provides an additional spectroscopic probe for understanding the structure and mechanism of this complex. The behavior of the signal in the S_1 to S_2 transition leads to the conclusion that two separate redox centers are active in the oxygen-evolving complex, and the spectroscopic properties of the S_1 state

intermediate provide additional insight into the electronic structure of the manganese ions.

6 References

Aasa, R. and Vänngard, T. (1975) *J. Magn. Reson. 19*, 308.

Abragam, A. and Bleaney, B. (1970) *Electron Paramagnetic Resonance of Transition Ions*, Clarendon Press, Oxford.

Abragam, A. and Pryce, M. H. L. (1951) *Proc. Roy. Soc. London A205*, 135.

Allen, J. P., Feher, G., Yeates, T. O., Rees, D. C., Deisenhofer, J., Michel, H., and Huber, R. (1986) *Proc. Natl. Acad. Sci. USA 83*, 8585.

Al'tshuler, S. A. and Kozyrev, B. M. (1974) *Electron Paramagnetic Resonance in Compounds of Transition Elements, 2nd revised edition*, John Wiley & Sons: New York.

Anderson, P. W. (1959) *Phys. Rev. 115*, 2.

Anderson, R. S., Bates, C. A., and Jaussaud, P. C. (1972) *J. Phys. C 5*, 3397.

Andréasson, L.-E. and Vänngard, T. (1988) *Ann. Rev. Plant Physiol. Plant Mol. Biol. 39*, 379.

Aurbach, R. L. and Richards, P. L. (1975) *Phys. Rev. B 12*, 2588.

Babcock, G. T., Blankenship, R. E., and Sauer, K. (1976) *FEBS Lett., 61*, 286.

Babcock, G. T. (1987) in *Photosynthesis*, J. Amesz, Ed., Elsevier, Amsterdam, 125.

Baker, J. M. (1971) *Rep. Prog. Phys. 34,* 109.

Baker, J. M. and Bleaney, B. (1958) *Proc. Roy. Soc. (London) A 245,* 156.

Baltscheffsky, M., Ed. (1990) *Current Research in Photosynthesis,* Kluwer Academic Publishers, Dordrecht.

Baranowski, J., Cukierda, T., Jezowsak-Trzebiatowska, B., and Kozlowshi, H. (1979) *J. Magn. Reson. 33,* 585.

Barry, B. A. and Babcock G. T. (1987) *Proc. Natl. Acad. Sci. USA 84,* 7099.

Beck, W. F., de Paula, J. C., and Brudvig, G. W. (1986) *J. Am. Chem. Soc. 108,* 4018.

Bersuker, I. B. (1975) *Coord. Chem. Rev. 14,* 357.

Berthold, D. A., Babcock, G. T., and Yocum, C. F. (1981) *FEBS Lett. 134,* 231.

Beyer, W. F. and Fridovich, I. (1985) *Biochemistry 24,* 6460.

Blankenship, R. E. and Prince, R. C. (1985) *Trends in Biochem. Sci. 10,* 382.

Bossek, U., Weyhermuller, T. Wieghardt, K, Bonvoisin, J., and Girerd, J. J. (1989) *J. Chem. Soc., Chem. Commun.,* 633.

Boussac, A., Zimmermann, J.-L., and Rutherford, A. W. (1989) *Biochemistry 28,* 8984.

Britt, R. D. (1988) *Ph.D. Thesis,* Univ. of Calif., Berkeley, CA, USA, Lawrence Berkeley Laboratory Report LBL-25042.

Britt, R. D., Zimmermann, J.-L., Sauer, K., and Klein, M. P. (1989) *J. Am. Chem. Soc. 111,* 3522.

Brudvig, G. W., Casey, J. L., and Sauer, K. (1983) *Biochem. Biophys. Acta 723,* 366.

Brudvig, G. W. and Crabtree, R. H. (1986) *Proc. Natl. Acad. Sci. USA 83,* 4586.

Butler, W. F., Johnston, D. C., Shore, H. B., Fredkin, D. R., Okamura, M. Y., and Feher, G. (1980) *Biophys. J. 32,* 967.

Butler, W. F., Calvo, R., Fredkin, D. R., Isaacson, R. A., Okamura, M. Y., and Feher, G. (1984) *Biophys. J. 45,* 947.

Cartier, C., Verdaguer, M., Menage, S., Girerd, J. J., Tuchagues, J. P., and Mabad, B. (1986) *J. Physique C8,* 623.

Casey, J. L. and Sauer, K. (1984) *Biochim. Biophys. Acta 767,* 21.

Chan, M. K. and Armstrong, W. H. (1988) *Inorg. Chem. 28,* 3777.

Cheniae, G. M. (1980) *Methods Enzymol. 69,* 349.

Clayton, R. K. (1980) *Photosynthesis: Physical Mechanisms and Chemical Patterns,* Cambridge University Press, Cambridge.

Cole, J. L. (1987) *Ph.D. Thesis,* Univ. of Calif., Berkeley, CA, USA, Lawrence

Berkeley Laboratory Report LBL-24123.

Cole, J., Yachandra, V. K., Guiles, R. D., McDermott, A. E., Britt, R. D., Dexheimer, S. L., Sauer, K., and Klein, M.P. (1987) *Biochim. Biophys. Acta 890,* 395.

Cooper, S. R., Dismukes, G. C., Klein, M. P., and Calvin, M. (1978) *J. Am. Chem. Soc. 100,* 7248.

Christou, G. and Vincent, J. B. (1987) *Biochim. Biophys. Acta 895,* 259.

Debus, R. J., Barry, B. A., Babcock, G. T., and McIntosh, L. (1988a) *Proc. Natl. Acad. Sci. USA 85,* 427.

Debus, R. J., Barry, B. A., Sithole, I., Babcock, G. T., and McIntosh, L. (1988b) *Biochemistry 27,* 9071.

de Groot, M. S. and van der Waals, J. H. (1960) *Mol. Phys. 3,* 191.

Deisenhofer, J., Epp, O., Miki, K., Huber, R., and Michel, H. (1984) *J. Mol. Biol. 180,* 385.

Deisenhofer, J., Epp, O., Miki, K., Huber, R., and Michel, H. (1985) *Nature 318,* 618.

de Paula, J. C., Beck, W. F., and Brudvig, G. W. (1986) *J. Am. Chem. Soc. 108,* 4002.

Dexheimer, S. L. and Klein, M. P. (1988) *Rev. Sci. Instr. 59,* 764.

Dexheimer, S. L., Gohdes, J. W., Chan, M. K., Hagen, K. S., Armstrong, W. H., and

Klein, M. P. (1989) *J. Am. Chem. Soc. 111,* 8923.

Diril, H., Chang, H.-R., Nilges, M. J., Zhang, X., Potenza, J. A., Schugar, H. J., Isied, S. S., and Hendrickson, D. N. (1989) *J. Am. Chem. Soc. 111,* 5102.

Dismukes, G. C. and Siderer, Y. (1980) *FEBS Letters, 121,* 73.

Dismukes, G. C. and Siderer, Y. (1981) *Proc. Natl. Acad. Sci. USA 78,* 274.

Dismukes, G. C., Ferris, K., and Watnick, P. (1982) *Photobiochem. Photobiophys. 3,* 243.

Dowsing, R. D. and Gibson, J. F. (1969) *J. Chem. Phys. 50,* 294.

Dowsing, R. D. (1970) *J. Magn. Reson. 2,* 332.

Fackler, J. P. and Avdeef, A. (1974) *Inorg. Chem. 13,* 1864.

Fee, J. A., Shapiro, E. R., Moss, T. H. (1976) *J. Biol. Chem. 251,* 6157.

Figgis, B. N., Raston, C. L., Sharma, R. P., and White, A. H. (1978) *Aust. J. Chem. 31,* 2545.

George, G. N., Prince, R. C., and Cramer, S. P. (1989) *Science 243,* 789.

Gerritsen, H. J. and Sabisky, E. S. (1963) *Phys. Rev. 132,* 1507.

Golding, R. M. and Tennant, W. C. (1974) *Mol. Phys. 28,* 167.

Gray, H. B. and Malmström, B. G. (1989) *Biochemistry 28,* 7499.

Gregson, A. K., Doddrell, D. M., and Healy, P. C. (1978) *Inorg. Chem. 17,* 1216.

Griffith, J. S. (1961) *The Theory of Transition Metal Ions,* Cambridge University Press, Cambridge.

Griffith, J. S. (1972) in *Structure and Bonding 10,* Springer-Verlag, New York, 87.

Guiles, R. D. (1988) *Ph.D. Thesis,* Univ. of Calif., Berkeley, CA, USA, Lawrence Berkeley Laboratory Report LBL-25186.

Guiles, R. D., Zimmermann, J.-L., McDermott, A. E., Yachandra, V. K., Cole, J. L., Dexheimer, S. L., Britt, R. D., Wieghardt, K., Bossek, U., Sauer, K., and Klein, M. P. (1990a) *Biochemistry 29,* 471.

Guiles, R. D., Yachandra, V. K., McDermott, A. E., Cole, J. L., Dexheimer, S. L., Britt, R. D., Sauer, K., and Klein, M. P. (1990b) *Biochemistry 29,* 486.

Haddy, A., Aasa, R., and Andreasson, L.-E. (1989) *Biochemistry 28,* 6954.

Hagen, K. S., Armstrong, W. H., and Hope, H. (1987) *Inorg. Chem. 27,* 967.

Hagen, W. R. (1982) *Biochem. Biophys. Acta 708,* 82.

Ham, F. S. (1972) in *Electron Paramagnetic Resonance,* S. Geschwind, Ed., Plenum Press, New York, 1.

Hansson, Ö., Andreasson, L.-E., and Vänngard, T. (1986) *FEBS Lett. 195,* 151.

Hansson, Ö., Aasa, R., and Vänngard, T. (1987) *Biophys. J. 51,* 825.

Hearst, J. E. (1986) in *Photosynthesis III,* Staehelin, L. A. and Arntzen, C. J., Eds., Springer-Verlag, Berlin, 382.

Hendrich, M. P. and Debrunner, P. G. (1988) *J. Magn. Reson. 78,* 133.

Hendrich, M. P. and Debrunner, P. G. (1989) *Biophys. J. 56,* 489.

Holtzapfel, W., Finkele, U., Kaiser, W., Oesterhelt, D., Scheer, H., Stilz, H. U. and Zinth, W. (1989) *Chem. Phys. Lett. 160,* 1.

Joliot, P., Barbieri, G., and Chabaud, R. (1969) *Photochem. Photobiol. 10,* 309.

Kennedy, B. J. and Murray, K. S. (1985) *Inorg. Chem. 24,* 1552.

Kirby, J. A., Goodin, D. B., Wydrzynski, T., Robertson, A. S., and Klein, M. P. (1981) *J. Am. Chem. Soc. 103,* 5537.

Kirmaier, C., Holten, D., Debus, R. J., Feher, G., and Okamura, M. Y. (1986) *Proc. Natl. Acad. Sci. USA 83,* 6407.

Kok, B., Forbush, B., and McGloin, M. P. (1970) *Photochem. Photobiol. 11,* 457.

Kono, Y. and Fridovich, I. (1983) *J. Biol. Chem. 258,* 6015.

Lawrence, G. D. and Sawyer, D. T. (1978) *Coord. Chem. Rev. 27,* 173.

Levin, P. D. and Brill, A. S. (1988) *J. Phys. Chem. 92,* 5103.

Li, X., Kessissoglou, D. P., Kirk, M. L., Bender, C. J., and Pecoraro, V. L. (1988) *Inorg. Chem. 27,* 1.

Ludwig, M. L., Pattridge, K. A., and Stallings, W. C. (1986) in *Manganese in Metabolism and Enzyme Function*, Schramm, V. L. and Wedler, F. C., Eds., Academic Press: New York, 405.

Martin, J.-L., Breton, J., Hoff, A. J., Migus, A., and Antonetti, A. (1986) *Proc. Natl. Acad. Sci. USA, 83,* 957.

McDermott, A. E., Yachandra, V. K., Guiles, R. D., Cole, J. L., Dexheimer, S. L., Britt, R. D., Sauer, K., and Klein, M. P. (1988) *Biochemistry 27,* 4021.

Meijer, G. C. M. (1975) *J. Appl. Sci. Eng. A 1,* 129.

Menage, S., Girerd, J.-J., and Gleizes, A. (1988) *J. Chem. Soc. Chem. Commun.,* 431.

Michel, H. and Deisenhofer, J. (1988) *Biochemistry 27,* 1.

Mueller, K. A. (1968) *Phys. Rev. 171,* 350.

Nishida, Y. (1988a) *Inorg. Chim. Acta 151,* 177.

Nishida, Y. (1988b) *J. Inorg. Biochem. 32,* 277.

Nugent, J. H. A. (1987) *Biochim. Biophys. Acta 893,* 184.

Owen, J. and Harris, E. A. (1972) in *Electron Paramagnetic Resonance,* S. Geschwind,

Ed., Plenum Press, New York, 427.

Pake, G. E. and Estle, T. L. (1973) *The Physical Principles of Electron Paramagnetic Resonance, 2nd ed.,* W. A. Benjamin, Inc., Reading, Massachusetts.

Pecoraro, V. L. (1988) *Photochem. Photobiol. 48,* 249.

Pecoraro, V. L., Kessissoglou, D., Li, X., Lah, M. S., Saadeh, S., Bender, C., Bonadies, J. A., and Larson, E. (1990) in *Current Research in Photosynthesis, Vol. 1,* M. Baltscheffsky, Ed., Kluwer Academic Publishers, Dordrecht, 709.

Penner-Hahn, J. E., Fronko, R. M., Waldo, G. S., Yocum, C. F., Bowlby, N. R., and Betts, S. D. (1990a) in *Current Research in Photosynthesis, Vol. 1,* M. Baltscheffsky, Ed., Kluwer Academic Publishers, Dordrecht, 797.

Penner-Hahn, J. E., Fronko, R. M., Pecoraro, V. L., Yocum, C. F., Betts, S. D., and Bowlby, N. R. (1990b) *J. Am. Chem. Soc. 112,* 2549.

Plaksin, P. M., Stoufer, R. C., Mathew, M., and Palenik, G. J. (1972) *J. Am. Chem. Soc. 94,* 2121.

Poole, C. P., Jr. (1983) *Electron Spin Resonance: A Comprehensive Treatise on Experimental Techniques, 2nd ed.,* Wiley, New York.

Radmer, R. and Chenaie, G. (1977) in *Primary Processes of Photosynthesis,* Barber, J., Ed., Elsevier, Amsterdam, 303.

Rutherford, A. W. and Zimmermann, J.-L. (1984) *Biochem. Biophys. Acta 767,* 168.

Rutherford, A. W. (1989) *Trends in Biochem. Sci. 14,* 227.

Sauer, K., Guiles, R. D., McDermott, A. E., Cole, J. L., Yachandra, V. K., Zimmermann, J.-L., Klein, M. P., Dexheimer, S. L., and Britt, R. D. (1988) *Chem. Scripta 28A,* 87.

Scaringe, R. P., Hodgson, D. J., and Hatfield, W. E. (1978) *Mol. Phys., 35* 701.

Schwoerer, M., Huber, R. A., and Hartl, W. (1981) *Chem. Phys. 55,* 97.

Sheats, J. E., Czernuszewicz, R. S., Dismukes, G. C., Rheingold, A. L., Petrouleas, V., Stubbe, J., Armstrong, W. H., Beer, R. H., and Lippard, S. J. (1987) *J. Am. Chem. Soc. 109,* 1435.

Shulman, R. G., Yafet, Y., Eisenberger, P., and Blumberg, W. E. (1976) *Proc. Natl. Acad. Sci. USA 73,* 1384.

Staehelin, L. A. and Arntzen, C. J., Eds. (1986) *Photosynthesis III,* Springer-Verlag, Berlin.

Tamura, N. and Cheniae, G. (1985) *Biochem. Biophys. Acta 809,* 245.

Tanabe, Y. and Sugano, S. (1954) *J. Phys. Soc. Japan 9,* 753, 766.

Theg, S. M. and Sayre, R. T. (1979) *Plant Sci. Lett. 16,* 321.

Tinkham, M. (1956) *Proc. Roy. Soc. A 219,* 535, 549.

Tycko, R. and Opella, S. J. (1987) *J. Chem. Phys. 86,* 1761.

van der Waals, J. H. and de Groot, M. S. (1959) *Mol. Phys. 2,* 333.

Wertz, J. E. and Bolton, J. R. (1972) *Electron Spin Resonance,* McGraw-Hill, New York.

Wieghardt, K., Bossek, U., Bonvoisin, J., Beauvillain, P., Girerd, J. J., Nuber, B., Weiss, J., and Heinze, J. (1986) *Angew. Chem. Int. Ed. Engl. 25,* 1030.

Willing, A., Follmann, H., and Auling, G. (1988) *Eur. J. Biochem. 170,* 603.

Yachandra, V. K., Guiles, R. D., McDermott, A., Britt, R. D., Dexheimer, S. L., Sauer, K., and Klein, M. P. (1986) *Biochem. Biophys. Acta 850,* 324.

Yachandra, V. K., Guiles, R. D., McDermott, A. E., Cole, J. L., Britt, R. D., Dexheimer, S. L., Sauer, K., and Klein, M. P. (1987) *Biochemistry 26,* 5974.

Yamaguchi, K. and Sawyer, D. T. (1985) *Inorg. Chem. 24,* 971.

Yocum, C. F., Yerkes, C. T., Blankenship, R. E., Sharp, R. R., and Babcock, G. T. (1981) *Proc. Natl. Acad. Sci USA 78,* 7507.

Zimmermann, J.-L. and Rutherford, A. W. (1984) *Biochem. Biophys. Acta 767,* 160.

Zimmermann, J.-L. and Rutherford, A. W. (1986) *Biochemistry 25,* 4609.

LAWRENCE BERKELEY LABORATORY
TECHNICAL INFORMATION DEPARTMENT
1 CYCLOTRON ROAD
BERKELEY, CALIFORNIA 94720